Vibro-Acoustic Simulation of Poroelastic Shell Structures

Zur Erlangung des akademischen Grades eines
Doktors der technischen Wissenschaften
ausgeführte Dissertation

eingereicht an der
Fakultät für Bauingenieurwissenachaften
der Technischen Universität Graz

von

Michael Helmut Gfrerer

Berichter: Univ.-Prof. Dr.-Ing. Martin Schanz
Univ.-Prof. Dr. rer. nat. Ernst Rank

Graz, 2.5.2017

Statutory Declaration

I declare that I have authored this thesis independently, that I have not used other than the declared sources/resources, and that I have explicitly marked all material which has been quoted either literally or by content from the used sources. The text document uploaded to TUGRAZonline is identical to the present doctoral thesis.

Graz, _____ _____

Date Signature

Eidesstattliche Erklärung

Ich erkläre an Eides statt, dass ich die vorliegende Arbeit selbstständig verfasst, andere als die angegebenen Quellen/Hilfsmittel nicht benutzt, und die den benutzten Quellen wörtlich und inhaltlich entnommenen Stellen als solche kenntlich gemacht habe.

Graz, am _____ _____

Datum Unterschrift

Abstract

The aim of the present thesis is to provide a numerical method for the vibro-acoustic simulation of poroelastic shells. The proposed method can be used to investigate arbitrary curved layered panels, as well as their interaction with the surrounding air.

One focus of the present work lies on the use of exact geometry representations. The geometry of the shell can be given either parametrically or implicitly. The parametric variant can be used for arbitrarily given parametrizations where the parameter domain consists of rectangles. This includes standard parametric modeling techniques, *e.g.* NURBS surfaces. In the case of the implicit variant, the reference surface of the shell is given by the zero level of a given level-set function. In this case the reference surface is approximated by a triangulation in a first step. In a second step this triangulation is lifted to the exact reference surface. Thus, an element-wise exact parametrization is obtained. For the evaluation of integrals over the shell volume, the derivatives of the parametrizations up to the second order are required. These derivatives are computed by automatic differentiation making use of a hyper-dual number concept.

Typically, an acoustic panel consists of a number of layers with different properties. In the present work, porous layers are modeled by the Biot theory, whereas stiff layers can be modeled by the theory of elasticity. Due to this heterogeneous material layup, the though-the-thickness variation of the shell displacement and the filling fluid pressure are described layer-wise. This semi-discretization reduces the problem to a two-dimensional problem on the reference surface, which is discretized by a high order Finite Element Method (FEM).

In order to take the surrounding air into account, a variational variant of the Method of Fundamental Solutions (MFS) is developed. Thus, the meshing of the acoustic fluid domain can be avoided. The discretization of the fluid pressure field is given by fundamental solutions with source points lying in the complement of the fluid domain. The unknown coefficients are determined by a variational formulation. In the case of unbounded domains the Sommerfeld radiation condition has to be considered. Due to the use of fundamental solutions, this condition is exactly fulfilled and thus poses no difficulty. In order to simulate coupled fluid-structure interaction problems, the FEM and the MFS are combined to a coupled method.

The implementation of the uncoupled FEM for the shell and the uncoupled MFS is verified against numerical examples based on the Method of Manufactured Solutions. For the verification of the coupled method an example with a known exact solution is considered. In order to show the potential of the method, further examples are simulated. First, the FEM is applied to the Scordelis-Lo roof problem and to a gyroid structure. Second, the interior acoustics of a complex cavity and the scattering at an assembly of spheres is investigated by the uncoupled MFS. In the last two examples sound transmission from a cavity to a half-space is simulated.

Zusammenfassung

Die vorliegende Arbeit beschäftigt sich mit der Entwicklung von neuen Simulationsmethoden im Bereich von vibro-akustischen Anwendungen. Die entwickelten Techniken können zur Berechnung von beliebig gekrümmter und geschichteten Schalen eingesetzt werden. Ebenso ist eine Berücksichtigung der Interaktion mit der umgebenden Luft möglich.

Ein wesentlicher Fokus der Arbeit liegt auf der Verwendung von exakten Geometriebeschreibungen. Es wird zwischen zwei Fällen unterschieden, wie die Schalenreferenzfläche definiert wird. Im ersten Fall ist diese durch eine gegebene Parametrisierung beschrieben. Hierbei ist aus Implementierungsgründen die einzige Einschränkung, dass das Parametergebiet rechteckig sein muss. Es können jedoch beliebige Funktionen in der Parametrisierung verwendet werden. Dies beinhaltet standardisierte parametrische Modellierungskonzepte, wie zum Beispiel NURBS-Flächen, als Spezialfall. Im zweiten Fall ist die Schalenreferenzfläche implizit als Nullisofläche einer gegeben Funktion definiert. In einem ersten Schritt wird diese Fläche durch eine Triangulierung approximiert. Diese Vernetzung wird in einem zweiten Schritt auf die exakte Fläche gehoben. Somit wird eine elementweise exakte Parametrisierung erstellt. Für die Integration über das Schalen Volumen werden die Ableitungen bis zur zweiten Ordnung der Parametrisierungen benötigt. Diese Ableitungen werden durch ein automatisches Differentiationsschema, welches auf hyper-dualen Zahlen aufbaut, gewonnen.

Mit dem Ziel eines optimierten Bauteilverhaltens werden häufig Bauteile bestehend aus mehren Schichten eingesetzt. Dabei werden auch gezielt poröse Materialien verwendet. In der vorlegenden Arbeit werden diese Schichten mit der Theorie von Biot beschrieben. Nicht poröse Schichten werden durch die klassische linearisierten Elastizitätstheorie modelliert. Da das Materialverhalten der eingesetzten Materialien sehr unterschiedlich sein kann, wird eine schichtweise Beschreibung des Schalenaufbaus vorgenommen. Diese teilweise Diskretisierung reduziert das Schalenproblem auf ein zweidimensional Problem auf der Referenzfläche. Zur Lösung dessen wird eine FEM verwendet, welche auf Ansatzfunktionen beliebig wählbarer Ordnung aufbaut.

Für die Diskretisierung von Luftvolumina wird eine auf einem Variationsprinzip beruhende MFS entwickelt. Dies hat den Vorteil, dass keine aufwendige Vernetzung von Volumina erforderlich ist. Darüber hinaus wird durch die Approximation mithilfe von Fundamentallösungen die Abstrahlbedingung, welche im Fall von unbeschränkten Gebieten relevant ist, exakt erfüllt. Um die Interaktion der Schalenstruktur mit der umgebenden Luft zu simulieren, wird ein neues Kopplungsschema der FEM und der MFS vorgeschlagen.

Die implementierten Methoden werden mit numerischen Beispielen verifiziert. Die korrekte Implementierung der ungekoppelten Methoden wird anhand von konstruierten Beispielen mit exakten Lösungen gezeigt. Die gekoppelte Methode wird mithilfe von radialsymmetrischen Lösungen verifiziert. In einer Reihe von weiteren Beispielen wird das Potential der entwickelten Methoden veranschaulicht.

Danksagung

Die vorliegende Arbeit enstand im Rahmen meiner Tätigkeit am Institut für Baumechanik an der technischen Universität Graz in der Zeit von 2014 bis 2017.

Meinem Doktorvater Herrn Professor Martin Schanz möchte ich an dieser Stelle, für die Möglichkeiten die er mir eröffnet hat, meinen Dank aussprechen.

Herzlich bedanke ich mich bei Herrn Professor Ernst Rank für die Durchsicht der Abeit sowie die Übernahme des Gutachtens. Sein Interesse an meiner Arbeit ist mir eine Ehre und hat mich sehr gefreut.

Meinen Kollegen danke ich für die gute Zusammenarbeit. Das freundschaftliche Arbeitsklima, die fachlichen Disskusionen und die größe Hilfsbereitschft haben mir sehr gut gefallen.

Herzlich Danken möchte ich auch meinen Eltern für ihr Vertrauen und ihre Unterstützung.

Nagyon köszönöm feleségem, Anna segítségét. Én mindig köszönök.

Graz, Juni 2017

Michael Gfrerer

Contents

NOTATION

The index notation is used throughout this thesis except for Chapter 2, where the direct notation predominates. Greek indices receive the values 1, 2, whereas Latin indices receive the values 1, 2, 3. The Einstein summation convention is applied. Thus, whenever an index occurs once as a superscript and once as a subscript we sum over this index. Commas $()_{,i}$ denote derivatives with respect to the respective coordinates.

As long as no other meaning is explicitly given to a certain symbol within the text, its meaning corresponds to the following notation list. Some symbols refer to more than one meaning. However, their meaning becomes clear in a given context.

General symbols

i	imaginary unit number
$\nabla \cdot (\cdot)$	divergence operator
$\nabla(\cdot)$	gradient operator
Δ	Laplace operator
$(\cdot)_{,i}$	derivative with respect to θ^i
$\langle \cdot \rangle$	determinant
$\mathrm{adj}(\cdot)$	adjugate matrix

Special symbols

Ω	domain
$\partial\Omega, \Gamma$	boundary of the domain
$\mathbf{x}$	Cartesian coordinate
t	time, shell thickness
$\mathbf{u}$	displacement vector
$\boldsymbol{\epsilon}$	linearized strain tensor
ρ	mass density, fluctuating mass density
v	velocity
$\mathbf{b}$	body-force density
$\boldsymbol{\sigma}$	stress tensor
$\mathbf{t}$	traction vector

$\mathbf{n}$	normal vector
p	fluid pressure
K	bulk modulus
ω	angular frequency
f	frequency
k	wave number
Γ_{D}	boundary with prescribed Dirichlet data
Γ_{N}	boundary with prescribed Neumann data
g_D	prescribed Dirichlet data
g_N	prescribed Neumann data
$\mathbb{C}$	Elasticity tensor
λ	first Lamé parameter
μ	second Lamé parameter
$\bar{\mathbf{u}}$	vector-valued test function
$\bar{p}$	scalar-valued test function
$M_u,\ K_u$	bilinear forms, mass and stiffness matrix
$L,\ D$	bilinear forms, coupling matrices
H^1	space of functions with weak square integrable first order derivative
ϕ	Porosity of porous media, level-set function
$\mathbf{U}$	fluid displacement vector
$\boldsymbol{\epsilon}^s, \epsilon^f$	Strain tensor of the solid skeleton and the fluid
$\boldsymbol{\sigma}^s, \boldsymbol{\sigma}^f$	partial stress tensor of the solid skeleton and the fluid
b	viscose drag
ρ_s, ρ_f	mass density of the solid and the fluid
ρ_a	apparent mass density
α_∞	tortuosity
$\mathbf{q}$	relative mass flux
$\boldsymbol{\sigma}^{\text{tot}}$	total stress tensor
Γ^{ae}	interface between an acoustic fluid and an elastic body
Γ^{ap}	interface between an acoustic fluid and a poroelastic body
Γ^{ep}	interface between an elastic body and a poroelastic body
$\mathbf{e}_i, \mathbf{e}^i$	i-th standard base vector
$\mathfrak{g}, \bar{\mathfrak{g}}$	parametrization, surface parametrization
$U, \bar{U}$	parameter domain, parameter plane
$\bar{\Omega}$	surface in real space
θ^i	curvilinear coordinates
θ^3	thickness coordinate
$\mathbf{G}_i$	covariant base vector
$\mathbf{G}_i$	contravariant base vector
G_{ij}	covariant coefficient of the metric
G_{ij}	contravariant coefficient of the metric

δ_i^j	Kronecker delta
J	Jacobi matrix
$\Gamma_{ijl}, \Gamma_{ij}{}^{l}$	Christoffel symbols of first and second kind
$\overline{\mathbf{G}}_i$	covariant surface base vectors
$\overline{\mathbf{G}}^i$	contravariant surface base vectors
$h_{\alpha\beta}$	coefficient of the second fundamental form
H	mean curvature
K	Gaussian curvature
μ_β^α	components of the shifter
t	shell thickness
$\overset{(\cdot)}{\mathbf{u}}, \overset{(\cdot)}{p}$	parameter in shell model
L	number of layers
$\overset{(\cdot)}{V}$	thickness function
N_i	finite element basis function
Φ^e	mapping from reference element to the parameter or real space
ξ, η	coordinates in the reference element
ϕ_i	element shape function
p	finite element ansatz order
$\bar{\Omega}_h$	discrete surface
a	mapping from $\bar{\Omega}_h$ to $\bar{\Omega}$
s	search directions
Ω_+	upper half-space
Ω^{int}	interior fluid domain
Ω^{ext}	exterior fluid domain
$\mathcal{G}$	fundamental solution
$\mathcal{H}$	gradient of the fundamental solution

1 INTRODUCTION

The so far underestimated effects of the high noise level humans are exposed to has become an important focus in research. This can be seen on the web-page of the World Health Organization Europe: "Excessive noise seriously harms human health and interferes with people's daily activities at school, at work, at home and during leisure time. It can disturb sleep, cause cardiovascular and psychophysiological effects, reduce performance and provoke annoyance responses and changes in social behaviour.

Traffic noise alone is harmful to the health of almost every third person in the WHO European Region. One in five Europeans is regularly exposed to sound levels at night that could significantly damage health." [1]

This increased awareness of noise lead to higher requirements on the vibro-acoustic performance of products. In order to comply with the strict legal regulations, this has to be taken into account as early as in the design phase. Nevertheless, the trend to reduce material usage with the help of lightweight constructions complicates the goal to reach these vibro-acoustic requirements. Typically, lightweight poroelastic materials are used in the design to cope with this problem. In order to make the design process more efficient, it is of interest to replace expensive and time consuming experiments by adequate computer simulations. This thesis aims to enlarge the predictive capabilities of simulations for complex curved structures including poroelastic damping material.

1.1 State of the art

In this section, we introduce the main elements of our developments and provide a brief state of research on them. A more comprehensive review of the state of research is given in the respective sections.

Physical models in vibro-acoustic simulations. Due to the fact that in most applications only small vibration amplitudes occur, it is usual to use linear models in the field of vibro-acoustics. Therefore, air volumes are modeled with the acoustic fluid, whereas solid structures are modeled with the linearized theory of elasticity. Poroelastic materials are described with the dynamic Biot theory. This theory was published in [23] and has been adapted to acoustic applications. Present-day descriptions can be found in [5] and [60].

[1] http://www.euro.who.int/en/health-topics/environment-and-health/noise/noise, 18.2.2017

Shells. Many structural parts can be classified as of shell-type. Therefore, their thickness is very small when compared to the other dimensions. In such a situation, it is reasonable to describe the geometry by a curved two-dimensional surface in space. This includes plates as a special case, if the surface is flat. The analysis of thin structures is a long-standing research topic. The first accepted elastic plate theory was already published in 1850 by Kirchhoff [100]. However, he deduced his theory from *ad hoc* assumptions. The work of Kirchhoff was extended to shells by Love [113]. However, the most used thin shell model is attributed to Koiter [102, 103]. This model has been mathematically justified in [48]. The Koiter model uses only three displacement parameters and is therefore a shear-rigid model. The development of shear-flexible kinematics is attributed to Reissner [143, 144] and Mindlin [121]. The corresponding shell model with five parameters is named after Naghdi [123, 124]. The Koiter model as well as the Naghdi model require to use a reduce deformation energy in order to yield acceptable results. This means that the material law has to be modified. In order to avoid a modification of the material law, shell models based on seven-parameters seem to be appropriate, cf. [56]. However, if one fixed shell model is used the error introduced by the model is fixed. A series of hierarchical shell models addresses this issue [3, 16]. However, there proper construction is challenging in the case of laminated structures.

The latter are in turn important in many applications focusing on optimized material usage. A recent review of laminated plate and shell models is given in [36]. In principle, two types of theories can be distinguished. In the first type the number of parameters is independent of the number of layers. Such theories are termed equivalent single layer theory. The second type referred to as layer-wise theories, where the number of parameters depends on the number of layers. Such a theory is formed by packages of single-layer shell models coupled at the layer interfaces.

Most of the work in the field is devoted to elastic structures. Nevertheless, the present work deals with poroelastic shells. Following the ideas of Kirchhoff, thin poroelastic plate theories for the consolidation problem [165] and the dynamic problem [169] have been derived. In [160] the displacement kinematics are extended to allow shear deformations. Following the idea of a three-dimensional resolution, a series expansion in thickness direction by means of monomials has been utilized for single layer poroelastic plates in [126]. This approach has been extended to layered panels in [125], utilizing a layer-wise modelling. In this approach possible air layers can also be considered. A rigorous derivation of poroelastic plate and shell theories have been published only recently [117, 120].

Finite Element Method for shells with focus on exact geometry. The Finite Element Method (FEM) is the most popular numerical discretization method for the analysis of thin walled structures. Due to the shell-type geometry, various geometric locking phenomena can occur. To overcome this issue, a huge number of different techniques have been developed. In order to resolve the locking issues, many finite elements are based

on mixed variational formulations. Common techniques are Reduced Integration, Assumed Natural Strains, Enhanced Assumed Strains, and the Discrete Strain Gap method (cf. [40, 104, 184]). Another possibility is the use a high order ansatz functions to reduce the locking effects [64, 140].

Since the creation of the Isogeometric Analysis (IGA) framework [90], the use of exact geometry descriptions steaming from CAD systems within the analysis has become a focus in research. The basic idea of IGA is to extend the standard isoparametric concept to NURBS functions. Thus, the geometry is described parametrically. The parametrization is inherited from CAD. However, [11] deals with general parametrizations. To our best knowledge, this is the only publication which investigates shell problems by making use of the exact geometry in the case of general parametrizations.

Beside parametric surface descriptions implicit descriptions are also possible. To our best knowledge, there is no method dealing with shell problems which incorporates the exact geometry in the case of implicitly given geometry. [61] and [52] are the only two publications proposing an exact geometry treatment using surface finite elements solving the Laplace-Beltrami equation. This approach relies on the use of the signed distance function. Therefore, it is only exact for closed surfaces and for special cases of surfaces with boundary.

Boundary related methods. In the present work, we want to discretize not only a shell structure but also the surrounding fluid domain. We focus on the cases where these fluid domains are described only by their boundary. When only the boundary of a complex shaped domain is given, it can be a rather difficult task to generate a volume mesh. To tackle this problem, one possibility is to use embedded/fictitious domain methods. These methods are based on the idea of defining an auxiliary domain which can be meshed easily. As recent contributions in this field, we would like to mention the Finite Cell method [134, 156], the Cartesian grid method [118] and the CutFEM [35]. Recent developments in the context of Constructive Solid Geometry modeling can be found in [153] and [178]. An interesting application of this concept to shell analysis is given in [141]. Instead of embedding the problem domain in real space the parametric problem domain is embedded in an auxiliary parametric domain. However, in [141] no general mapping between parametric space and real space is deployed (cf. [99]).

Another possibility for the analysis of domains described by their boundary is to resort to boundary related methods, where no volume mesh is required. The most developed method of this type is the Boundary Element Method (BEM). In the direct BEM, the unknown boundary data are discretized, whereas in the indirect BEM, an auxiliary density function defined on the boundary is sought. This density function is used to describe the solution field. The indirect BEM can be seen as a Trefftz-type method. In such methods, the solution is approximated by a linear combination of basis functions, which fulfill the

underlying partial differential equation. Reviews on Trefftz-type methods along with their classification can be found in [101] and [85]. A Trefftz-type which was developed with the aim to solve vibro-acoustic problems is the Wave Based Method (WBM) developed in [62]. Since its first publication, this method has been constantly developed further [59]. Within the WBM, the solution is determined by means of a variational formulation. Another Trefftz-method is the Method of Fundamental Solutions (see *e.g.* [71]). This method uses fundamental solutions of the underlying partial differential equation for the solution approximation. Typically, the solution is determined by collocation at the boundary. Due to the use of fundamental solutions, the Sommerfeld radiation condition is fulfilled exactly. Thus, unbounded domains are easily treatable.

Coupled methods. It is common practice to consider vibro-acoustic systems as a number of interacting subsystems. As fluid domains and structural parts are of different nature, different discretization methods might be applied. Such methods have been reviewed in the previous two paragraphs. In order to simulate the full system considering all interactions, the different methods have to be coupled. The coupling of FEM-BEM is well known in literature. We mention [152] and [76] among others for the analysis in time domain. A FEM-BEM coupling schema for frequency domain sensitivity analysis was presented in [79]. A considerable amount of research work was devoted to the coupling of the WBM and the FEM for different situations as well. We mention the cases of structural (FEM) - acoustic fluid (WBM) coupling [171], acoustic fluid (WBM) - poroelastic domain (FEM) coupling [93] and the coupling of two different poroelastic domains [105]. Furthermore, a coupled FEM-MFS schema for two two-dimensional elastic domains was proposed in [81] and extended to a 2.5-dimensional model for the prediction of vibrations due to underground railway traffic in [9].

1.2 Parametric and implicit geometry description

One main aspect of this thesis is the use of exact geometry description. We aim to avoid the discretization of the geometry. In order to motivate the geometric settings treated in this thesis, the simple example of a circle is considered.

What is a circle?

It is the set of all points in a plane that are at a given distance from a given center. Mathematically speaking, in the Cartesian plane, a circle C with radius r and the center at the origin reads

$$C = \{(x,y) \in \mathbb{R}^2 \mid x^2 + y^2 - r^2 = 0\}. \tag{1.1}$$

x	y	weight
1	0	1
1	1	$\frac{\sqrt{2}}{2}$
0	1	1
-1	1	$\frac{\sqrt{2}}{2}$
-1	0	1
-1	-1	$\frac{\sqrt{2}}{2}$
0	-1	1
1	-1	$\frac{\sqrt{2}}{2}$
1	0	1

Table 1.1: Control points and weights for a NURBS curve of a circle

Another description of the same circle is given by

$$C = \{c(t) = (r\cos(t), r\sin(t)) \in \mathbb{R}^2 \mid 0 \leq t \leq 2\pi\}. \tag{1.2}$$

A third possibility is to utilize the concept of NURBS curves. To this end, we introduce the B-spline functions, which are given recursively by

$$N_{i,n} = f_{i,n}N_{i,n-1} + g_{i+1,n}N_{i+1,n-1}, \tag{1.3}$$

where

$$f_{i,n}(t) = \frac{t - k_i}{k_{i+n} - k_i} \tag{1.4}$$

and

$$g_{i,n}(t) = \frac{k_{i+n} - t}{k_{i+n} - k_i}. \tag{1.5}$$

Here, t is the parameter and k_i is the i^{th} knot. The lowest order basis functions $N_{i,0}$ are piece-wise constant functions. Then a NURBS curve is given by

$$c(t) = \sum_{i=1}^{l} \frac{N_{i,n}w_i}{\sum_{j=1}^{l} N_{j,n}w_j}\mathbf{P}_i \tag{1.6}$$

where l stands for the number of control points $\mathbf{P}_i$ and corresponding weights w_i. With these definitions, a third possibility to describe a circle is given by the list of control points and corresponding weights given in Table 1.1 and the knot vector $\{0,0,0,\pi/2, \pi/2,\pi,\pi,3\pi/2,3\pi/2,2\pi,2\pi,2\pi\}$.

All in all, there is an infinite number of possibilities to describe one and the same circle. We refer to the description (1.1) as an implicit representation. A point $\mathbf{p} \in C$ fulfills the equation $\phi(\mathbf{p}) = 0$, where $\phi(\mathbf{p}) = x^2 + y^2 - r^2$ in the case of the circle. The other two

descriptions above are referred to as of parametric type. A point $\mathbf{p} \in C$ is given by an equation depending on the single parameter t. Each of these three possibilities has its own advantage. In the case of the implicit curve, it is rather easy to determine if a point $\mathbf{p} \in \mathbb{R}^2$ lies on the circle, inside or outside of it. This can be easily judged by evaluating $\phi(\mathbf{p})$. In the case of a parametric representation, this question is much more difficult to answer. On the other hand, it is easy to place points on the parametric curve. In order to integrate on a curve, we need a parametrization. For example, to compute the length L of the circle, we have to solve the integral

$$L = \int_{t=0}^{2\pi} \left| \frac{\mathrm{d}c(t)}{\mathrm{d}t} \right| \mathrm{d}t. \tag{1.7}$$

In view of the integrand, the 'best' parametrization is the arc-length parametrization, where $\left| \frac{\mathrm{d}c(t)}{\mathrm{d}t} \right| = 1$. For the circle, this parametrization is stated in (1.2). The NURBS parametrization given above is not optimal regarding this aspect. However, it is not possible to obtain an arc-length parametrization of a circle by means of NURBS. Nevertheless, NURBS curves and surfaces constitute a standard technique in CAD, since they allow for an easy manipulation of the geometric object.

In this section, we considered parametric and implicit descriptions of a circle in the Cartesian plane. As this thesis deals with the analysis of shells, we will generalize these concepts in order to describe general surfaces in the three-dimensional Cartesian space. For the parametric description, we allow for general equations, which includes *e.g.* NURBS surfaces as special case.

1.3 Outline

In Chapter 2, the physical models studied in this thesis are introduced. These are the acoustic fluid modeling the air, the theory of elasticity modeling solids and the Biot theory of poroelasticity. We provide the governing equations, boundary conditions and coupling conditions for each model and for all possible coupling situations.

Chapter 3 is devoted to shell structures. First, the differential geometry of shells is presented. Second, the classical models for elastic shells are reviewed. Finally, we develop a model for laminated poroelastic shells.

In Chapter 4, the numerical methods to solve the arising boundary value problem are presented. We use the Finite Element Method to discretize the shell structure and the Method of Fundamental Solutions to discretize the air. A coupling of both methods is developed.

The verification of the implementation of the numerical methods developed in Chapter 4 is conducted in Chapter 5. We investigate the convergence behavior as the mesh is refined. For the shell FEM and the MFS exact solutions are used for the error evaluation. They are

constructed by means of the Method of Manufactured Solutions. The coupled method is verified against radial symmetric solutions.

Chapter 6 deals with further numerical results of the implemented methods. The presence of locking for low order FEMs is assessed. The influence of integration and the distance of the source points in the MFS is investigated. Furthermore, vibro-acoustic examples are presented in order to demonstrate the capabilities of the methods.

The thesis will be concluded with a summary in Chapter 7. A brief outlook on possible future work is provided.

2 PHYSICAL MODELS

In this chapter, the governing equations of the physical models are introduced, which will be solved numerically in Chapter 4. The treated models are the acoustic fluid, the elastic solid, and the poroelastic solid. All these models describe wave propagation phenomena and are thus time dependent. In this thesis we consider the case of harmonic time dependency only. In order to set up problems where are all three considered models are interacting at the same time, boundary and coupling conditions are presented.

All physical models presented here have common assumptions. First, the theory of continuum mechanics is adopted. It is assumed that matter completely fills the space it occupies. Therefore, the material is modeled as a continuous mass, rather than as discrete particles, ignoring the fact that matter is made of atoms. Consequently, only effects with length scales much greater than the atomic level are studied. The second common assumption is that only small changes in the state variables (*e.g.* pressure or displacements) are considered. Therefore, no distinction between the Euler description and the Lagrange description is necessary. Furthermore, this allows to neglect higher order terms in the governing equations and thus the obtained models are linear.

2.1 Material independent equations

In this section, the material independent concepts will be presented, which build the basis for all subsequent models. These are the kinematics of material bodies and the balance laws. In the following, we consider a material body $\Omega \subset \mathbb{R}^3$ with boundary Γ.

2.1.1 Kinematics

We describe the deformation of the material body by the deformation of the individual material points. Let $\mathbf{X}$ be the position vector of a material point at the time t_0. Due to movement and deformation, the material point will occupy $\mathbf{x}(t)$ at time t. In the following, the motion of the body is described by $\mathbf{x}(\mathbf{X},t)$. Assuming that the differential

$$\mathbf{F}(\mathbf{X},t) = \frac{\partial \mathbf{x}}{\partial \mathbf{X}} \tag{2.1}$$

exists and is non-singular, a bijective relation between $\mathbf{X}$ and $\mathbf{x}$ exists. Typically, $\mathbf{F}$ is called the deformation gradient. Since the deformation gradient $\mathbf{F}$ contains information about

local rigid body motions, it is not suitable as a strain measure. The polar decomposition of the deformation gradient can be expressed as

$$\mathbf{F} = \mathbf{R} \cdot \mathbf{U} = \mathbf{V} \cdot \mathbf{R}, \tag{2.2}$$

where $\mathbf{R}$ is a proper orthogonal tensor and $\mathbf{U}$ and $\mathbf{V}$ are symmetric positive definite tensors. An appropriate strain measure is given by the Green-Lagrange strain tensor

$$E = \frac{1}{2}\left(\mathbf{F}^\top \cdot \mathbf{F} - \mathbf{I}\right) = \frac{1}{2}\left(\mathbf{U}^\top \cdot \mathbf{U} - \mathbf{I}\right), \tag{2.3}$$

which is also called the change in metric tensor [46]. Introducing the displacement field $\mathbf{u} = \mathbf{x} - \mathbf{X}$, the Green-Lagrange strain tensor can be written as

$$E = \frac{1}{2}\left((\nabla \mathbf{u})^\top + \nabla \mathbf{u} + (\nabla \mathbf{u})^\top \cdot \nabla \mathbf{u}\right), \tag{2.4}$$

where $\nabla \mathbf{u}$ is the gradient of $\mathbf{u}$. Linearization of (2.4) with respect to $\mathbf{u}$ yields the linearized stain tensor

$$\boldsymbol{\epsilon} = \frac{1}{2}\left((\nabla \mathbf{u}) + (\nabla \mathbf{u})^\top\right). \tag{2.5}$$

2.1.2 Balance laws

Balance laws are material independent equations expressing the change of state of a continuum due to external influence. These equations are mostly formulated as integral equations. Assuming smoothness of the integrands, the equations can be localized. In the present thesis, we focus on mechanical fields. Extensions to other fields (thermal, electric,...) are not considered.

Balance of mass. In order to formulate the balance of mass, we define the mass M of a body Ω as

$$M = \int_\Omega \rho \, \mathrm{d}\mathbf{x}, \tag{2.6}$$

where ρ stands for the density. The balance of mass expresses how M changes with respect to time. We assume that no mass enters Ω through its boundaries and no internal production or loss of mass happens. Thus, the material time derivative of M equals zero, $\frac{\mathrm{d}M}{\mathrm{d}t} = 0$. Due to this special structure of no change, the balance of mass is called conservation of mass in this case. For further use, differentiation and integration are changed in order. This is accomplished in the Reynolds transport theorem

$$\frac{\mathrm{d}M}{\mathrm{d}t} = \int_{\Omega_t} \left(\frac{\partial \rho}{\partial t} + \nabla \cdot (\rho \, \mathbf{v})\right) \mathrm{d}\mathbf{x}, \tag{2.7}$$

where $\mathbf{v} = \frac{\partial \mathbf{x}}{\partial t}$ represents the velocity. $\nabla \cdot \mathbf{v}$ denotes the divergence of $\mathbf{v}$. Since the domain Ω is arbitrary, the localization theorem yields the local conservation of mass

$$\frac{\partial \rho}{\partial t} + \nabla \cdot (\rho\, \mathbf{v}) = 0. \tag{2.8}$$

For a smooth spatial field Φ holds [84]

$$\frac{\mathrm{d}}{\mathrm{d}t} \int_{\Omega} \Phi\, \rho \, \mathrm{d}\mathbf{x} = \int_{\Omega} \dot{\Phi}\, \rho \, \mathrm{d}\mathbf{x}, \tag{2.9}$$

if conservation of mass is assumed.

Balance of momentum. In order to state the momentum balance laws, we define the linear momentum of a body Ω as

$$\mathfrak{l} = \int_{\Omega} \mathbf{v}\, \rho \, \mathrm{d}\mathbf{x}, \tag{2.10}$$

and the angular momentum about the origin

$$\mathfrak{a} = \int_{\Omega} (\mathbf{x} \times \mathbf{v})\, \rho \, \mathrm{d}\mathbf{x}. \tag{2.11}$$

In view of (2.9), as a consequence of the conservation of mass, the relations

$$\begin{aligned} \frac{\mathrm{d}}{\mathrm{d}t}\mathfrak{l} &= \int_{\Omega} \frac{\mathrm{d}\mathbf{v}}{\mathrm{d}t}\, \rho \, \mathrm{d}\mathbf{x}, \\ \frac{\mathrm{d}}{\mathrm{d}t}\mathfrak{a} &= \int_{\Omega} \left(\mathbf{x} \times \frac{\mathrm{d}\mathbf{v}}{\mathrm{d}t} \right) \rho \, \mathrm{d}\mathbf{x} \end{aligned} \tag{2.12}$$

hold. The momentum balance laws are given by

$$\begin{aligned} \frac{\mathrm{d}}{\mathrm{d}t}\mathfrak{l} &= \int_{\Gamma} \mathbf{t} \, \mathrm{d}s_{\mathbf{x}} + \int_{\Omega_t} \mathbf{b} \, \mathrm{d}\mathbf{x}, \\ \frac{\mathrm{d}}{\mathrm{d}t}\mathfrak{a} &= \int_{\Gamma} \mathbf{x} \times \mathbf{t} \, \mathrm{d}s_{\mathbf{x}} + \int_{\Omega} \mathbf{x} \times \mathbf{b} \, \mathrm{d}\mathbf{x}, \end{aligned} \tag{2.13}$$

where $\mathbf{t}$ stands for the surface tractions and $\mathbf{b}$ is the body force density. A central result in continuum mechanics is given by Cauchy's Theorem [84]. It asserts that a necessary and sufficient condition that the momentum balance laws be satisfied is that there exist a tensor field $\boldsymbol{\sigma}$ (stress tensor) such that

(a) for each unit vector $\mathbf{n}$,

$$\mathbf{t}(\mathbf{n}) = \boldsymbol{\sigma} \cdot \mathbf{n},$$

(b) $\boldsymbol{\sigma}$ is symmetric,

(c) $\boldsymbol{\sigma}$ satisfies the equation of motion

$$\rho \left(\frac{\partial \mathbf{v}}{\partial t} + \mathbf{v} \cdot \nabla \mathbf{v} \right) = \nabla \cdot \boldsymbol{\sigma} + \mathbf{b}. \tag{2.14}$$

Up to this point, we have summarized the material independent equations that will be used in the rest of this thesis. In the following three sections, we will specialize these equations and introduce material dependent constitutive laws, in order to obtain the equations for an acoustic fluid, an elastic solid and a poroelastic solid.

2.2 Acoustic fluid

The acoustic fluid is a widely used model to describe the propagation of sound in fluids. The starting point for the derivation is the conservation of mass

$$\frac{\partial \rho}{\partial t} + \nabla \cdot (\rho \mathbf{v}) = 0, \tag{2.15}$$

and the equation of motion

$$\rho \left(\frac{\partial \mathbf{v}}{\partial t} + \mathbf{v} \cdot \nabla \mathbf{v} \right) = \nabla \cdot \boldsymbol{\sigma} + \mathbf{b}. \tag{2.16}$$

In the following, we will introduce several assumptions in order to derive the equations for an acoustic fluid [145]. At first, we assume that the fluid is inviscid and no shear stresses occur. Therefore, no energy is dissipated inside the fluid and the stress tensor can be written in terms of the pressure as $\boldsymbol{\sigma} = -p\,\mathbf{I}$. Next, we assume only small disturbances around a mean value. The physical quantities can be expressed as the sum of their time mean parts and fluctuating parts,

$$\begin{aligned} \rho &= \rho_0 + \tilde{\rho}, \\ \mathbf{v} &= \mathbf{v}_0 + \tilde{\mathbf{v}}, \\ p &= p_0 + \tilde{p}. \end{aligned} \tag{2.17}$$

Here, ρ_0, $\mathbf{v}_0$, p_0 represent the initial density, the mean flow velocity and the ambient pressure. Additionally, we assume that the fluid is homogeneous and isotropic. Thus, the time mean parts are constant with respect to space and time. The quantities $\tilde{\rho}$, $\tilde{\mathbf{v}}$, $\tilde{p}$ stand for the spacial and time variable density variation, velocity variation, and pressure variation, respectively. Furthermore, it is assumed that the fluid is initially at rest. Hence, the

mean flow velocity is zero, $\mathbf{v}_0 = \mathbf{0}$. Introducing all assumptions so far in (2.15) and (2.16) yields

$$\begin{aligned} \frac{\partial \tilde{\rho}}{\partial t} + \nabla\tilde{\rho}\cdot\tilde{\mathbf{v}} + (\rho_0+\tilde{\rho})\nabla\cdot\tilde{\mathbf{v}} = 0, \\ (\rho_0+\tilde{\rho})\left(\frac{\partial \tilde{\mathbf{v}}}{\partial t} + \tilde{\mathbf{v}}\cdot\nabla\tilde{\mathbf{v}}\right) + \nabla\tilde{p} = \mathbf{b}, \end{aligned} \tag{2.18}$$

where we used $\nabla\rho_0 = \mathbf{0}$ and $\nabla p_0 = \mathbf{0}$. Since acoustic disturbances have only a very small amplitude, we can neglect products of small parameters, which leads to

$$\begin{aligned} \frac{\partial \tilde{\rho}}{\partial t} + \rho_0\nabla\cdot\tilde{\mathbf{v}} = 0, \\ \rho_0\frac{\partial \tilde{\mathbf{v}}}{\partial t} + \nabla\tilde{p} = \mathbf{b}. \end{aligned} \tag{2.19}$$

In (2.19), two equations for three variables are given. In order to close the theory, an additional equation has to be provided. It is assumed that the fluid is an ideal gas, and the wave propagation happens adiabatic and reversible. Thus, the equation is

$$\tilde{\rho} = \frac{\rho_0}{\gamma\, p_0}\tilde{p}, \tag{2.20}$$

where $\gamma = \frac{c_p}{c_V}$ is the ratio of specific heat at constant pressure and specific heat at constant volume. For air, it has the value $\gamma = 1.4$. Introducing the bulk modulus $K^a = \gamma\, p_0$, the governing equations of an acoustic fluid in the time domain are

$$\begin{aligned} \frac{\partial p}{\partial t} + K^a\nabla\cdot\mathbf{v} = 0, \\ \rho_0\frac{\partial \mathbf{v}}{\partial t} + \nabla p = \mathbf{b}. \end{aligned} \tag{2.21}$$

In (2.21), we have dropped the tilde for the sake of a simpler notation. In the following, we will always refer to the fluctuating part, although not stated.

Frequency domain. In a next step, the corresponding frequency domain equations are developed. To this end, a harmonic time dependency is assumed. Therefore, a time dependent quantity can be written as the real part of a product of two functions, *i.e.*

$$\chi(x,t) = \Re[\bar{\chi}(x)\,\mathrm{e}^{\mathrm{i}\omega t}] \tag{2.22}$$

for a generic real valued field χ, whereas $\bar{\chi}$ is a complex valued field. Furthermore, i and ω stand for the imaginary unit and the angular respectively. The angular frequency is related to the ordinary frequency f by $\omega = 2\pi f$. Assuming a time dependency of type (2.22) for

all variables, the frequency domain equations are obtained. The balance of mass and the balance of momentum in the frequency domain are

$$\mathrm{i}\omega\bar{p} + K\,\nabla\cdot\bar{\mathbf{v}} = 0 \tag{2.23}$$

and

$$\mathrm{i}\omega\rho_0\bar{\mathbf{v}} + \nabla\bar{p} = \bar{\mathbf{f}}\,. \tag{2.24}$$

Thus, the particle velocity can be expressed in terms of the pressure gradient,

$$\bar{\mathbf{v}} = \frac{\bar{\mathbf{f}} - \nabla\bar{p}}{\mathrm{i}\omega\rho_0}\,. \tag{2.25}$$

Inserting (2.25) in (2.23) yields the Helmholtz equation

$$k^2 p + \Delta p = g, \tag{2.26}$$

where $g = \nabla\cdot\bar{\mathbf{f}}$, $k = \omega\sqrt{\frac{\rho_0}{K}}$ is the wave number and $\Delta = \nabla\cdot\nabla$ the Laplace operator. In (2.26) we have dropped the bar for the sake of simplicity.

Boundary value problem. Given the material parameter ρ, K and the domain Ω with boundary $\Gamma = \Gamma_D \cup \Gamma_N$, let g, g_D, g_N be given scalar functions. Find $p(x,\omega)$ such that

$$\begin{aligned} k^2 p + \Delta p &= g && \text{in } \Omega, \\ p(x,\omega) &= g_D(x,\omega) && \text{for } x \in \Gamma_D, \\ v_n(x,\omega) &= g_N(x,\omega) && \text{for } x \in \Gamma_N. \end{aligned} \tag{2.27}$$

On the Dirichlet boundary Γ_D, the pressure has the prescribed value g_D, whereas on the Neumann boundary Γ_N, the normal velocity $v_n = \mathbf{v}\cdot\mathbf{n}$ has the prescribed value g_N. In the case of an unbounded domain, the solution has to fulfill the Sommerfeld radiation condition

$$\lim_{|x|\to\infty} |x| \left(\frac{\partial}{\partial |x|} + \mathrm{i}k \right) p(x) = 0, \tag{2.28}$$

first considered in [161].

2.3 Elastic solid

In this section, we summarize the governing equations for wave propagation in elastic media. Among many others, we mention the books of Altenbach [6] and Holzapfel [86] for nice presentations of the nonlinear theory. An in-depth mathematical foundation of the theory of elasticity is given by Gurtin [84] and Marsden and Hughes [119], among others.

A book with special focus on differential geometry is given by Ciarlet [46]. Books with a focus on wave propagation in elastic solids are those by Achenbach [1], Eringen and Suhubi [70] and Graff [83], among many others.

In contrast to the acoustic fluid, where the variable in (2.26) is the pressure p, in case of an elastic solid, we choose the displacement field $\mathbf{u}$ as the primal variable. Assuming only small oscillations around a balanced initial state, the equation of motion (2.14) simplifies to

$$\rho_0 \frac{\partial^2 \mathbf{u}}{\partial t^2} = \nabla \cdot \boldsymbol{\sigma} + \mathbf{b}. \tag{2.29}$$

Here, $\mathbf{u}$ and $\boldsymbol{\sigma}$ refer to the oscilatory parts. Since only small oscillations are considered, it is quite feasible to linearize the material law at the initial state. Furthermore, we are assuming a homogeneous and isotropic material. Then the relation between stress tensor and strain tensor can be written as

$$\boldsymbol{\sigma} = \mathbb{C} : \boldsymbol{\epsilon} \tag{2.30}$$

with the isotropic elasticity tensor

$$\mathbb{C} = \lambda\, \mathbf{I} \otimes \mathbf{I} + 2\mu\, \mathsf{I} \tag{2.31}$$

where $\mathbf{I}$ is the second-rank identity tensor, and I is the symmetric part of the fourth-rank identity tensor. λ, μ and are the first and the second Lamé parameters. They can be expressed in terms of other important material parameters

$$\lambda = \frac{E\nu}{(1+\nu)(1-2\nu)}, \tag{2.32}$$

$$\mu = \frac{E}{2(1+\nu)}, \tag{2.33}$$

$$\lambda = K - \frac{2}{3}G, \tag{2.34}$$

$$\mu = G, \tag{2.35}$$

where E is the Young's modulus, ν is the Poisson's ratio, K is the bulk modulus, and G the shear modulus. Nevertheless, only two parameters can be given independently for an isotropic material.

Frequency domain. Assuming harmonic time dependency (2.22), the equation of motion gets

$$-\rho_0\, \omega^2 \mathbf{u} = \nabla \cdot \boldsymbol{\sigma} + \mathbf{b}. \tag{2.36}$$

In order to include dissipation in the elastic solid, we allow for complex valued material parameters. In the present thesis we assume that the material parameters are frequency independent. We remark that this is not consistent with any viscous dissipation model in

time domain. For a detailed discussion on viscoelasticity, we refer to [44] among others. Inserting (2.30) and (2.5) in (2.29) yield the elastodynamic wave equation in frequency domain

$$-\rho_0\,\omega^2\mathbf{u} = (\lambda+\mu)\nabla\cdot\nabla\mathbf{u} + \mu\Delta\mathbf{u} + \mathbf{b}. \tag{2.37}$$

Next, we state the strong form of the boundary value problem.

Boundary value problem. Given the material parameter ρ, λ, μ and the domain Ω with boundary $\Gamma = \Gamma_D^i \cup \Gamma_N^i$ for each $i = 1,2,3$. Let $\mathbf{b}$ be a given vector-valued function and u_i^D, t_i^N given scalar-valued functions. Find $\mathbf{u}(x,\omega)$ such that

$$\begin{aligned} -\rho\;\omega^2\mathbf{u} &= \nabla\cdot\boldsymbol{\sigma} + \mathbf{b} && \text{in } \Omega, \\ \boldsymbol{\sigma} &= \mathbb{C} : \boldsymbol{\epsilon} \\ \boldsymbol{\epsilon} &= \frac{1}{2}\left((\nabla\mathbf{u}) + (\nabla\mathbf{u})^\top\right) \\ u_i(x,\omega) &= u_i^D(x,\omega) && \text{for } x \in \Gamma_D^i, \\ t_i(x,\omega) &= t_i^N(x,\omega) && \text{for } x \in \Gamma_N^i. \end{aligned} \tag{2.38}$$

On the Dirichlet boundary Γ_D^i the displacement in direction i has the prescribed value u_i^D. On the Neumann boundary Γ_N^i the surface traction in direction i has the prescribed value t_i^N.

The Finite Element Method, which will be used to discretize the elastic solid domains is rather based on the weak form of the governing equations than on the strong form given above. In the following, the derivation of the weak form is given.

Weak form. We follow the presentation in [94]. The space of test functions is defined as $V_0 = \{\bar{\mathbf{u}} \in [H^1(\Omega)]^3 |\ \bar{u}_i = 0 \text{ on } \Gamma_D^i\}$. Multiplying (2.36) with a vector-valued test function $\bar{\mathbf{u}} \in V_0$ and integrating over the domain Ω we obtain

$$\int_\Omega \left(-\rho_0\,\omega^2\mathbf{u}\cdot\bar{\mathbf{u}} - (\nabla\cdot\boldsymbol{\sigma})\cdot\bar{\mathbf{u}}\right)\mathrm{d}\mathbf{x} = \int_\Omega \mathbf{b}\cdot\bar{\mathbf{u}}\,\mathrm{d}\mathbf{x}. \tag{2.39}$$

Integration by parts of the second term on the left yields

$$\int_\Omega \left(-\rho_0\,\omega^2\mathbf{u}\cdot\bar{\mathbf{u}} + \boldsymbol{\sigma} : \nabla\bar{\mathbf{u}}\right)\mathrm{d}\mathbf{x} = \int_\Omega \mathbf{b}\cdot\bar{\mathbf{u}}\,\mathrm{d}\mathbf{x} + \int_\Gamma \mathbf{t}\cdot\bar{\mathbf{u}}\mathrm{d}s_x. \tag{2.40}$$

Due to the symmetry of $\boldsymbol{\sigma}$,

$$\boldsymbol{\sigma} : \nabla\bar{\mathbf{u}} = \boldsymbol{\sigma} : \boldsymbol{\epsilon}(\bar{\mathbf{u}}) = (\mathbb{C} : \boldsymbol{\epsilon}(\mathbf{u})) : \boldsymbol{\epsilon}(\bar{\mathbf{u}}) \tag{2.41}$$

holds. In a next step, the boundary conditions are taken into account. We have $t_i = t_i^N$ on Γ_N^i and by construction of the test space $\bar{u}_i = 0$ on Γ_D^i. Considering this in the last integral we obtain

$$-\rho\ \omega^2 M_u(\mathbf{u},\bar{\mathbf{u}}) + K_u(\mathbf{u},\bar{\mathbf{u}}) = f_V(\bar{\mathbf{u}}) + f_N(\bar{\mathbf{u}}), \tag{2.42}$$

where

$$\begin{aligned} M_u(\mathbf{u},\bar{\mathbf{u}}) &= \int_\Omega \mathbf{u}\cdot\bar{\mathbf{u}}\ \mathrm{d}\mathbf{x}, \\ K_u((\mathbf{u},\bar{\mathbf{u}}) &= \int_\Omega (\mathbb{C} : \boldsymbol{\epsilon}(\mathbf{u})) : \boldsymbol{\epsilon}(\bar{\mathbf{u}})\ \mathrm{d}\mathbf{x}, \\ f_V(\bar{\mathbf{u}}) &= \int_\Omega \mathbf{b}\cdot\bar{\mathbf{u}}\ \mathrm{d}\mathbf{x}, \\ f_N(\bar{\mathbf{u}}) &= \int_{\Gamma_N^i} t_i^N\ \bar{u}_i\ \mathrm{d}s_x. \end{aligned} \tag{2.43}$$

Thus, the weak form of the problem reads: Find $\mathbf{u} \in \{\mathbf{u} \in [H^1(\Omega)]^3 |\ u_i = u_i^D \text{ on } \Gamma_D^{u_i}\}$ such that (2.42) is fulfilled for all $\bar{\mathbf{u}} \in V_0$.

2.4 Poroelastic solid

In poroelasticity, the coupled mechanics of deformation of the solid matrix and the fluid flow in the pore network are considered. The first poroelastic model was developed by von Terzaghi in 1927 [177], who investigated consolidation using a one-dimensional model. In 1941, Biot published a three-dimensional consolidation theory [21], which was extended to anisotropic material behavior in 1955 [22]. A theory for wave propagation in poroelastic media was published in 1956 by Biot [23, 24].

A theory strictly based on thermodynamic principles is the Theory of Porous Media (TPM). It is based on the Theory of Mixtures [28] and the concept of volume fractions. Following this approach, Bowen [29, 30] described fluid-saturated porous media considering incompressible as well as compressible constituents. Subsequent developments of the TPM were mainly motivated by geomechanics. We refer to [58] and [69] for a presentation of these developments.

Although the Biot theory is based on engineering intuition rather than on a consistent thermodynamic derivation, it enjoys a wide acceptance among engineers. Nevertheless, assuming linear models, the Biot theory and the TPM have almost the same governing equations [155]. Since many developments motivated by the modeling of sound absorbing materials are based on the Biot theory, we will use this theory in the present thesis.

Biot Theory Following Biot [23], we consider a fully saturated porous medium. Therefore, we define the bulk volume V, the solid volume V^s, and the fluid volume V^f such that $V = V^s + V^f$. It is assumed that the fluid can move within the interconnected void space V^f, whereas the sealed void space is part of V^s. Assuming a statistically isotropic homogeneous material, we can define the effective porosity as

$$\phi = \frac{V^f}{V}, \tag{2.44}$$

which we call simply porosity in the following. The strain tensor for the elastic skeleton are computed analogously to the pure elastic case

$$\boldsymbol{\epsilon}^s = \frac{1}{2}\left((\nabla \mathbf{u}^s) + (\nabla \mathbf{u}^s)^\top\right), \tag{2.45}$$

where $\mathbf{u}^s$ denotes the solid displacement. The volumetric strain in the fluid is given by

$$\epsilon^f = \nabla \cdot \mathbf{U}, \tag{2.46}$$

where $\mathbf{U}$ denotes the fluid displacement. The constitutive law for the stress tensor in the solid skeleton is

$$\boldsymbol{\sigma}^s = 2\mu\, \boldsymbol{\epsilon}^s + \left(\lambda + \frac{Q^2}{R}\right) \mathrm{tr}(\boldsymbol{\epsilon}^s)\, \mathbf{I} + Q\, \epsilon^f\, \mathbf{I}, \tag{2.47}$$

and for the fluid phase

$$\boldsymbol{\sigma}^f = \left(Q\, \mathrm{tr}(\epsilon^s) + R\, \epsilon^f\right) \mathbf{I}. \tag{2.48}$$

The parameters λ and μ are the usual Lamé constants. The parameters Q and R consider a volumetric coupling between the solid skeleton and the fluid phase. Considering the micro-mechanical level [63], they can be expressed

$$\begin{aligned} Q &= \frac{\phi(\alpha - \phi)(K^s)^2 K^f}{K^f(K^s - K) + \phi K^s(K^s - K^f)}, \\ R &= \frac{\phi^2 (K^s)^2 K^f}{K^f(K^s - K) + \phi K^s(K^s - K^f)}, \end{aligned} \tag{2.49}$$

where K^s, K^f and K are the bulk moduli of the solid and fluid constituents and the skeleton respectively. Assuming an inviscid fluid at macroscopic scale, the relation of fluid stress and the pore pressure is given by

$$\boldsymbol{\sigma}^f = -\phi\, p\mathbf{I}. \tag{2.50}$$

The partial momentum balances are given by

$$\nabla \cdot \boldsymbol{\sigma}^s = \rho_{11}\ddot{\mathbf{u}} + \rho_{12}\ddot{\mathbf{U}} + b\left(\dot{\mathbf{u}} - \dot{\mathbf{U}}\right), \tag{2.51}$$

and

$$\nabla \cdot \boldsymbol{\sigma}^f = \rho_{12}\ddot{\mathbf{u}} + \rho_{22}\ddot{\mathbf{U}} - b\left(\dot{\mathbf{u}} - \dot{\mathbf{U}}\right). \tag{2.52}$$

Therein, b is the viscose drag, which occurs on a microscopic level due to a relative motion of the solid skeleton and the fluid phase. The densities are defined as

$$\begin{aligned}\rho_{11} &= (1-\phi)\rho_s + \rho_a,\\ \rho_{22} &= \phi\rho_f + \rho_a,\\ \rho_{12} &= -\rho_a,\end{aligned}$$

where ρ_s is the density of the solid, ρ_f is the density of the fluid, and ρ_a is the apparent mass density, which takes inertia coupling effects into account. We compute the apparent mass density by

$$\rho_a = \phi\rho_f(\alpha_\infty - 1), \tag{2.53}$$

where α_∞ is the tortuosity. This structural parameter considers the flow pattern at microscopic level due to the presence of the frame.

Frequency domain. In a next step, we assume harmonic time dependency in order to obtain the equations to be solved later. The momentum balances get

$$\nabla\cdot\boldsymbol{\sigma}^s = -\omega^2(\rho_{11}\mathbf{u} + \rho_{12}\mathbf{U}) + i\omega b(\mathbf{u}-\mathbf{U}) \tag{2.54}$$

and

$$\nabla\cdot\boldsymbol{\sigma}^f = -\omega^2(\rho_{12}\mathbf{u} + \rho_{22}\mathbf{U}) - i\omega b(\mathbf{u}-\mathbf{U}). \tag{2.55}$$

The relative mass flux gets

$$\mathbf{q} = \mathrm{i}\omega\phi\ (\mathbf{U}-\mathbf{u}). \tag{2.56}$$

In the following, the governing equations are treated further in order to make them suitable for a finite element formulation in the variables $\mathbf{u}$ and p. Using (2.50), we compute from (2.55) the fluid displacement

$$\mathbf{U} = \frac{-\phi\nabla p + (\omega^2\rho_{12} + i\omega b)\mathbf{u}}{-\omega^2\rho_{22} + i\omega b}, \tag{2.57}$$

and the relative displacement

$$\mathbf{U}-\mathbf{u} = \frac{-\phi\nabla p + \omega^2\phi\rho_f\mathbf{u}}{-\omega^2\rho_{22} + i\omega b} = \frac{\beta}{\omega^2\rho_f\phi}(-\nabla p + \omega^2\rho_f\mathbf{u}), \tag{2.58}$$

where we have introduced

$$\beta = \frac{\omega^2\rho_f\phi^2}{-\omega^2\rho_{22} + i\omega b}. \tag{2.59}$$

Inserting (2.45), (2.46) and (2.50) in (2.48) and some rearrangement yields

$$\phi\ \nabla\cdot(\mathbf{U}-\mathbf{u}) + \alpha\ \nabla\cdot\mathbf{u} + \frac{\phi^2}{R}p = 0. \tag{2.60}$$

Together with equation (2.58), we get

$$-\frac{\beta}{\omega^2\rho_f}\Delta p + (\beta+\alpha)\,\nabla\cdot\mathbf{u} + \frac{\phi^2}{R}p = 0. \tag{2.61}$$

In (2.47) and (2.48), the partial stress tensors for the solid and fluid phase were used. Another possibility is to use the total stress tensor $\boldsymbol{\sigma}^{\text{tot}} = \boldsymbol{\sigma}^s + \boldsymbol{\sigma}^f$. Then,

$$\boldsymbol{\sigma}^{\text{tot}} = 2\mu\,\boldsymbol{\epsilon}^s + \lambda\,\text{tr}(\boldsymbol{\epsilon}^s)\,\mathbf{I} - \alpha p\,\mathbf{I}, \tag{2.62}$$

where $\alpha = \phi(1+\frac{Q}{R}) = 1-\frac{K}{K_s}$ is the so-called effective stress coefficient [63]. For typical sound absorbing materials used in acoustic applications, the bulk modulus of the elastic solid K_s is very large compared to the bulk modulus of the porous material K. Therefore, it is reasonable to use the approximation $\alpha = 1$. The effective stress is defined as

$$\boldsymbol{\sigma}^{\text{eff}} = \boldsymbol{\sigma}^{\text{tot}} + p\,\mathbf{I}, \tag{2.63}$$

and therefore

$$\boldsymbol{\sigma}^{\text{eff}} = 2\mu\,\boldsymbol{\epsilon}^s + \lambda\,\text{tr}(\boldsymbol{\epsilon}^s)\,\mathbf{I}, \tag{2.64}$$

is in analogy with the pure elastic case. Adding (2.51) and (2.52) and taking (2.57) into account results in

$$\nabla\cdot\boldsymbol{\sigma}^{\text{tot}} + \omega^2\mathbf{u}\left(\rho+\rho_f\beta\right) - \beta\,\nabla p = 0, \tag{2.65}$$

where the bulk density $\rho = (1-\phi)\rho_s + \phi\rho_f$ is introduced.

High frequency correction. In the above equations, fluid flow of Poiseuille type is assumed. In the case of high frequencies, this assumption breaks down. Therefore, the above theory is modified by considering frequency dependent material parameters. Following [92], the frequency dependent viscous drag is given as

$$b(\omega) = \sigma\phi^2 G_J(\omega). \tag{2.66}$$

Here, the relaxation function

$$G_J(\omega) = \sqrt{1+\frac{4i\alpha_\infty^2\eta_f\rho_0\omega}{\sigma^2\Lambda^2\phi^2}} \tag{2.67}$$

is used with the viscous characteristic length Λ, the static flow resistivity σ, and the dynamic viscosity η_f. In order to take thermal effects into account, Champoux and Allard [39] introduced the thermal characteristic length Λ'. Following this approach, the bulk modulus of the fluid becomes frequency dependent

$$K^f(\omega) = \frac{\gamma\,p_0}{\gamma-\frac{\gamma-1}{\alpha'(\omega)}}, \tag{2.68}$$

with the function

$$\alpha'(\omega) = 1 + \frac{8\eta_f}{\mathrm{i}\omega\Lambda'^2 Pr\,\rho_f}\sqrt{1 + \mathrm{i}\rho_f \frac{Pr\Lambda'^2}{16\eta_f}}. \tag{2.69}$$

The Prandtl number Pr is given by

$$Pr = \frac{c_p}{\eta_f \kappa}, \tag{2.70}$$

with the specific heat capacity at constant pressure c_p and the thermal conductivity κ.

Boundary value problem. With the six equations (2.45) to (2.48), (2.51) and (2.52), the Biot theory is complete. In order to state a boundary value problem, boundary conditions are left to be specified. On the boundary of a poroelastic solid, two conditions have to be given. The first condition is on the solid displacement or the total surface traction. Since these quantities are vector-valued, one has to distinguish between different directions in space. For each direction i, either the solid displacement u_i (on $\Gamma_D^{u_i}$) or the total surface traction t_i^{tot} (on $\Gamma_N^{u_i}$) has to be prescribed, such that $\Gamma = \Gamma_D^{u_i} \cup \Gamma_N^{u_i}$. The second condition has to be either a prescribed fluid pressure (on Γ_D^p), or a prescribed normal component of the relative mass flux (on Γ_N^p) such that $\Gamma = \Gamma_D^p \cup \Gamma_N^p$.

The strong form of the poroelastic boundary value problem reads: Given the material parameter ϕ, ρ_s, ρ_f, λ, μ, σ, α_∞, η_f, Λ, Λ' and the domain Ω with boundary $\Gamma = \Gamma_D^{u_i} \cup \Gamma_N^{u_i}$ for $i = 1,2,3$ and $\Gamma = \Gamma_D^p \cup \Gamma_N^p$, let $\mathbf{u}_D$, $\mathbf{t}_N$, p_D, q_N be given functions. Find $\mathbf{u}(x,\omega)$ and $p(x,\omega)$ such that

$$\begin{aligned}
\nabla \cdot \boldsymbol{\sigma}^{\mathrm{tot}} + \omega^2 \mathbf{u}\left(\rho + \rho_f \beta\right) - \beta\,\nabla p = 0 \qquad & \text{in } \Omega, \\
-\frac{\beta}{\omega^2 \rho_f}\Delta p + (\beta + \alpha)\,\nabla \cdot \mathbf{u} + \frac{\phi^2}{R} p = 0 \qquad & \text{in } \Omega, \\
u_i(x,\omega) = u_i^D(x,\omega) \qquad & \text{for } x \in \Gamma_D^{u_i}, \\
t_i^{\mathrm{tot}}(x,\omega) = t_i^N(x,\omega) \qquad & \text{for } x \in \Gamma_N^{u_i}, \\
p(x,\omega) = p_D(x,\omega) \qquad & \text{for } x \in \Gamma_D^p, \\
q_n(x,\omega) = q_N(x,\omega) \qquad & \text{for } x \in \Gamma_N^p.
\end{aligned} \tag{2.71}$$

Weak form. Multiplying (2.61) with a real and scalar-valued test function $\bar{p}$ and integration over the domain gives

$$\int_\Omega \phi\,\nabla \cdot (\mathbf{U} - \mathbf{u})\,\bar{p}\,\mathrm{d}\mathbf{x} + \int_\Omega \left(\alpha\,\nabla \cdot \mathbf{u} + \frac{\phi^2}{R} p\right)\bar{p}\,\mathrm{d}\mathbf{x} = 0. \tag{2.72}$$

Integration by parts of the first term yields

$$-\int_\Omega \phi\ (\mathbf{U}-\mathbf{u})\cdot\nabla\bar{p}\,\mathrm{d}\mathbf{x}+\int_\Gamma \phi\ (\mathbf{U}-\mathbf{u})\cdot\mathbf{n}\ \bar{p}\,\mathrm{d}s_\mathbf{x}+\int_\Omega\left(\alpha\,\nabla\cdot\mathbf{u}+\frac{\phi^2}{R}p\right)\bar{p}\,\mathrm{d}\mathbf{x}=0. \quad (2.73)$$

With the relative mass flux (2.56) and the relative displacement (2.58) we obtain

$$-\int_\Omega \frac{\beta}{\omega^2\rho_f}(-\nabla p+\omega^2\rho_f\mathbf{u})\cdot\nabla\bar{p}\,\mathrm{d}\mathbf{x}+\int_\Gamma\frac{\mathbf{q}\cdot\mathbf{n}}{i\omega}\ \bar{p}\,\mathrm{d}s_\mathbf{x}+\int_\Omega\left(\alpha\,\nabla\cdot\mathbf{u}+\frac{\phi^2}{R}p\right)\bar{p}\,\mathrm{d}\mathbf{x}=0. \quad (2.74)$$

Multiplying (2.65) with a vector valued test function and integration over the domain gives,

$$\int_\Omega \nabla\cdot\boldsymbol{\sigma}^{\mathrm{tot}}\cdot\bar{\mathbf{u}}\,\mathrm{d}\mathbf{x}+\int_\Omega\left(\omega^2\left(\rho+\rho_f\beta\right)\mathbf{u}-\beta\nabla p\right)\cdot\bar{\mathbf{u}}\,\mathrm{d}\mathbf{x}=0. \quad (2.75)$$

Integration by parts of the first term yields

$$-\int_\Omega \boldsymbol{\sigma}^{\mathrm{tot}}:\nabla\bar{\mathbf{u}}\,\mathrm{d}\mathbf{x}+\int_\Gamma \mathbf{t}^{\mathrm{tot}}\cdot\bar{\mathbf{u}}\,\mathrm{d}s_\mathbf{x}+\int_\Omega\left(\omega^2\mathbf{u}\left(\rho+\rho_f\beta\right)-\beta\nabla p\right)\cdot\bar{\mathbf{u}}\,\mathrm{d}\mathbf{x}=0. \quad (2.76)$$

Thus, we can formulate the weak form of the poroelastic boundary value problem: Find $\mathbf{u}\in\{\mathbf{u}\in[H^1(\Omega)]^3|\ u_i=u_i^D \text{ on } \Gamma_D^{u_i}\}$ and $p\in\{p\in H^1(\Omega)|\ p=p_D \text{ on } \Gamma_D^p\}$ such that

$$\begin{aligned}-K_u(\mathbf{u},\bar{\mathbf{u}})+\omega^2\left(\rho+\beta\rho^f\right)M_u(\mathbf{u},\bar{\mathbf{u}})+D(p,\bar{\mathbf{u}})-L(p,\bar{\mathbf{u}})+f_u(\bar{\mathbf{u}})=0,\\ K_p(p,\bar{p})+M_p(p,\bar{p})+D(\bar{p},\mathbf{u})-L(\bar{p},\mathbf{u})+f_p(\bar{p})=0,\end{aligned} \quad (2.77)$$

are fulfilled for all test functions $\bar{\mathbf{u}}$ and $\bar{p}$. The bilinear and linear forms are defined in (2.43) and

$$\begin{aligned}K_p(p,\bar{p})&=\frac{\beta}{\omega^2\rho^f}\int_\Omega\nabla p\cdot\nabla\bar{p}\ \mathrm{d}\mathbf{x},\\ M_p(p,\bar{p})&=\frac{\phi^2}{R}\int_\Omega p\ \bar{p}\ \mathrm{d}\mathbf{x},\\ D(p,\bar{\mathbf{u}})&=\int_\Omega p\,\nabla\cdot\bar{\mathbf{u}}\ \mathrm{d}\mathbf{x},\\ L(p,\bar{\mathbf{u}})&=\beta\int_\Omega\nabla p\cdot\bar{\mathbf{u}}\ \mathrm{d}\mathbf{x},\\ f_u(\bar{\mathbf{u}})&=\int_{\Gamma_N^{u_i}}t_i^N\bar{u}_i\,\mathrm{d}s_\mathbf{x},\\ f_p(\bar{p})&=\int_{\Gamma_N^p}\frac{\mathbf{q}\cdot\mathbf{n}}{i\omega}\ \bar{p}\,\mathrm{d}s_\mathbf{x}.\end{aligned} \quad (2.78)$$

2.5 Coupling conditions

The goal of this section is to develop coupling conditions between the physical models introduced. In Figure 2.1 the abstract setting of coupled continua is depicted. The domains Ω^a, Ω^e, Ω^p refer to an acoustic fluid, to an elastic solid and to a poroelastic solid respectively. The boundary of Ω^a is denoted by $\Gamma^a = \Gamma^a_D \cup \Gamma^a_N \cup \Gamma^{ae} \cup \Gamma^{ap}$ and is the union of four non-overlapping parts. In view of all three models, Γ^o_D and Γ^o_N are the Dirichlet and the Neumann boundary of the domain Ω^o, $o \in \{a,e,p\}$. Γ^{ae} and Γ^{ap} denote the coupling boundary of the acoustic fluid domain Ω^a with the elastic solid domain Ω^e and the poroelastic solid domain Ω^p. The boundary of Ω^e is denoted by $\Gamma^e = \Gamma^e_D \cup \Gamma^e_N \cup \Gamma^{ae} \cup \Gamma^{ep}$, whereas the boundary of Ω^p is $\Gamma^p = \Gamma^p_D \cup \Gamma^p_N \cup \Gamma^{ap} \cup \Gamma^{ep}$. The coupling boundary between Ω^e and Ω^p is Γ^{ep}. Before we consider the coupling of different models, we examine the

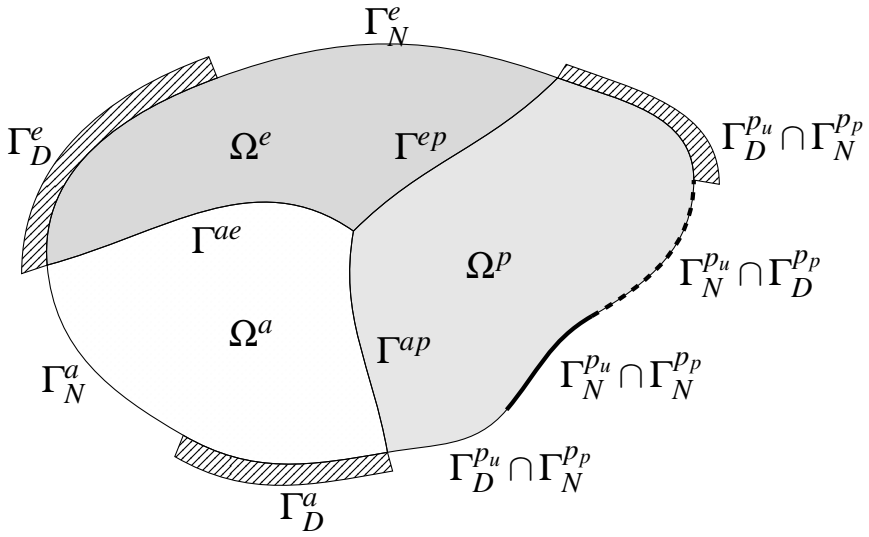

Figure 2.1: Coupled continua: acoustic fluid continuum Ω^a, elastic solid continuum Ω^e, poroelastic solid continuum Ω^p

coupling of two elastic continua. The coupling of two elastic continua (Ω_1, Ω_2) over the common interface Γ yields two conditions. The first condition which has to hold is the continuity of the displacements

$$\mathbf{u}^{(1)} = \mathbf{u}^{(2)} \quad \text{on } \Gamma. \tag{2.79}$$

The second condition is the equilibrium of forces, which results in

$$\mathbf{t}^{(1)} + \mathbf{t}^{(2)} = \mathbf{0} \quad \text{on } \Gamma. \tag{2.80}$$

In the case of an *acoustic fluid - elastic solid* interface Γ^{ae} also two coupling conditions are necessary. According to the inviscid assumption for the acoustic fluid, no shear stresses

occur in the fluid. Hence, particles of the fluid can move tangential to the interface without resistance. Therefore, only the normal displacements are continuous

$$\mathbf{u}^a \cdot \mathbf{n} = \mathbf{u}^e \cdot \mathbf{n}. \tag{2.81}$$

Due to (2.57), we can express the fluid displacement through the pressure $\mathbf{u}^a = \frac{\rho^a}{\omega^2}\nabla p$. Thus, the coupling condition gets

$$\frac{\rho^a}{\omega^2}\nabla p^a \cdot \mathbf{n} = \mathbf{u}^e \cdot \mathbf{n} \quad \text{on } \Gamma^{ae}. \tag{2.82}$$

The traction on the interface resulting from the scalar pressure field in the fluid is $\mathbf{t}^a = -p^a\mathbf{n}$. Thus, the equilibrium of forces yields

$$\mathbf{t}^e = -p^a\mathbf{n} \quad \text{on } \Gamma^{ae}, \tag{2.83}$$

where the normal vector is the outward normal vector of the elastic domain.

On an *acoustic fluid - poroelastic solid* interface Γ^{ap}, three coupling conditions have to be fulfilled. The continuity of normal displacements implies

$$\mathbf{u}^a \cdot \mathbf{n} = \mathbf{u}^p \cdot \mathbf{n} \quad \text{on } \Gamma^{ap}, \tag{2.84}$$

where $\mathbf{u}^p = (1-\phi)\mathbf{u} + \phi\mathbf{U}$ is the displacement of a 'poroelastic particle'. Using the relative mass flux defined in (2.56) and (2.58), the coupling condition gets

$$\frac{\nabla p^a \cdot \mathbf{n}}{\rho^a \omega^2} = \mathbf{u}^s \cdot \mathbf{n} + \frac{1}{\mathrm{i}\omega}\mathbf{q} \cdot \mathbf{n} \quad \text{on } \Gamma^{ap}. \tag{2.85}$$

The second condition is given by the equilibrium of forces. The surface traction induced by the scalar pressure in the acoustic fluid has to be balanced with the total traction in the poroelastic solid

$$-p^a\mathbf{n} = \mathbf{t}^{tot} \quad \text{on } \Gamma^{ap}, \tag{2.86}$$

where the normal vector is the outward normal vector of the poroelastic domain. The third condition ensures the continuity of the pressure fields. Hence,

$$p^a = p^p \quad \text{on } \Gamma^{ap}. \tag{2.87}$$

The remaining combination is an *elastic solid - poroelastic solid* interface Γ^{ep}. The elastic solid and the poroelastic solid are able to resist shear forces. Therefore, no relative motion between the two solid phases are allowed

$$\mathbf{u}^s = \mathbf{u}^e \quad \text{on } \Gamma^{ep}. \tag{2.88}$$

The elastic domain represents an impervious interface for the fluid in the poroelastic solid. Therefore, the relative mass flux normal to the interface has to be zero

$$\mathbf{q} \cdot \mathbf{n} = 0 \quad \text{on } \Gamma^{ep}. \tag{2.89}$$

As a third condition, the equilibrium of forces demands

$$\mathbf{t}^e + \mathbf{t}^{tot} = \mathbf{0} \quad \text{on } \Gamma^{ep}. \tag{2.90}$$

3 DIFFERENTIAL GEOMETRY AND SHELL MODELS

In this chapter, we specify the physical models in the context of shell analysis. Shells are thin-walled structures with one dimension significantly smaller than the other two. In this setting, solutions to the general three-dimensional problem are difficult to obtain, both analytically and numerically. This motivates the simplification of the three-dimensional equations to two-dimensional ones with the goal of solving a simpler problem. This can be solved analytically or with reduced numerical effort. Due to the fact that no analytic solutions are available for general shells, a huge amount of work has been devoted to the development of special finite elements for shell structures. Therefore, many procedures are related to the FEM. These will be discussed in section 4.1. In the present thesis, we assume that the shell is given as a thin region related to a reference surface. We treat the cases where this reference surface is given parametrically or implicitly as the zero level of a given level-set function. In both cases, in order to apply the FEM, the parametrization of the reference surface is needed. In the first case, it is given, whereas in the second case, it is constructed numerically from the level-set function, which we explain in all details in section 4.1.3. Nevertheless, the exact geometry is preserved in both cases. In the following, we present the three-dimensional differential geometry and the differential geometry of shells to the extent to which it is needed in our analysis. Furthermore, we review classical shell models and present an extension thereof to poroelastic shells.

3.1 Differential geometry

In this section, we present the notations and definitions of differential geometry, which will be used in the rest of the present thesis. First, the three-dimensional differential geometry is considered. As a second step, two-dimensional surfaces immersed in the three-dimensional space are treated. This forms the basis for the differential geometry of shells, where the three-dimensional geometry of shells is induced by the geometry of the two-dimensional surface. The differential geometry in the context of thin-walled structures is exhaustively discussed in [18] and [46], among others.

Let $\mathbb{E}^3$ be the three-dimensional Euclidean space equipped with the standard orthonormal basis consisting of the three base vectors $\mathbf{e}_i = \mathbf{e}^i$ and the standard Euclidean scalar product $\mathbf{a} \cdot \mathbf{b}$. We identify a point $x \in \mathbb{E}^3$ with its Cartesian coordinates $\mathbf{x} \in \mathbb{R}^3$.

An important concept in this work is the use of coordinate transformations. Let U denote an open subset of $\mathbb{R}^n$ and $\mathfrak{g} : U \to \mathbb{E}^3$ an injective mapping. Then, for a point x in the open

set $M = \mathfrak{g}(U)$, we write

$$x = \mathfrak{g}(\theta^i), \quad \theta^i \in U, \tag{3.1}$$

and θ^i are the curvilinear coordinates of x. Assuming $\mathfrak{g}$ is differentiable, we can define the three vectors

$$\mathbf{G}_i = \mathfrak{g}_{,i} = \frac{\partial}{\partial \theta^i}\mathfrak{g}. \tag{3.2}$$

We call $\mathfrak{g}$ a parametrization of M, if the vectors $\mathbf{G}_i$ are linearly independent. A parametrization $\mathfrak{g}$ induces a metric on M, where

$$\mathrm{G}_{ij} = \mathbf{G}_i \cdot \mathbf{G}_j \tag{3.3}$$

are the coefficients. We write $[\mathrm{G}_{ij}]$ for the coefficient matrix. Since $\mathbf{G}_i$ are linearly independent, the matrix $[\mathrm{G}_{ij}]$ is invertable and we can define the contravariant components of the metric G^{ij} as the entries of $[\mathrm{G}_{ij}]^{-1}$. Based on the above relations, the contravariant base vectors $\mathbf{G}^i$ are defined as

$$\mathbf{G}^i = G^{ij}\mathbf{G}_j. \tag{3.4}$$

Here, we made use of the Einstein summation convention. Whenever an index occurs once as a superscript and once as a subscript we sum over this index. The base vectors satisfy

$$\mathbf{G}^i \cdot \mathbf{G}^j = \mathrm{G}^{ij}, \quad \mathbf{G}^i \cdot \mathbf{G}_j = \delta^i_j. \tag{3.5}$$

The Kronecker delta δ^j_i is defined as

$$\delta^j_i = \begin{cases} 1 & \text{for} \quad i = j, \\ 0 & \text{for} \quad i \neq j. \end{cases} \tag{3.6}$$

Furthermore, the Jacobi matrix J is defined as the matrix with base vectors as columns,

$$J = [\mathbf{G}_1, \ldots, \mathbf{G}_i]. \tag{3.7}$$

The entry $J[i,j]$ of the Jacobi matrix is given by

$$J[i,j] = J^j_i = \mathbf{G}_i \cdot \mathbf{e}^j, \tag{3.8}$$

and the relation

$$[\mathrm{G}_{ij}] = J^\top J \tag{3.9}$$

holds. The Christoffel symbols of first kind are defined as

$$\Gamma_{ijl} = \mathbf{G}_{i,j} \cdot \mathbf{G}_l = \frac{1}{2}\left(G_{jl,i} + G_{il,j} - G_{ij,l}\right), \tag{3.10}$$

whereas the Christoffel symbols of second kind are

$$\Gamma_{ij}{}^k = \Gamma_{ijl} G^{lk}. \tag{3.11}$$

They satisfy the symmetry relation

$$\begin{aligned} \Gamma_{ij}{}^{l} &= \Gamma_{ji}{}^{l} \\ \Gamma_{ijl} &= \Gamma_{jil} \end{aligned} \tag{3.12}$$

and

$$\mathbf{G}^{p}_{,i} = -\Gamma_{ij}{}^{p}\mathbf{G}^{j} \tag{3.13}$$

holds.

Geometry of surfaces in $\mathbb{E}^3$. Let $\bar{\Omega}$ be a two-dimensional surface immersed in $\mathbb{E}^3$. Assuming $\bar{\Omega}$ is parametrically given, we have

$$\begin{aligned} \overline{\mathfrak{g}}:\ \bar{U} \subset \mathbb{R}^2 &\to \bar{\Omega} \subset \mathbb{R}^3 \\ (\theta^1,\theta^2) &\mapsto \overline{\mathfrak{g}}(\theta^1,\theta^2). \end{aligned} \tag{3.14}$$

The two base vectors spanning the tangential plane to the surface are given by

$$\overline{\mathbf{G}}_\alpha = \frac{\partial}{\partial\theta^\alpha}\overline{\mathfrak{g}} \qquad \alpha = 1,2. \tag{3.15}$$

This allows us to define the unit normal vector to $\bar{\Omega}$ as

$$\mathbf{n} = \frac{\tilde{\mathbf{n}}}{\|\tilde{\mathbf{n}}\|}, \quad \tilde{\mathbf{n}} = \overline{\mathbf{G}}_1 \times \overline{\mathbf{G}}_2. \tag{3.16}$$

Due to the definition of the normal vector as a unit vector, we have $\mathbf{n}\cdot\mathbf{n} = 1$. Taking the derivative with respect to θ^α, it yields $\frac{\partial}{\partial\theta^\alpha}(\mathbf{n}\cdot\mathbf{n}) = \mathbf{n}_{,\alpha}\cdot\mathbf{n} + \mathbf{n}\cdot\mathbf{n}_{,\alpha} = 0$. Thus, the derivatives of the normal vector are in the tangent plane of the surface. Expressing the derivatives of the normal vector trough a linear combination of the tangent vectors yields

$$\mathbf{n}_{,\alpha} = -h^\beta_\alpha \overline{\mathbf{G}}_\beta, \tag{3.17}$$

where

$$h_{\alpha\beta} = -\overline{\mathbf{G}}_\alpha\cdot\mathbf{n}_{,\beta}, \quad \text{and} \quad h^\beta_\alpha = \overline{G}^{\beta\gamma}h_{\alpha\gamma}. \tag{3.18}$$

These relations are known as the Weingarten equations, first established in [179]. The functions $h_{\alpha\beta}$ are the coefficients of the second fundamental form. Differentiation of $\mathbf{G}_\alpha\cdot\mathbf{n} = 0$ yields

$$h_{\alpha\beta} = -\overline{\mathbf{G}}_\alpha\cdot\mathbf{n}_{,\beta} = \mathbf{G}_{\alpha,\beta}\cdot\mathbf{n}. \tag{3.19}$$

Two important measures of curvature are the mean curvature H and the Gaussian curvature K, which are computed by

$$\begin{aligned} H &= \frac{1}{2}h^\gamma_\gamma, \\ K &= h^1_1 h^2_2 - h^2_1 h^1_2. \end{aligned} \tag{3.20}$$

Geometry of shells. In the present work, we consider a shell as a thee-dimensional body Ω given by the parametrization

$$\begin{aligned} \mathfrak{g}:\ (\bar{U}\times T)\subset\mathbb{R}^3 &\to \Omega\subset\mathbb{R}^3 \\ (\theta^1,\theta^2)\times\theta^3 &\mapsto \mathfrak{g}(\theta^1,\theta^2,\theta^3)=\overline{\mathfrak{g}}(\theta^1,\theta^2)+\theta^3\,\mathbf{n}, \end{aligned} \tag{3.21}$$

where $T\subset\mathbb{R}$ is the interval $T=[t_{bot},t_{top}]$. The situation is depicted in Figure 3.1. In view

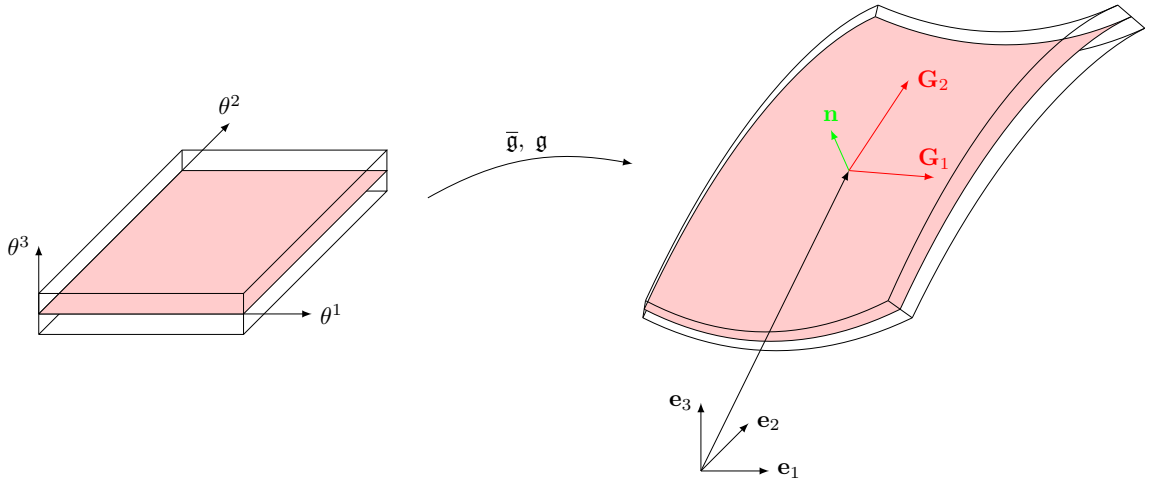

Figure 3.1: Parametrization of a shell

of (3.17), the covariant base vectors are

$$\mathbf{G}_i=\mathfrak{g}_{,i}=\begin{cases}\overline{\mathfrak{g}}_{,\alpha}+\mathbf{n}_{,\alpha}\theta^3=(\delta^\beta_\alpha-\theta^3h^\beta_\alpha)\overline{\mathbf{G}}_\beta & \text{if } i=\alpha=1,2\\ \mathbf{n} & \text{if } i=3\end{cases}. \tag{3.22}$$

Typically, $\mu^\beta_\alpha=\delta^\beta_\alpha-\theta^3h^\beta_\alpha$ is called the shifter. The components of the covariant metric tensor are given by

$$\begin{aligned} \mathrm{G}_{\alpha\beta}&=\mathbf{G}_\alpha\cdot\mathbf{G}_\beta=\left(\delta^\gamma_\alpha-\theta^3h^\gamma_\alpha\right)\overline{\mathbf{G}}_\gamma\cdot\left(\delta^\lambda_\beta-\theta^3h^\lambda_\beta\right)\overline{\mathbf{G}}_\lambda\\ &=\overline{G}_{\alpha\beta}-2\left(\theta^3\right)h_{\alpha\beta}+(\theta^3)^2h_{\alpha\gamma}h^\gamma_\beta\\ \mathrm{G}_{\alpha3}&=\mathrm{G}_{3\alpha}=0\\ \mathrm{G}_{33}&=1. \end{aligned} \tag{3.23}$$

In order to compute the components of the covariant metric tensor, we compute the determinant of the Jacobi matrix. We use the notation $\det([g_{ij}])=\langle g_{ij}\rangle$. Thus,

$$\begin{aligned} \langle J\rangle&=\left\langle\overline{\mathbf{G}}_1,\overline{\mathbf{G}}_2,\mathbf{n}\right\rangle-\theta^3\left(\left\langle h^\alpha_1\overline{\mathbf{G}}_\alpha,\overline{\mathbf{G}}_2,\mathbf{n}\right\rangle+\left\langle\overline{\mathbf{G}}_1,h^\alpha_2\overline{\mathbf{G}}_\alpha,\mathbf{n}\right\rangle\right)+(\theta^3)^2\left\langle h^\gamma_1\overline{\mathbf{G}}_\gamma,h^\alpha_2\overline{\mathbf{G}}_\alpha,\mathbf{n}\right\rangle\\ &=\sqrt{\langle\overline{G}_{\alpha\beta}\rangle}\left(1-2H\theta^3+K(\theta^3)^2\right), \end{aligned} \tag{3.24}$$

where we have used the following properties of the determinant:

- Linearity in the columns: $\langle A_1 + A_2, B, C\rangle = \langle A_1, B, C\rangle + \langle A_2, B, C\rangle$ and $\langle \alpha A, B, C\rangle = \alpha\langle A, B, C\rangle$.
- If two columns are equal, the determinant is zero: $\langle A, A, B\rangle = 0$.
- Multiplicativity: $\left\langle \mathrm{G}_{ij}\right\rangle = \left\langle J^\top J\right\rangle = \left\langle J^\top\right\rangle \langle J\rangle = \langle J\rangle^2$.

The components of the contravariant metric are given by

$$\begin{aligned}
[\mathrm{G}^{\alpha\beta}] = [\mathrm{G}_{\alpha\beta}]^{-1} &= \frac{\mathrm{adj}([\mathrm{G}_{\alpha\beta}])}{\det([\mathrm{G}_{\alpha\beta}])} = \frac{\mathrm{adj}([\overline{G}_{\alpha\beta}]) - 2\,\theta^3\,\mathrm{adj}([h_{\alpha\beta}]) + (\theta^3)^2\mathrm{adj}([h_{\alpha\gamma}h^\gamma_\beta])}{\left\langle \overline{G}_{\alpha\beta}\right\rangle (1 - 2H\theta^3 + K(\theta^3)^2)^2} \\
\mathrm{G}^{\alpha 3} &= \mathrm{G}^{3\alpha} = 0 \\
\mathrm{G}^{33} &= 1,
\end{aligned} \tag{3.25}$$

where $\mathrm{adj}([\overline{G}_{\alpha\beta}])$ is the adjugate matrix of $[\overline{G}_{\alpha\beta}]$. Since $[\overline{G}_{\alpha\beta}]$ is a 2×2 matrix,

$$\mathrm{adj}([\overline{G}_{\alpha\beta}]) = \begin{bmatrix} \overline{G}_{22} & -\overline{G}_{12} \\ -\overline{G}_{12} & \overline{G}_{11} \end{bmatrix}. \tag{3.26}$$

In the following, we study the gradient and the divergence operator. In local coordinates, the gradient of a scalar-valued function is

$$\nabla f = f_{,i}\mathbf{G}^i = f_{,\alpha}\mathbf{G}^\alpha + f_{,3}\mathbf{n}. \tag{3.27}$$

Next, the gradient of vector-valued function $\mathbf{v}$ in local coordinates is stated. Assuming $\mathbf{v} = v_i\mathbf{e}^i$, the gradient is

$$\nabla\mathbf{v} = v_{i,j}\,\mathbf{e}^i \otimes \mathbf{G}^j = v_{i,\alpha}\,\mathbf{e}^i \otimes \mathbf{G}^\alpha + v_{i,3}\,\mathbf{e}^i \otimes \mathbf{n}. \tag{3.28}$$

In the case of $\mathbf{v} = v\,\mathbf{n}$, we have

$$\nabla\mathbf{v} = v_{,j}\,\mathbf{n}\otimes\mathbf{G}^j + v\,\mathbf{n}_{,j}\otimes\mathbf{G}^j = v_{,j}\,\mathbf{n}\otimes\mathbf{G}^j - v\,h^\beta_\alpha\mathbf{G}_\beta\otimes\mathbf{G}^\alpha. \tag{3.29}$$

We define the divergence operator as the adjoint to the gradient operator. In local coordinates, we have for $\vec{X} = X_i\mathbf{G}^i$ [148],

$$\begin{aligned}
<\vec{X}, \nabla f>_{L_2} &= \int_M \vec{X}\cdot\nabla f\,\mathrm{d}V \\
&= \int_U X_i\mathbf{G}^i\cdot f_{,j}\mathbf{G}^j\sqrt{\det\mathrm{G}}\,\mathrm{d}\theta \\
&= \int_U X_i f_{,j}\mathrm{G}^{ij}\sqrt{\det\mathrm{G}}\,\mathrm{d}\theta \\
&= -\int_U f\frac{1}{\sqrt{\det\mathrm{G}}}\left(X_i\mathrm{G}^{ij}\sqrt{\det\mathrm{G}}\right)_{,j}\sqrt{\det\mathrm{G}}\,\mathrm{d}\theta \\
&= <-\frac{1}{\sqrt{\det\mathrm{G}}}\left(X_i\mathrm{G}^{ij}\sqrt{\det\mathrm{G}}\right)_{,j}, f>_{L_2}.
\end{aligned} \tag{3.30}$$

Thus,

$$\nabla \cdot \vec{X} = \frac{1}{\sqrt{\det \mathrm{G}}} \left(X_i \mathrm{G}^{ij} \sqrt{\det \mathrm{G}} \right)_{,j}. \tag{3.31}$$

By combination of (3.27) and (3.31), the Laplacian of a scalar-valued function f is given as

$$\Delta f = \frac{1}{\sqrt{\det \mathrm{G}}} \left(f_{,i} \mathrm{G}^{ij} \sqrt{\det \mathrm{G}} \right)_{,j}. \tag{3.32}$$

Following the lines in (3.30), the divergence in case of $\vec{X} = X\mathbf{n}$ is given in local coordinates as

$$\nabla \cdot \vec{X} = \frac{1}{\sqrt{\det \mathrm{G}}} \left(X \sqrt{\det \mathrm{G}} \right)_{,3} = X_{,3} + X \frac{2(\theta^3 K - H)}{1 - 2H\theta^3 + K(\theta^3)^2} = X_{,3} + X\iota, \tag{3.33}$$

with

$$\iota = \frac{2(\theta^3 K - H)}{1 - 2H\theta^3 + K(\theta^3)^2}. \tag{3.34}$$

In the same way, we find the divergence in case of $\vec{X} = X_i \mathbf{e}^i$ as

$$\nabla \cdot \vec{X} = \frac{1}{\sqrt{\det \mathrm{G}}} \left(X_i (\mathbf{e}^i \cdot \mathbf{G}^j) \sqrt{\det \mathrm{G}} \right)_{,j} = X_{i,j} J^i_k \mathrm{G}^{kj} + \frac{X_i}{\sqrt{\det \mathrm{G}}} \left((\mathbf{e}^i \cdot \mathbf{G}^j) \sqrt{\det \mathrm{G}} \right)_{,j}. \tag{3.35}$$

This expression can be further simplified. In view of (3.13), direct calculation of the last term gives

$$\begin{aligned} \left((\mathbf{e}^i \cdot \mathbf{G}^k) \sqrt{\det G} \right)_{,k} &= (\mathbf{e}^i_{,k} \cdot \mathbf{G}^k) \sqrt{\det G} + (\mathbf{e}^i \cdot \mathbf{G}^k_{,k}) \sqrt{\det G} + (\mathbf{e}^i \cdot \mathbf{G}^k) (\sqrt{\det G})_{,k} \\ &= (\mathbf{e}^i \cdot -\Gamma_{kl}{}^k \mathbf{G}^l) \sqrt{\det G} + (\mathbf{e}^i \cdot \mathbf{G}^k) \left(\frac{(\det G)_{,k}}{2\sqrt{\det G}} \right). \end{aligned} \tag{3.36}$$

Using Jacobi's formula $\frac{\mathrm{d}}{\mathrm{d}t} \det A(t) = \mathrm{tr}\left(\mathrm{adj}(A(t)) \frac{\mathrm{d}}{\mathrm{d}t} A(t) \right)$ for a matrix A, and the representation of the adjugate $\mathrm{adj}\, A = A^{-1} \det A$, we have

$$(\det G)_{,k} = \det G \, G^{ij} G_{ij,k} = \det G \, G^{ij} (\Gamma_{kij} + \Gamma_{kji}) = 2 \det G \, \Gamma_{ki}{}^i. \tag{3.37}$$

Thus,

$$\left((\mathbf{e}^j \cdot \mathbf{G}^k) \sqrt{\det G} \right)_{,k} = 0, \tag{3.38}$$

and

$$\nabla \cdot (X_j \mathbf{e}^j) = X_{i,j} J^i_k \mathrm{G}^{kj}. \tag{3.39}$$

3.2 Elastic shells

In this section, we review shell models of elastic thin-walled structures. Shells are characterized by having one extension which is considerably smaller than the extension in the other two directions.

Three-dimensional elastic shell problem. We consider the operators in the elastic solid boundary value problem in local coordinates assuming a general parametrization. Assuming $\boldsymbol{\sigma} = \sigma^{kl}\,\mathbf{G}_k \otimes \mathbf{G}_l$, the divergence of the stress tensor can be computed by

$$\nabla \cdot \boldsymbol{\sigma} = -\left(\sigma^{jl}_{,j} + \sigma^{kl}\Gamma_{kj}{}^{j} + \sigma^{jk}\Gamma_{kj}{}^{l}\right)\mathbf{G}_l. \tag{3.40}$$

Representing the linearized strain tensor in the form $\boldsymbol{\epsilon} = \epsilon_{ij}\,\mathbf{G}^i \otimes \mathbf{G}^j$, the components are given by

$$\epsilon_{ij} = \frac{1}{2}\left(\mathbf{G}_i \cdot \frac{\partial \mathbf{u}}{\partial \theta^j} + \mathbf{G}_j \cdot \frac{\partial \mathbf{u}}{\partial \theta^i}\right). \tag{3.41}$$

The components of the isotropic elasticity tensor $\mathbb{C} = \mathbb{C}^{ijkl}\,\mathbf{G}_i \otimes \mathbf{G}_j \otimes \mathbf{G}_k \otimes \mathbf{G}_l$ are given by

$$\mathbb{C}^{klij} = \lambda \mathrm{G}^{ij}\mathrm{G}^{kl} + \mu\left(\mathrm{G}^{ik}\mathrm{G}^{jl} + \mathrm{G}^{il}\mathrm{G}^{kj}\right). \tag{3.42}$$

In the case of a shell-like parametrization (3.21), the components of the linearized strain tensor are

$$\begin{aligned}
\epsilon_{\alpha\beta} &= \frac{1}{2}\left(\mu^{\varsigma}_{\alpha}\overline{\mathbf{G}}_{\varsigma} \cdot \frac{\partial \mathbf{u}(\theta^j)}{\partial \theta^\beta} + \mu^{\varsigma}_{\beta}\overline{\mathbf{G}}_{\varsigma} \cdot \frac{\partial \mathbf{u}(\theta^j)}{\partial \theta^\alpha}\right),\\
\epsilon_{\alpha 3} &= \frac{1}{2}\left(\mu^{\varsigma}_{\alpha}\overline{\mathbf{G}}_{\varsigma} \cdot \frac{\partial \mathbf{u}(\theta^j)}{\partial \theta^3} + \mathbf{n} \cdot \frac{\partial \mathbf{u}(\theta^j)}{\partial \theta^\alpha}\right),\\
\epsilon_{33} &= \frac{\partial \mathbf{u}(\theta^j)}{\partial \theta^3} \cdot \mathbf{n}.
\end{aligned} \tag{3.43}$$

In view of (3.23), the relations (3.42) can be evaluated to

$$\begin{aligned}
\mathbb{C}^{\alpha\beta\gamma\varphi} &= \lambda \mathrm{G}^{\alpha\beta}\mathrm{G}^{\gamma\varphi} + \mu\left(\mathrm{G}^{\alpha\gamma}\mathrm{G}^{\beta\varphi} + \mathrm{G}^{\alpha\varphi}\mathrm{G}^{\beta\gamma}\right),\\
\mathbb{C}^{\alpha\beta 33} &= \mathbb{C}^{33\alpha\beta} = \lambda \mathrm{G}^{\alpha\beta},\\
\mathbb{C}^{3\alpha 3\beta} &= \mathbb{C}^{3\alpha\beta 3} = \mathbb{C}^{\alpha 33\beta} = \mathbb{C}^{\alpha 3\beta 3} = \mu \mathrm{G}^{\alpha\beta},\\
\mathbb{C}^{3\alpha\beta\gamma} &= \mathbb{C}^{\alpha 3\beta\gamma} = \mathbb{C}^{\alpha\beta 3\gamma} = \mathbb{C}^{\alpha\beta\gamma 3} = 0,\\
\mathbb{C}^{333\alpha} &= \mathbb{C}^{33\alpha 3} = \mathbb{C}^{3\alpha 33} = \mathbb{C}^{\alpha 333} = 0,\\
\mathbb{C}^{3333} &= \lambda + 2\mu.
\end{aligned} \tag{3.44}$$

Up to this point, no approximation in the equations of linearized elasticity has been introduced. In the following, we consider shell models which simplify the three-dimensional equations introducing an approximation.

Shell models. There have been many different approaches in the analysis of shells, and providing a complete view on the topic seems impossible. Bischoff and coworkers formulate this in their review article [26] with the following words: “The series of names in

connection with shell formulations could be continued forever; there are very few topics in structural mechanics where so many investigations have been published. Even for experts, it is hardly possible to have an overall view on the number of special finite element models developed so far. This is a strong indication for the complexity of the involved mechanics on the one hand and their practical relevance on the other hand."

This citation and the titles of the review articles [26] and [37] indicate the tight coupling of the FEM and shell models in shell analysis. The different approaches in shell analysis can be classified in three groups with different starting points but similar results. The first approach is based on the idea of the Cosserat continua [53], where additionally to classical continuum mechanics, couple stresses and rotational degrees of freedom are considered. In their monograph from 1909 [54], the Cosserats describe the mechanics of deformable surfaces among the mechanics of rods and generalized continua. If the shell is modeled with a deformable surface, it is assumed to be two-dimensional a priori. We refer to [7] and references therein for a description of this approach. The second possibility is to perform a dimension reduction of the governing three-dimensional equations. The resulting two-dimensional model is a simplified model in the sense that the full three-dimensional model is approximated by means of simpler (easier to solve) equations. The third large group of shell analysis approaches is constituted by the pure numerical ones. Here, the three-dimensional equations are discretized directly by means of finite elements, taking the characteristics of shells into account. We will review some of these approaches in Section 4.1.

In the rest of this section, we focus on shell models obtained by dimension reduction. These two-dimensional shell models approximate a three-dimensional master model. The approximation yields an error, which we call modeling error [20] and is defined as the difference of the exact solution of the three-dimensional equations u^{3d} and the exact solution of the shell model u^M. In order to be able to judge if a shell model is valid or not, the asymptotic correctness plays a fundamental role. A shell model is said to be asymptotically correct, if the modeling error decreases, when the thickness t of the shell decreases, *i.e.* the solution of the shell model converges to the solution of the three-dimensional equations,

$$\lim_{t\to 0} ||u^{3d} - u^M|| \to 0. \tag{3.45}$$

The first accepted theory was given by Kirchhoff [100] in 1850. Regarding the earlier history of work devoted to shell analysis, we refer to [26]. Kirchhoff considered the special case of plates, *i.e.* flat shells. He deduced his theory from *ad hoc* assumptions. A formal proof of the asymptotic correctness of Kirchhoff's theory was published by Morgenstern [122] in 1959. In 1888, Love [113] extended Kirchhoff's work to shells. Due to these developments, the three-dimensional displacement field

$$\mathbf{u}^{KL}(\mathbf{w}|\theta^1,\theta^2,\theta^3) = \left(w_\alpha - \theta^3(w_{3,\alpha} + h^\beta_\alpha w_\beta)\right)\overline{\mathbf{G}}^\alpha + w_3\mathbf{n} \tag{3.46}$$

of a vector field $\mathbf{w} = w_\alpha \overline{\mathbf{G}}^\alpha + w_3 \mathbf{n}$ defined on the reference surface is called Kirchhoff-Love displacement field. Probably the simplest, but asymptotically correct model in linear thin shell analysis is Koiter's linear shell theory [102, 103]: Let $\bar{U} \subset \mathbb{R}^2$, $\overline{\mathfrak{g}}(\bar{U})$ be the mid-surface and $\mathbf{p}$ the load. The shell thickness is $2t$. Find $\mathbf{u}^K \in V^K$ such that

$$B_M(\mathbf{u}^K, \boldsymbol{\eta}) + B_B(\mathbf{u}^K, \boldsymbol{\eta}) = \ell_K(\boldsymbol{\eta}) \text{ for all } \boldsymbol{\eta} \in V^K, \tag{3.47}$$

where

$$\begin{aligned} V^K &= \{\boldsymbol{\eta} \in H^1(\bar{U}) \times H^1(\bar{U}) \times H^2(\bar{U}) \mid \boldsymbol{\eta} = \eta_{3,n} = 0 \text{ on } \gamma_0\}, \\ B_M(\mathbf{u}^K, \boldsymbol{\eta}) &= \epsilon \int_{\bar{U}} a^{\alpha\beta\gamma\varphi}\, \gamma_{\gamma\varphi}(\mathbf{u}^K) \gamma_{\alpha\beta}(\boldsymbol{\eta}) \sqrt{\langle \overline{G}_{\alpha\beta} \rangle}\, \mathrm{d}\bar{U}, \\ B_B(\mathbf{u}^K, \boldsymbol{\eta}) &= \frac{\epsilon^3}{3} \int_{\bar{U}} a^{\alpha\beta\gamma\varphi}\, \rho_{\gamma\varphi}(\mathbf{u}^K) \rho_{\alpha\beta}(\boldsymbol{\eta}) \sqrt{\langle \overline{G}_{\alpha\beta} \rangle}\, \mathrm{d}\bar{U}, \\ \ell_K(\boldsymbol{\eta}) &= \int_{\bar{U}} \mathbf{p} \cdot \boldsymbol{\eta} \sqrt{\langle \overline{G}_{\alpha\beta} \rangle}\, \mathrm{d}\bar{U}, \end{aligned} \tag{3.48}$$

and

$$\begin{aligned} a^{\alpha\beta\gamma\varphi} &= \frac{4\lambda\mu}{\lambda + 2\mu} \overline{G}^{\alpha\beta} \overline{G}^{\gamma\varphi} + 2\mu \left(\overline{G}^{\alpha\gamma} \overline{G}^{\beta\varphi} + \overline{G}^{\alpha\varphi} \overline{G}^{\beta\gamma} \right) \\ \gamma_{\alpha\beta}(\boldsymbol{\eta}) &= \frac{1}{2} \left(\eta_{\alpha,\beta} + \eta_{\beta,\alpha} \right) - \overline{\Gamma}_{\alpha\beta}^{\gamma} \eta_\gamma - h_{\alpha\beta} \eta_3 \\ \rho_{\alpha\beta}(\boldsymbol{\eta}) &= \eta_{3,\alpha\beta} - \overline{\Gamma}_{\alpha\beta}^{\gamma} \eta_\gamma \eta_{3,\gamma} + h_\beta^\gamma (\eta_{\gamma,\alpha} - \overline{\Gamma}_{\alpha\gamma}^{\varphi} \eta_\varphi) \\ &\quad + h_\alpha^\gamma (\eta_{\gamma,\beta} - \overline{\Gamma}_{\beta\gamma}^{\varphi} \eta_\varphi) + (h_{\beta,\alpha}^\gamma + \overline{\Gamma}_{\alpha\varphi}^{\gamma} h_\beta^\varphi - \overline{\Gamma}_{\beta\alpha}^{\gamma} h_\gamma^\varphi) \eta_\varphi - h_\beta^\gamma h_{\gamma\alpha} \eta_3. \end{aligned} \tag{3.49}$$

In the problem given above, we restricted ourselves to the case of a clamped boundary on $\gamma_0 \subset \partial\bar{U}$. Furthermore, $\eta_{3,n}$ denotes the normal derivative with respect to γ_0. The Koiter model has been justified in [48]. It is interesting to note that the Koiter model is no limit model in the asymptotic sense. In an asymptotic analysis, the principal term is sought in case of vanishing thickness. Depending on the geometry and on the boundary and loading conditions, either a membrane shell [47] or a flexible shell or [50] a generalized membrane shell [49] is the limit model.

Once the solution $\mathbf{u}^K$ of the Koiter model has been obtained, the three-dimensional displacement field can be reconstructed by means of (3.46). This procedure has been analyzed and justified in [109] under distinct assumptions on the loading and boundary conditions. A refined three-dimensional displacement reconstruction was already proposed in [103], where the reconstructed displacement field is quadratic with respect to the thickness. This is refined further, including a reconstruction of the boundary layer in [110].

The solution of the Koiter model is the displacement field of the mid-surface, which can be described by three parameters. Theories with tree unknown parameters are referred to as models of Kirchhoff-Love type or as 3-parameter models [26]. A refined 3-parameter model and reconstruction procedure is given in [107]. Models of the Kirchhoff-Love type are shear rigid. Therefore, these models cannot approximate the full three-dimensional displacement field (cf. [13]) in general loading situations.

In contrast to the thin shell analysis, the thick shell analysis is based on shear deformable theories. The early achievements in this direction in the case of plates were made by Reissner [143, 144] and Mindlin [121]. To honor this, the displacement field

$$\mathbf{u}^{RM}(\mathbf{w},\theta^1,\theta^2,\theta^3) = \mathbf{w} + \theta^3 v_\alpha \overline{\mathbf{G}}^\alpha \tag{3.50}$$

of a field $(\mathbf{w}, v_\alpha)$ defined on the reference surface is called Reissner-Mindlin displacement field. The first acceptable shear deformable theory to determine $(\mathbf{w}, v_\alpha)$ was proposed by Naghdi [123, 124]. Since $(\mathbf{w}, v_\alpha)$ involves five parameters, shear deformable shell models are called models of Reissner-Mindlin type or 5-parameter models [26].

The Koiter model, as well as the Naghdi model can be obtained by inserting the respective kinematics in the three-dimensional equations, performing integration through the thickness, assuming vanishing transverse normal stress and neglecting small terms. In a shell, the transverse normal stress is given by

$$\boldsymbol{\sigma}^{33} = \lambda \mathrm{G}^{\alpha\beta}\boldsymbol{\epsilon}_{\alpha\beta} + (\lambda + 2\mu)\boldsymbol{\epsilon}_{33}. \tag{3.51}$$

Assuming $\boldsymbol{\sigma}^{33} = 0$, the transverse normal strain is given by

$$\boldsymbol{\epsilon}_{33} = -\frac{\lambda}{\lambda + 2\mu}\mathrm{G}^{\alpha\beta}\boldsymbol{\epsilon}_{\alpha\beta}, \tag{3.52}$$

which is used for static condensation. This results in a modified material law, where λ has to be replaced by $\bar{\lambda}$,

$$\bar{\lambda} = \frac{2\mu\lambda}{\lambda + 2\mu}. \tag{3.53}$$

A shell model which uses the unmodified three-dimensional material law is classified as a three-dimensional shell theory [26]. There is numerical evidence that the lowest order theory which is asymptotically correct is based on the displacement field

$$\mathbf{u}^{3D}(\theta^1,\theta^2,\theta^3) = \overset{(0)}{\mathbf{u}} + \theta^3 \overset{(1)}{\mathbf{u}} + (\theta^3)^2 \overset{(n)}{u}\mathbf{n}, \tag{3.54}$$

depending on $(\overset{(0)}{\mathbf{u}}, \overset{(1)}{\mathbf{u}}, \overset{(n)}{u})$, and involves seven parameters. In the case of plates, the asymptotic correctness was shown in [135, 149]. As an alternative to the parameter $\overset{(n)}{u}$, one can introduce a parameter accounting for a linear variation of the transverse normal strain (see *e.g.* [25]).

Up to now, we have discussed single plate and shell theories focusing on their asymptotic correctness, *i.e.* it is required that the modelling error decreases as the thickness decreases. However, in practice one wants to solve a shell problem with a fixed thickness. In this case, the modelling error is fixed by the chosen model. Following the idea of Cauchy's power series method, one possibility to derive shell models is to introduce an expansion of the displacement field in terms of the thickness coordinate

$$\mathbf{u}(\theta^2,\theta^2,\theta^3) = F_0(\theta^3)\mathbf{v}_0(\theta^1,\theta^2) + F_1(\theta^3)\mathbf{v}_1(\theta^1,\theta^2) + F_2(\theta^3)\mathbf{v}_2(\theta^1,\theta^2) + \ldots. \quad (3.55)$$

The idea of using generalized Fourier expansions with Legendre polynomials as basis functions was introduced by Vekua (see *i.e.* [173]). For a detailed overview, we refer to [183] and references therein. Inserting the expansion (3.55) in the three-dimensional equations and truncation at different orders yield a hierarchy of shell models. In [97], Kienzler derives plate models using an infinite power series expansion. In order to get a finite system of equations, he introduces the uniform approximation method, in which all terms smaller than a given order are neglected. An extension to anisotropic material behavior and a detailed discussion on second order plate theories were given in [98, 158].

The idea of a systematic procedure to decrease the modelling error resulted in hierarchical shell models. According to [3, 16], a hierarchy of models (with solutions u^{M_i} for the i-th model) should fulfill the following criteria:

- Approximability, for a fixed thickness:

$$||u^{3d} - u^{M_i}|| \to 0 \qquad \text{as } i \to \infty, \quad (3.56)$$

- Asymptotic consistency, for a fixed model i:

$$\frac{||u^{3d} - u^{M_i}||}{||u^{3d}||} \to 0 \qquad \text{as } t \to 0, \quad (3.57)$$

- Optimal rate of convergence, in the absence of boundary layers and edge singularities:

$$\frac{||u^{3d} - u^{M_i}||}{||u^{3d}||} \leq C\, t^{\alpha_i} \qquad \text{as } t \to 0,\ i \to \infty \quad (3.58)$$

with a convergence rate $\alpha_{i+1} > \alpha_i$.

The first hierarchical models for shells are given by Vekua. In the case of monolithic plates (the material parameters are constant through the thickness), simple polynomial director functions F_i in (3.55) can be used to fulfill all three criteria. In the case of laminated shells (the material parameters are piecewise constant through the thickness), continuous polynomials cannot fulfill the criterion of optimal convergence rate. We refer to [142] for the mechanics of laminated shells. The mathematical investigation in this field started with the

work of Vogelius [174–176], who considered the scalar Laplace equation. Investigations on elastic plates and shells are given in [16] and [3], see also [56].

A recent review of laminated plate and shell models is given in [36]. Using an expansion like (3.55) for laminated shells, the resulting model is called an equivalent single layer theory. The number of parameters is independent of the number of layers. In order to account for the transverse continuity of the stress, a zig-zag function can be included, see [38]. Another possibility is to use layer-wise theories, which are formed by packages of single-layer shell models coupled at the layer interfaces. In this case, the number of parameters in the model depends on the number of layers. In the next section, we develop a layer-wise theory which accounts for elastic and poroelastic layers.

3.3 Layer-wise poroelastic shell model

In this section, we describe a layer-wise theory for laminated poroelastic shells. Beside early contributions, the analysis of thin poroelastic plate structures starts with [165], where the quasi-static behavior of poroelastic plates is studied. The solid displacement field is restricted to be of Kirchhoff-Love type. In-plane diffusion is neglected, whereas the transverse diffusion is solved with a three-dimensional approach. The dynamic behavior of poroelastic plates by means of a plate model was analyzed in [168]. In [126], poroelastic plate theories for homogeneous plates have been derived utilizing a series expansion in thickness direction. This approach has been extended to layered panels including air layers in [125]. In [160], the extension of the Mindlin plate model to poroelastic plates is proposed. To this end, a quadratic expansion of the pressure through-the-thickness is chosen. A rigorous justification of the poroelastic plate theory given in [165] was published in [117]. The limit model in case of a flexual shell has been derived only recently [120].

In the present thesis, we employ a layer-wise theory. We consider a layup as depicted in Figure 3.2. The total number of layers is L. Each layer has a thickness t_i, $i = 1 \dots L$ and is classified as elastic or poroelastic. The distance from the reference surface to the bottom of the shell is denoted by t_0. Furthermore, we define $T_i = \left[\sum_{j=0}^{i-1} t_j \, , \, \sum_{j=0}^{i} t_j\right]$. The relations between the local thickness coordinate $\tau_i \in [0,1]$ of layer i and the global thickness coordinate $\theta^3 \in T_i$ are

$$\tau_i(\theta^3) = \frac{1}{t_i}\left(\theta^3 - \sum_{j=0}^{i-1} t_j\right), \tag{3.59}$$

and

$$\theta^3(\tau_i) = \sum_{j=0}^{i-1} t_j + t_i\,\tau_i \, . \tag{3.60}$$

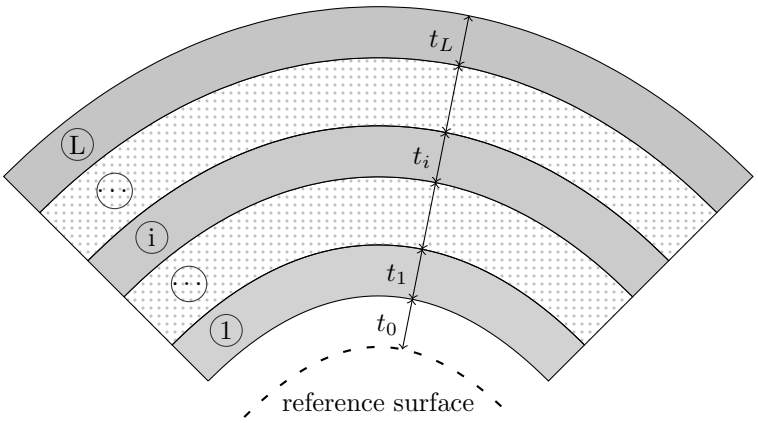

Figure 3.2: Layup of the shell

A layer-wise theory is a semi-discretization of the displacement field. The present layer-wise theory is based on the displacement field given in (3.54). However, instead of monomials, the functions $\overset{(\cdot)}{V}(\tau_\ell(\theta^3))$ are used. The displacement field for layer ℓ is assumed to be of the form

$$\mathbf{u}^\ell(\theta^1,\theta^2,\theta^3) = \overset{(1)}{V}(\tau_\ell(\theta^3))\ \overset{(1,\ell)}{u_i}\ \mathbf{e}^i + \overset{(2)}{V}(\tau_\ell(\theta^3))\ \overset{(2,\ell)}{u_i}\ \mathbf{e}^i + \overset{(n)}{V}(\tau_\ell(\theta^3))\ \overset{(n,\ell)}{u}\ \mathbf{n}. \tag{3.61}$$

The parameters $\overset{(1,\ell)}{u_i} = \overset{(1,\ell)}{u_i}(\theta^1,\theta^2)$ and $\overset{(2,\ell)}{u_i} = \overset{(2,\ell)}{u_i}(\theta^1,\theta^2)$ describe the displacement of the bottom ($\tau = 0$) and the top ($\tau = 1$) of layer ℓ. The displacement field inside the layer is given by the linear functions

$$\begin{aligned} \overset{(1)}{V}(\tau) &= 1-\tau, \\ \overset{(2)}{V}(\tau) &= \tau. \end{aligned} \tag{3.62}$$

This is enhanced with the parameter $\overset{(n,\ell)}{u_i} = \overset{(n,\ell)}{u_i}(\theta^1,\theta^2)$, which accounts for a quadratic variation of the displacement in thickness direction. Thus, we define

$$\overset{(n)}{V}(\tau) = \tau^2 - \tau, \tag{3.63}$$

which vanishes at the bottom and the top surface of the layer. In all possible combinations of elastic and poroelastic layers, the continuity of the displacement field is required. Thus, for two subsequent layers, we set

$$\overset{(2,\ell)}{u_i} = \overset{(1,\ell+1)}{u_i}. \tag{3.64}$$

The total number of parameters is $3(L+1)+L$ and is independent of the stacking sequence. Following [160], the fluid pressure field in poroelastic layers is approximated by

a quadratic expansion. The pressure field for layer ℓ is assumed to be

$$p^{\ell}(\theta^1,\theta^2,\theta^3) = \overset{(1)}{V}(\tau_\ell(\theta^3))\overset{(1,\ell)}{p} + \overset{(2)}{V}(\tau_\ell(\theta^3))\overset{(2,\ell)}{p} + \overset{(n)}{V}(\tau_\ell(\theta^3))\overset{(n,\ell)}{p}, \tag{3.65}$$

where $\overset{(1,\ell)}{p} = \overset{(1,\ell)}{p}(\theta^1,\theta^2)$, $\overset{(2,\ell)}{p} = \overset{(2,\ell)}{p}(\theta^1,\theta^2)$, and $\overset{(n,\ell)}{p} = \overset{(n,\ell)}{p}(\theta^1,\theta^2)$ are three parameters. Between two poroelastic layers, we require the continuity of the pressure. If layer ℓ and $\ell+1$ both are poroelastic, we set

$$\overset{(2,\ell)}{p} = \overset{(1,\ell+1)}{p}. \tag{3.66}$$

The total number of parameters is $3L_p - n_p$, where L_p is the number of poroelastic layers and n_p is the number of interfaces between two poroelastic layers. Since the considered coupling of elastic and poroelastic layers is natural [5], it is sufficient to enforce the continuity of the displacement field and the pressure field, as it is done in (3.64) and (3.66).

4 NUMERICAL SOLUTION METHODS

In this chapter, we will introduce the numerical methods to solve the problems posed in Chapter 2 and 3. These are the Finite Element Method (FEM) and the Method of Fundamental Solutions (MFS). The FEM will be used for the discretization of the layered poroelastic shell problem, whereas the MFS discretizes the acoustic fluid surrounding the shell. We review the basic concepts of both methods. Then we propose a coupled method.

4.1 Finite Element Method

Nowadays, the FEM is one of the most popular numerical methods to find approximate solutions to boundary value problems. A review of the early history of the FEM can be found in [80] among others. In 1909, Walter Ritz proposed a method [146], which is now called the Ritz method. To recall the basic concepts of the Ritz method, we consider the problem

$$\Delta u = 0 \quad \text{in } \Omega, \qquad u = g \quad \text{on } \Gamma. \tag{4.1}$$

It is well known that the solution of (4.1) is a solution of the minimization problem

$$\text{Find } u \in V: \quad J(u) = \inf_{v \in V} J(v), \tag{4.2}$$

where

$$J(v) = \frac{1}{2} \int_{\Omega} \nabla v \cdot \nabla v \, \mathrm{d}x, \tag{4.3}$$

and

$$V = \{u \in H^1(\Omega) |\ u(x) = g(x) \text{ for } x \in \Gamma\} \tag{4.4}$$

is the set of all admissible functions. The idea of the Ritz method is to choose a finite dimensional subset $V_h \subset V$ and seek the solution therein. Therefore, we introduce the function $u_h \in V_h$,

$$u_h(x) = g(x) + \sum_{i=1}^{n} a_i N_i(x), \tag{4.5}$$

where $N_i(x)$ are linearly independent functions satisfying $N_i(x) = 0$ for $x \in \Gamma$. Plugging this function in the functional (4.3), we have

$$J(a_1, a_2, \ldots, a_n) = \frac{1}{2} \int_{\Omega} \nabla u_h \cdot \nabla u_h \, \mathrm{d}x. \tag{4.6}$$

A necessary condition for the minimizer is the stationary condition. Thus, we require

$$\frac{\partial J}{\partial a_1} = 0, \quad \dots \quad \frac{\partial J}{\partial a_i} = 0, \quad \dots \quad \frac{\partial J}{\partial a_n} = 0. \tag{4.7}$$

This yields the system of linear equations,

$$Ku = f, \tag{4.8}$$

where

$$\begin{aligned} K[i,j] &= \int_\Omega \nabla N_i \cdot \nabla N_j \, \mathrm{d}x, \\ u[i] &= a_i, \\ f[i] &= -\int_\Omega g \, N_i \, \mathrm{d}x. \end{aligned} \tag{4.9}$$

The solution of (4.8) yields the unknown coefficients a_i. Then the approximate solution is given by (4.5).

Referring to [80], one drawback of the Ritz method is that it only applies to minimization problems. This was resolved, when Bubnov introduced the procedure to obtain the weak form starting form the differential equation, which leads to the same results as the Ritz method. This has already been applied in this thesis in Sections 2.3 and 2.4. Beside many applications, a main contribution of Galerkin is to realize that one does not even need a minimization principle for the procedure of Bubnov.

A crucial point in the Ritz method is the choice of basis functions $N_i(x)$. Ritz used polynomials and the eigenfunctions of a clamped rod as basis functions. Bubnov and Galerkin also used trigonometric functions. These choices are global functions in the sense that they are non-vanishing almost in the whole problem domain. This yields fully populated matrices K in (4.8). In 1943, Courant [55] used piece-wise polynomials, which are called hat functions today. This choice has the distinctive advantage that the resulting matrix K becomes sparse. As these piece-wise polynomials are defined with respect to elements, the term Finite Element Method is used. The element concept gives also great flexibility in handling complex domains. The first formal definition of a finite element was given by Ciarlet [45]. To summarize, the classical version of the FEM is based on the following principles:

- The domain Ω is covered by a mesh $\mathcal{T}_h$, which is a collection of elements.
- The space V_h consists of low order piece-wise polynomials.
- The basis $\{N_i\}$ of V_h has local supports. Each basis function N_i is non-zero only on a few neighboring elements.

Due to its efficiency and flexibility, the literature on the FEM is vast. We mention the books of Strang and Fix [163], Jung and Langer [94], Braess [31], Brenner and Scott [32], Steinbach [162], and Zienkiewicz *et al.* [185] among many others.

FEM for surface problems. The poroelastic shell problem treated in this thesis is governed by a two-dimensional problem posed on the reference surface, which is embedded in the three-dimensional ambient space. Beside shell problems, it is of interest to solve other partial differential equations on surfaces. A review of finite elements for surface problems is given in [66].

Following the classical FEM approach, the first step is to construct a surface mesh. To this end, different algorithms have been developed, depending on the description of the surface (*e.g.* parametric description [14], implicit description [57], description by data from measurements [108]). This step turns the original surface description into a discrete piecewise parametric description. With the focus on implicitly represented geometry, the work of Dziuk [65] plays an important role. Therein, the convergence of a FEM based on linear triangles is proved. To this end, the so-called lift operator was introduced. It establishes a relation between functions on the discrete surface $\bar{\Omega}_h$ and the continuous smooth surface $\bar{\Omega}$. To this end, a point x in a strip $U_{\bar{\Omega}}$ around $\bar{\Omega}$ is mapped onto $\bar{\Omega}$ by means of

$$\begin{aligned} a : U_{\bar{\Omega}} &\to \bar{\Omega} \\ x &\mapsto a(x) = x - d(x)\nu(x). \end{aligned} \tag{4.10}$$

Here, $d(x)$ is the oriented distance function and $\nu(x) = \nabla d(x)$ is the normal vector to $\bar{\Omega}$ at $a(x)$. The method in [65] has been extended to an arbitrary high order in [61]. To achieve a high order method, both the geometry and the field approximation have to be of higher order. To achieve a high order geometry description, typically Lagrange shape functions are used. Their geometric nodes are arranged such that the surface is represented accurately. Nevertheless, the mapping (4.10) is difficult to realize in situations where the signed distance function is not given explicitly. Therefore, one resorts to a mapping of the type

$$\begin{aligned} a : U_{\bar{\Omega}} &\to \bar{\Omega} \\ x &\mapsto a(x) = x + r(x)\, s(x), \end{aligned} \tag{4.11}$$

where $r(x)$ is the distance to the surface with respect to the predefined search direction $s(x)$. The mesh transformation can be obtained by nodal interpolation [77, 78] or by projection [106]. We remark that in [77] and [106], an interface problem is treated. Nevertheless, a method for surface problems based on the exact geometry, thus eliminating the geometric error, is described in [61]. This method builds the basis of our method proposed in Section 4.1.3. We remark that in practical examples, the surface is not necessarily smooth. In [77], multiple level-set functions for the domain description are considered, introducing corners

in the surface. It remains an open question to what extent our method described in Section 4.1.3 is applicable in such situations.

Another type of method for solving surface problems are the Eularian methods [34], where the need of a triangulation of the surface is bypassed. To this end, the problem is extended to the ambient space. Then, this three-dimensional problem can be solved using the standard FEM. We refer to [66] for an overview of such bulk FEMs.

FEM for shell problems. In this paragraph, a literature review of finite element approaches for elastic shells is given. Due to the vast amount of literature available on the topic, an overall review cannot be provided. We broadly classify the finite elements for shells into four categories [136]:

- facet-shell elements,
- 3-D elements,
- continuum element,
- shell elements based on a shell theory.

The facet-shell elements were the first finite elements for the numerical analysis of shells. The shell geometry is approximated by flat elements with plate-like membrane and bending behavior. Due to the missing coupling between bending and stretching, these elements cannot provide reliable performance in general.

The most general approach is the use of standard 3D elements. Therein, the three-dimensional shell volume is represented by three-dimensional elements. However, using only linear shape functions, the aspect ratio of the elements is limited. This leads to prohibitively high computational costs. Even worse, using only one linear element through the thickness leads to wrong results, even in the thin limit. Good results can be obtained, if we use quadratic shape functions in thickness direction, which is in agreement with the kinematics in (3.54). Using a high order ansatz in the in-plane directions, the requirements on the aspect ratio of the elements can be reduced [64, 140]. An automatic hp FEM for thin-walled structures is given in [167]. Motivated by the observation that in most CAD software, the geometry is described by NURBS, Hughes introduced the concept of Isogeometric Analysis [90]. The main idea therein is to use the NURBS functions from the geometry model also for the approximation of the field variables. This high order isoparametric method using exact geometry was used in [90] for the solution of shell problems given by a three-dimensional description.

The continuum elements or degenerated elements are motivated by the finite element analysis. The first degenerated element was proposed by Ahmad, Irons and Zienkiewicz [4]. The mid-surface of the shell is approximated by elements. Then, the three-dimensional shell volume is approximated by the interpolation of the normal vector using the standard

basis functions. Finally, appropriate assumptions are imposed on the displacement field. This typically leads to a Reissner-Mindlin type kinematic. Although having different starting points, continuum elements and elements based on a shell theory coincide, in case the same assumptions are posed [33].

A shell theory is formulated on the exact geometry of the shell, which is given by means of a parametrization of the reference surface. The kinematic assumptions are formulated with reference to the exact geometry, leading to a formulation of the problem where the unknown fields live on the reference surface only. In particular, the sought field variables depend on the parametric coordinates and are determined by a problem with non-constant coefficients. In fact, the quantities from differential geometry become coefficients. The two most common shell models are the Koiter model (shear rigid) and the Naghdi model (shear deformable). Both encounter their difficulties when it comes to the finite element discretization. In the case of the Koiter model, the solution lies in H^2. Thus, a conforming discretization requires advanced concepts. In the special case of rectangular elements, the Bogner-Fox-Schmit element [27] is applicable, which is based on Hermite basis functions. A famous triangular element, which can be used in an arbitrary planar triangulation, is the Argyris element [12]. We refer to [132] for a discussion of further plate elements. An interesting approach extending the concept of subdivision surfaces to the discretization was given in [51]. Recently, the conforming discretization on unstructured quadrilateral meshes has been presented in [115]. Furthermore, in the case of curved structures, an insufficient approximation of the space of inextensional displacements leads to membrane locking. In the case of the Naghdi model, a discretization of H^1 functions is required. One of the main problems here is shear locking. In order to resolve the locking issues, many finite elements based on mixed approaches have been proposed. Common techniques are reduced integration, assumed natural strain, enhanced assumed strain, and discrete strain gap [40, 104, 184]. A locking-free method based on an advanced mathematical variational formulation is the TD-NNS method [139]. At the price of H^2 conforming elements, a shear-locking free method based on a pure displacement formulation is possible [68, 111, 131]. Another problem arises in case of large rotations. Then, the discretization of the non-linear configuration space is required, see [154] for this issue.

To our best knowledge, the first FEM for shells based on the exact geometry given by NURBS is due to Cho and Roh in [43]. They discretize the field variables arising from a shear deformable shell theory in the parameter domain with linear and quadratic elements. To tackle the locking issue, the assumed strain technique is deployed. The work of Arciniega and Reddy [10, 11] generalizes the exact geometry to arbitrary parametrizations. They apply their high order FEM based on Lagrange elements to a seven-parameter shell theory considering geometrical nonlinearities and functionally graded shells. However, the actual computation of the arising integrals is carried out by symbolic algebra subroutines written in MAPLE. Following the concept of Isogemetric Analysis, shell finite elements based on different shell models were proposed in [19, 88, 89, 96] among others. Therein, the reference surface is described by NURBS, just as the field approximation.

4.1.1 Basic concepts

The first step to obtain a finite element discretization is a geometric partitioning of the problem domain Ω with a mesh $\mathcal{T}_h$. In many situations, the mesh is only an approximation

$$\Omega \approx \mathcal{T}_h = \bigcup_{e=1}^{N} \tau_e, \tag{4.12}$$

which is the union of geometric elements τ_e. For the later construction of shape functions, the concept of the reference element is crucial. Typically, reference elements of simple shape are used. In the case of three-dimensional problems, tetrahedra and hexahedra are common, whereas in that of two-dimensional problems triangles and quadrilaterals dominate. In the rest of the present thesis, we treat triangles and quadrilaterals only. We assume that the geometric element is given as the image of a map $\Phi^e : \tau^R \mapsto \tau_e$ with the reference element τ^R as domain. Usually, this mapping is written in the form

$$\mathbf{x} \in \tau_e : \quad \mathbf{x}(\xi,\eta) = \sum_{i=1}^{N} \varphi_i(\xi,\eta)\, \mathbf{x}_i^e. \tag{4.13}$$

Here, the functions φ_i are the bi-variant Lagrange polynomials defined with respect to the N nodes on the reference element. $\mathbf{x}_i^e$ are the coordinates of the nodes in the real space. We restrict our presentation to the lowest order case only. Extensions to higher order mapping functions and the blending function technique can be found in [164]. In the case of the reference triangle illustrated in Figure 4.1, we have $N = 3$ and the functions

$$\begin{aligned} \varphi_1 &= 1 - \xi - \eta, \\ \varphi_2 &= \xi, \\ \varphi_3 &= \eta, \end{aligned} \tag{4.14}$$

are related to the nodes $(0,0)$, $(1,0)$, and $(0,1)$. In the case of the reference quadrilateral

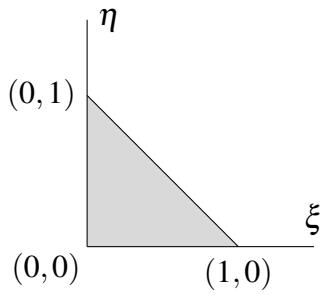

Figure 4.1: Reference triangle

depicted in Figure 4.2, we have $N = 4$ and the functions

$$\begin{aligned} \varphi_1 &= 1 - \xi - \eta + \xi\eta, \\ \varphi_2 &= \xi\,(1-\eta), \\ \varphi_3 &= \eta\,(1-\xi), \\ \varphi_4 &= \xi\,\eta, \end{aligned} \tag{4.15}$$

are related to the nodes $(0,0)$, $(1,0)$, $(0,1)$, and $(1,1)$.

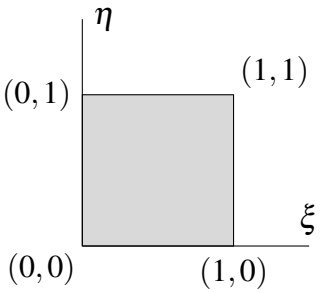

Figure 4.2: Reference quadrilateral

Shape functions. In a next step, we define the element shape functions, which will later form the basis of V_h. In contrast to the classical version of the FEM, where only low order polynomials are used, we construct high order hierarchical shape functions. Following [164], hierarchical shape functions have been first introduced by Peano [137, 138]. We follow the presentation of Zaglmayr [182], where a general approach for the construction of shape functions with special continuity requirements is given. In view of the problems introduced in Chapter 2, we consider H^1-conforming shape functions. In order to construct the shape functions, we introduce the Legendre polynomials, which are defined by the three-term recurrence relation

$$(n+1)\ell_{n+1}(x) = (2n+1)\ell_n(x) - n\,\ell_{n-1}(x) \quad \text{for} \quad n \geq 1, \tag{4.16}$$

and

$$\begin{aligned} \ell_0(x) &= 1, \\ \ell_1(x) &= x. \end{aligned} \tag{4.17}$$

The set $(\ell_i)_{0\leq i\leq p}$ spans the full space of polynomials up to order p on the interval $(-1,1)$. Furthermore, they satisfy the orthogonality relation

$$\int_{-1}^{1} \ell_i(x)\,\ell_j(x)\,\mathrm{d}x = \frac{2}{2i+1}\delta_{ij} \tag{4.18}$$

Furthermore, we introduce the integrated Legendre polynomials

$$L_n(x) = \int_{-1}^{x} \ell_{n-1}(y)\,\mathrm{d}y, \qquad n \geq 2. \tag{4.19}$$

For the construction of the shape functions on the triangle, we introduce the scaled integrated Legendre polynomials

$$L_n^S(x,t) = t^n L_n\left(\frac{x}{t}\right). \tag{4.20}$$

With the polynomials defined above, we construct a Vertex-Edge-Cell-based space on the reference quadrilateral and the reference triangle. We use a uniform polynomial order p. The vertex-based shape functions are

$$\phi_i^V(\xi,\eta) = \varphi_i(\xi,\eta), \qquad \text{for } i = 1,\ldots,N. \tag{4.21}$$

The functions φ_i are given in (4.14) for the triangle and in (4.15) for the quadrilateral. The $4(p-1)$ edge-based shape functions on the quadrilateral are

$$\begin{aligned}
\phi_i^{E_1} &= L_{i+1}(1-2\xi)(1-\eta),\\
\phi_i^{E_2} &= L_{i+1}(1-2\eta)\,\xi,\\
\phi_i^{E_3} &= L_{i+1}(1-2\xi)\,\eta,\\
\phi_i^{E_4} &= L_{i+1}(1-2\eta)(1-\xi), \qquad \text{for } i = 1,\ldots,p-1.
\end{aligned} \tag{4.22}$$

The $(p-1)^2$ cell based shape functions on the quadrilateral are

$$\phi_{ij}^C = L_{i+1}(1-2\xi)L_{j+1}(1-2\eta), \qquad \text{for } i,j = 1,\ldots,p-1. \tag{4.23}$$

In the case of the triangle, for $p \geq 2$, the $3(p-1)$ edge based shape functions are

$$\begin{aligned}
\phi_i^{E_1} &= L_{i+1}^S(2\xi+\eta-1, 1-\eta),\\
\phi_i^{E_2} &= L_{i+1}^S(\eta-\xi, \eta+\xi),\\
\phi_i^{E_3} &= L_{i+1}^S(1-\xi-2\eta, 1-\xi), \qquad \text{for } i = 1,\ldots,p-1.
\end{aligned} \tag{4.24}$$

Given $p \geq 3$, the $\frac{(p-2)(p-1)}{2}$ cell-based shape functions on the triangle are

$$\phi_{ij}^C = L_{i+2}^S(2\xi+\eta-1, 1-\eta)\;\eta\;\ell_j(2\eta-1), \qquad \text{for } 1 \leq i+j \leq p-3. \tag{4.25}$$

Up to this point, we have constructed element shape functions on the reference element. By means of (4.13), we can map the element functions to the real space. The goal is now to construct a global basis $\{N_i(\mathbf{x})\}$ for V_h. Therefore, we have to piece together the shape functions defined on the elements. This is achieved by establishing a connection between the local degrees of freedom and the global ones. Details on the basic assembling process can be found *e.g.* in the textbook [94]. Solutions for the orientation problem in the high-order case are described in [182].

Dirichlet boundary conditions. In the Ritz method, the basis functions are chosen such that they fulfill the Dirichlet boundary conditions exactly. Given the element concept of the FEM, the Dirichlet boundary conditions are only fulfilled approximately. In view of (4.5), we decompose the set of basis functions according to $\{\phi_i\} = \{\phi_{i,I}\} \cup \{\phi_{i,D}\}$, where $\{\phi_{i,D}\}$ is the set of basis functions with support on the Dirichlet boundary Γ_D and $\{\phi_{i,I}\} = \{\phi_i\} \cap \{\phi_{i,D}\}$. Considering a scalar problem with Dirichlet boundary $\Gamma_D \subseteq \Gamma$, the approximation reads

$$u_h(\mathbf{x}) = \sum_{i \in \Upsilon_D} g_i N_i(\mathbf{x}) + \sum_{i \in \Upsilon_I} a_i N_i(\mathbf{x}), \tag{4.26}$$

where Υ_D is the index set of basis functions with support on the Dirichlet boundary Γ_D and $\Upsilon_I = \Upsilon \setminus \Upsilon_D$. The coefficients g_i are computed by means of projection. To this end, we minimize the error in the Dirichlet datum

$$||g - u_h||^2_{L_2(\Gamma_D)} = \int_{\Gamma_D} (g - u_h)^2 \, \mathrm{d}s. \tag{4.27}$$

This leads to the linear system of equations

$$M_\Gamma \, u_\Gamma = f_\Gamma \tag{4.28}$$

where

$$\begin{aligned} M_\Gamma[i,j] &= \int_{\Gamma_D} \phi_i(x)\phi_j(x) \, \mathrm{d}s, \\ u_\Gamma[i] &= g_i, \\ f_\Gamma[i] &= \int_{\Gamma_D} \phi_i(x) g(x) \, \mathrm{d}s. \end{aligned} \tag{4.29}$$

4.1.2 A FEM for parametric shells

The goal of this section is to present the FEM based on the layer-wise theory given in Section 3.3, if the reference surface is given parametrically. The case of an implicitly given reference surface is treated in Section 4.1.3. In the present thesis, the shell analysis is based on the following principles:

- The three-dimensional shell is given through a reference surface and thickness information. The reference surface is given either parametrically or implicitly. In both cases, the exact geometry is used in the simulation.
- The dependency of the field variables on the thickness coordinate is resolved with a semi-discretization using a layer-wise model based on a 7-parameter model extended to poroelasticity, introduced in Section 3.3.

- The field variables are sought with respect to the curvilinear coordinates induced by the parametrization. The coefficients in the governing equations depend on the material parameters and on quantities from differential geometry. This requires the derivatives of the parametrization up to the second order. Although these derivatives are evaluated numerically, they are computed with double precision using the hyper-dual number concept introduced in [72]. Thus, the derivatives do not alter the overall accuracy.
- The discretization of the field variables is done using high order hierarchical shape functions.
- The solution is obtained by solving the respective three-dimensional equations of elasticity and poroelasticity. We use a tensor product quadrature rule based on one-dimensional Gauss-Legendre rules. No approximation of the integrands is introduced. Apart from using high order shape functions, no method to avoid locking has been considered.
- All possible coupling combinations between elastic and poroelastic layers are natural [5]. Thus, only the continuity of the displacement field and the fluid pressure field have to be considered. This is accomplished in the standard assembling process.

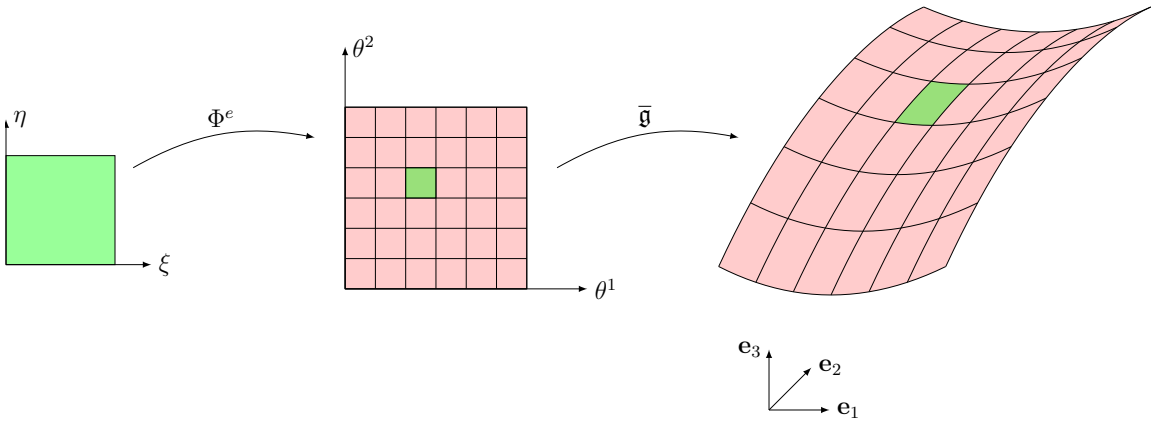

Figure 4.3: Geometry mappings for parametrically given shells

We distinguish between two variants of the way how the reference surface is given. In this section, we treat the case where the reference surface is given by a global parametrization $\overline{\mathfrak{g}}$. The situation is depicted in Figure 4.3. Instead of mapping the reference element to the real space, it is mapped to the parameter space. For this we adopt the standard geometry mapping (4.13). From the parameter space it is mapped to the real space by means of $\overline{\mathfrak{g}}$. The computation of the system matrix requires the knowledge of the quantities from differential geometry given in Section 3.1. The main difficulty here is the evaluation of the derivatives of the parametrization $\overline{\mathfrak{g}}$ up to the second order. To accomplish this task, different strategies are possible. One possibility is to use symbolic differentiation. This

has the drawback of leading to inefficient codes. A second possibility is to use numerical differentiation based on finite differences. However, it is well known that this approach leads to inaccurate results due to round off and subtractive cancellation errors. In the present work we use an automatic differentiation schema based on an augmented algebra. In particular, we use the hyper-dual number concept developed in [72]. To this end, a hyper-dual number class has been implemented providing operator overloading.

The sought field variables are in H^1. Therefore, the two-dimensional high order basis functions introduced in Section 4.1.1 are applicable. We discretize each parameter introduced in the shell model by means of (4.26). Within this setting, the remaining difficulty lies in the evaluation of the integrals given in (2.43) and (2.78) . Here, we only work out the detailed expression for the elastic stiffness matrix K_u. In view of (3.44), we have

$$\begin{aligned} K_u(\mathbf{u}_h, \bar{\mathbf{u}}_h) = \sum_{l=1}^{N_L} \int\limits_{\bar{U}\times T_l} \Big(& \mathbb{C}^{\alpha\beta\gamma\varphi} \tilde{\epsilon}_{\alpha\beta} \hat{\epsilon}_{\gamma\varphi} + \lambda \mathrm{G}^{\alpha\beta} \left(\tilde{\epsilon}_{\alpha\beta} \hat{\epsilon}_{33} + \tilde{\epsilon}_{33} \hat{\epsilon}_{\alpha\beta} \right) + \\ & 4\mu \mathrm{G}^{\alpha\beta} \tilde{\epsilon}_{\alpha 3} \hat{\epsilon}_{\beta 3} + (\lambda + 2\mu) \tilde{\epsilon}_{33} \hat{\epsilon}_{33} \Big) \sqrt{\langle \mathrm{G}_{\alpha\beta} \rangle} \, \mathrm{d}\theta, \end{aligned} \tag{4.30}$$

where $\tilde{\epsilon}_{ij} = \epsilon_{ij}(\mathbf{u}_h)$ and $\hat{\epsilon}_{ij} = \epsilon_{ij}(\bar{\mathbf{u}}_h)$. In view of the layer kinematics given in (3.61), the components of the strain tensor for every layer are

$$\begin{aligned} \epsilon_{\alpha\beta} &= \frac{1}{2} \left(\mu_\alpha^\varsigma \bar{J}_\varsigma^i \left(\overset{(1)}{V} \overset{(1)}{u}_{i,\beta} + \overset{(2)}{V} \overset{(2)}{u}_{i,\beta} \right) + \mu_\beta^\varsigma \bar{J}_\varsigma^i \left(\overset{(1)}{V} \overset{(1)}{u}_{i,\alpha} + \overset{(2)}{V} \overset{(2)}{u}_{i,\alpha} \right) \right) - \mu_\alpha^\varsigma h_{\varsigma\beta} \overset{(n)}{V} \overset{(n)}{u}, \\ \epsilon_{\alpha 3} &= \frac{1}{2} \left(\mu_\alpha^\varsigma \bar{J}_\varsigma^i \left(\overset{(1)}{V}_{,3} \overset{(1)}{u}_i + \overset{(2)}{V}_{,3} \overset{(2)}{u}_i \right) + \bar{J}_3^i \left(\overset{(1)}{V} \overset{(1)}{u}_{i,\alpha} + \overset{(2)}{V} \overset{(2)}{u}_{i,\alpha} \right) + \overset{(n)}{V} \overset{(n)}{u}_{,\alpha} \right), \\ \epsilon_{33} &= \bar{J}_3^i \left(\overset{(1)}{V}_{,3} \overset{(1)}{u}_i + \overset{(2)}{V}_{,3} \overset{(2)}{u}_i \right) + \overset{(3)}{V}_{,3} \overset{(3)}{u}_3. \end{aligned} \tag{4.31}$$

The superscript l has been dropped for the sake of easier readability. The contravariant components of the metric tensor are computed by (3.25), without simplifications. We use the tensor product of one-dimensional Gauss-Legendre rules, where we distinguish between the in-plane directions and the thickness direction. For the in-plane direction we take at least $p+1$ quadrature points, whereas for the thickness direction three quadrature points are taken. All other arising integrals are computed in a similar fashion. All necessary ingredients can be found in Section 3.1. Special care has to be taken of singular parametrizations, where the determinant of the metric vanishes on some part.

Singular parametrizations. We propose a strategy to deal with singular parametrizations of smooth surfaces. In particular, we focus on the case, where one side of the boundary is mapped to a single point in the real space. In this case, the stiffness matrix does

not need to exist. We modify the ansatz space by combining and skipping basis functions. In the framework of Isogeometric Analysis, a similar strategy was considered in [166]. Related studies on the interpolation properties in the case of the standard FEM, when quadrilaterals degenerate to triangles are [2,91].

For presentational purposes, we assume that the boundary at the line $\theta^1 = 0$ in the parameter space is mapped to a single point P_0 in the real space. Therefore, we can write

$$\overline{\mathfrak{g}}(0, \theta^2) = P_0. \tag{4.32}$$

Obviously,

$$\overline{\mathbf{G}}_2 = \mathbf{0} \quad \text{for } \theta^1 = 0, \tag{4.33}$$

and the determinant of the metric is zero at the whole line $\theta^1 = 0$. We assume that apart from the line $\theta^1 = 0$ the parametrization is regular. Furthermore, it is assumed that $\mathrm{G}_{11} > 0$ and that the Laurent expansion of $\mathrm{G}^{22}\sqrt{\langle \mathrm{G}_{\alpha\beta} \rangle}$ about $\theta^1 = 0$ is of the form

$$\mathrm{G}^{22}\sqrt{\langle \mathrm{G}_{\alpha\beta} \rangle} = \frac{a_{-1}(\theta^2)}{\theta^1} + \sum_{i=0}^{\infty} (\theta^1)^i a_i(\theta^2). \tag{4.34}$$

Investigation of the existence of

$$\int_{\bar{\Omega}} \nabla u_h \cdot \nabla v_h \, \mathrm{d}\mathbf{x} = \int_{\bar{U}} (u_{h,1} v_{h,1} G^{11} + (u_{h,1} v_{h,2} + u_{h,2} v_{h,1}) G^{12} + u_{h,2} v_{h,2} G^{22}) \sqrt{\langle \mathrm{G}_{\alpha\beta} \rangle} \, \mathrm{d}\theta \tag{4.35}$$

leads to the following modifications of the shape functions:

1. All vertex-based shape functions on $\theta^1 = 0$ are added up to one single shape function.
2. All edge-based shape functions on $\theta^1 = 0$ are removed, *i.e.* the respective degrees of freedom are constrained to zero in the implementation.
3. No modification of the cell-based shape functions is made.

The problematic term is

$$u_{h,2} v_{h,2} \, G^{22} \sqrt{\langle \mathrm{G}_{\alpha\beta} \rangle} = u_{h,2} v_{h,2} \frac{a_{-1}(\theta^2)}{\theta^1} + \text{higher order terms}. \tag{4.36}$$

We remark that u_h and v_h are polynomials. The integral exists in the case of $u_{h,2} = 0$, *i.e.* u_h is constant with respect to θ^2 or $u_h = 0$ on $\theta^1 = 0$. Writing

$$u_{h,2} = \sum_{i=0}^{p} \sum_{j=0}^{p} a_{ij} \, (\theta^1)^i \, (\theta^2)^j, \tag{4.37}$$

the integral does not exist if any $a_{0j} \neq 0$. The non-vanishing functions on $\theta^1 = 0$ are related to the nodes and edges there. All cell-based shape functions vanish on the boundary. A function u_h which is constant with respect to θ^2 can be constructed summing all node-based functions up. This gives one new shape function. The edge-based shape functions are of higher order with respect to θ^2 on $\theta^1 = 0$. Thus, they are eliminated.

As indicated by the numerical results given in Chapter 5, this approach seems to be feasible for all integrals arising in this thesis in the case of the considered singularities.

4.1.3 A FEM for implicitly given shells

In the previous section, we assumed that the reference surface of the shell is given by a global parametrization $\bar{\mathfrak{g}}$, which is given as an input. In this section, we want to treat the case where the reference surface is given implicitly as the zero level of a given level set function. In order to utilize the finite element concept, we turn this implicit description into a parametric one.

In this section, the reference surface is given as follows. Let $B \subseteq \mathbb{R}^3$ be a given rectangular cuboid and $\phi : B \to \mathbb{R}$ a given level-set function. Then the implicit reference surface $\bar{\Omega} \subset B$ is given as the zero level-set,

$$\bar{\Omega} = \{\mathbf{x} \in B |\ \phi(\mathbf{x}) = 0\}. \tag{4.38}$$

In order to apply the FEM, we parametrize the reference surface using triangles. To this end, we first use the Marching Cubes Algorithm [112] to obtain a triangulation $\bar{\Omega}_h$ of the reference surface. This triangulation represents a linear approximation of the surface. We require that the approximation is sufficiently accurate such that the following steps are well defined. However, it is not necessary that any vertex lies on $\bar{\Omega}$.

Now, the goal is to lift $\bar{\Omega}_h$ onto $\bar{\Omega}$ such that $a(\bar{\Omega}_h) = \bar{\Omega}$. Using the mapping based on the closest point projection defined in (4.10) is not suitable in the considered setting. This is illustrated in Figure 4.4. The level-set function defines a sphere in $\mathbb{R}^3$. However, only a part of the sphere lies in the considered B. The black triangle is mapped to the blue surface $a(\bar{\Omega}_h)$. The red surface is the difference between $\bar{\Omega}$ and $a(\bar{\Omega}_h)$. Thus, $a(\bar{\Omega}_h) \neq \bar{\Omega}$. In order to overcome this issue, we use (4.11)

$$\begin{aligned} \bar{\mathfrak{g}} : U_{\bar{\Omega}} &\to \bar{\Omega} \\ \mathbf{x} &\mapsto a(\mathbf{x}) = \mathbf{x} + r(\mathbf{x})\, s(\mathbf{x}). \end{aligned} \tag{4.39}$$

For the unique definition, we need to specify the search directions $s(x)$. Let V denote the set of all vertices of $\bar{\Omega}_h$. We set

$$\tilde{s}_v(\mathbf{x}) = \frac{\nabla\phi(\mathbf{x})}{||\nabla\phi(\mathbf{x})||} \quad \text{for } \mathbf{x} \in V. \tag{4.40}$$

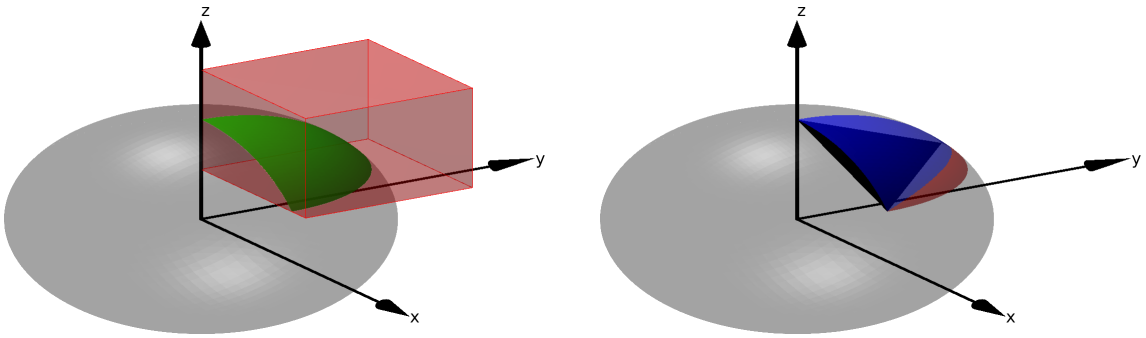

Figure 4.4: Limitations of the closest point projection lift

To preserve the exact geometry, we apply a modification at the vertices on the boundary of B. Thus, we set

$$s_v(\mathbf{x}) = \begin{cases} \tilde{s}_v(\mathbf{x}) - (\tilde{s}_v(\mathbf{x}) \cdot \mathbf{n}_{\partial B}(\mathbf{x}))\, \mathbf{n}_{\partial B}(\mathbf{x}) & \text{for } \mathbf{x} \in V \cap \partial B \\ \tilde{s}_v(\mathbf{x}) & \text{else} \end{cases}. \tag{4.41}$$

Then the search direction field $s(\mathbf{x})$ defined on $\bar{\Omega}_h$ is obtained by linear interpolation of $s_v(\mathbf{x})$. The mapping is numerically realized by means of the Newton iteration

$$\mathbf{x}^{k+1} = \mathbf{x}^k - s(\mathbf{x}^k)\, \frac{\phi(\mathbf{x}^k)}{\nabla\phi(\mathbf{x}^i) \cdot s(\mathbf{x}^k)}. \tag{4.42}$$

Thus, every point in the reference element can be mapped onto the exact geometry, which reassembles the situation of Section 4.1.2 where $\bar{\mathfrak{g}}$ was given as input directly. However, the evaluation of the parametrization requires the solution of a non-linear root finding problem. Thus, the use of symbolic differentiation becomes difficult. Nevertheless, the hyper-dual number concept is not affected by this issue.

Although the exact geometry is available, it is of interest to refine the mesh in order to achieve a better approximation of the sought field variables. In the case of an approximated geometry, the mesh has to be perturbed after each refinement. In the simplest approach, the newly created nodes have to be projected onto the continuous surface $\bar{\Omega}$. However, in an exact geometry setting, no perturbation of the mesh is necessary. We end this section with a study where we compare the lifted mesh and the non-lifted mesh. To this end, we compute the error in the area for a part of a hyperboloid given as $\phi = z^2 - 1 - x^2 - y^2$ and $B = [0,2] \times [0,2] \times [0.5, 1.5]$. We distinguish between four refinement procedures.

(a) Fixed mesh: h-type refinement without perturbation, the search directions are interpolated.

(b) Lifted mesh: h-type refinement with perturbation, the search directions are interpolated.

(c) Updated search directions: h-type refinement with perturbation, the search directions are recomputed after each refinement.

(d) One element: p-type refinement, the number of quadrature points on the single element is increased successively.

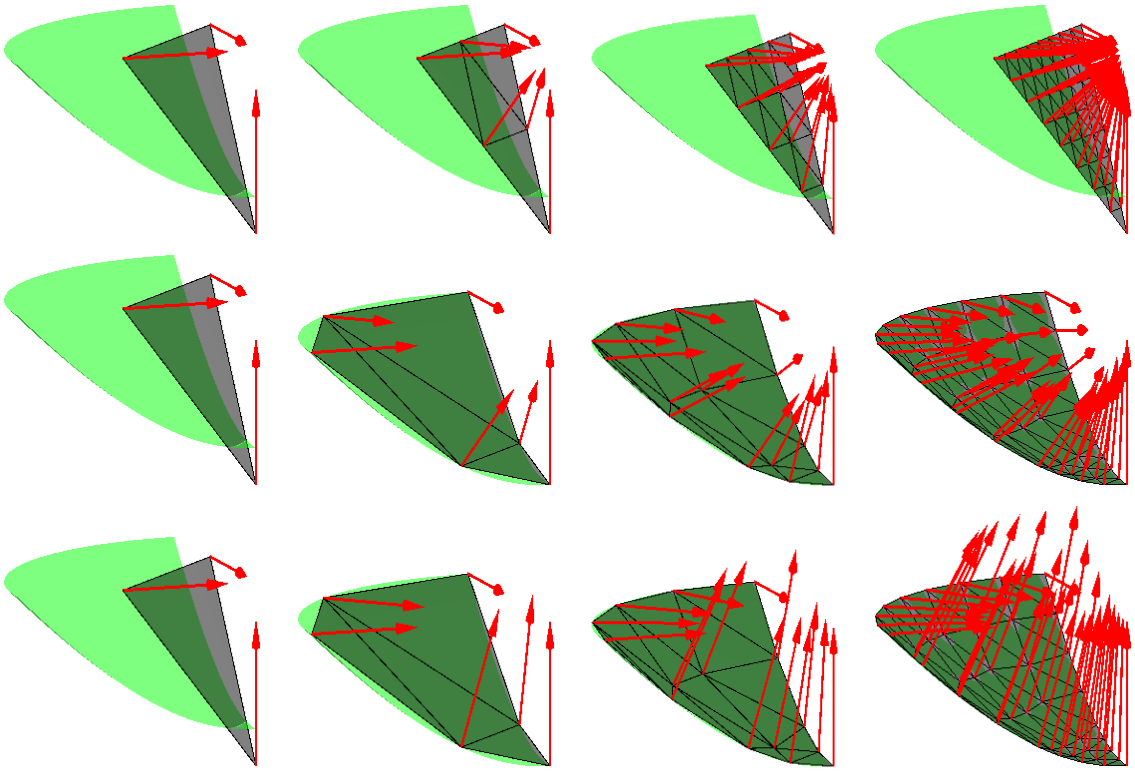

Figure 4.5: Refinement without (upper row) and with (lower row) lifting the vertices, the red arrows indicate the search directions

In all h-type refinements we use four quadrature points per element. The first four levels are depicted in Figure 4.5 for these refinement procedures. The results are illustrated in Figure 4.6. The refinement schemes (a) and (b) yield the same optimal asymptotic convergence rate. Interestingly, scheme (a) has a better constant in this example. However, scheme (c) gives a sub-optimal quadratic rate, whereas (d) yields an exponential convergence rate, as it is expected for a p-type refinement.

4.2 Method of Fundamental Solutions

In this section, we will introduce a variant of the Method of Fundamental Solutions (MFS), which is a Trefftz-type method. This method is used to discretize the acoustic fluid sur-

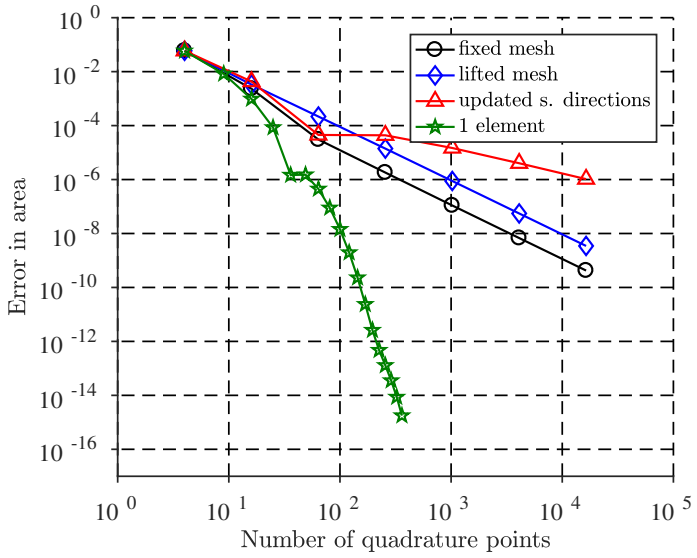

Figure 4.6: Convergence results for the error in area

rounding the shell structure. In general, a Trefftz method consists of a discrete Trefftz space and a Trefftz variational formulation. Apart from exceptions, any discrete space can be used with any variational formulation.

In 1926, an alternative numerical method to the Ritz method was proposed by Trefftz [170]. The main difference between these methods is the way how the solution space is approximated. Instead of choosing an ansatz which fulfills the Dirichlet boundary conditions exactly, an ansatz fulfilling the partial differential equations was suggested. Therefore, we search for an approximate solution in the form of

$$v_h(x) = \sum_{i=1}^{N_s} c_i \, p_i(x), \tag{4.43}$$

where c_i are the coefficients which have to be determined and p_i are functions fulfilling the governing partial differential equation in the domain. Considering the problem given in (4.1), the p_i are potential functions. The ansatz (4.43) can be used with respect to elements in a mesh or to the whole problem domain. Here, we adopt the latter use leading to a single-element Trefftz method [85]. For the particular functions, different choices are possible. In the recent survey [85], generalized harmonic polynomials, plane waves, evanescent waves, fundamental solutions and multipol expansions are mentioned as the most used ansatz functions among others. In the present work we use fundamental solutions of the Helmholtz equation.

Once the set of approximating functions is chosen, the task is to determine the coefficients

c_i in (4.43). In [170], the unknown coefficients are determined by the minimization of

$$F(v_h) = \int_\Omega \nabla(p - v_h) \cdot \nabla(p - v_h) \, \mathrm{d}\mathbf{x}, \tag{4.44}$$

where p is the exact solution. This yields the system of linear equations,

$$Ku = f, \tag{4.45}$$

where

$$\begin{aligned} K[i,j] &= \int_\Gamma p_i \, \nabla p_j \cdot \mathbf{n} \; \mathrm{d}s_\mathbf{x}, \\ u[i] &= c_i, \\ f[i] &= -\int_\Gamma g \, \nabla p_i \cdot \mathbf{n} \; \mathrm{d}s_\mathbf{x}. \end{aligned} \tag{4.46}$$

In [101], a classification of different formulations for the single-element Trefftz method can be found. We refer to [85] for a number of Trefftz variational formulations for Trefftz element methods where also inter-element residuals are considered.

Usually, the MFS refers to a particular combination of discrete space and variational formulation. The ansatz functions are fundamental solutions with source points placed along a curve (in 2D) or on a surface (in 3D) surrounding the computational domain Ω. It is necessary that the source points lie in the complement of Ω, since the fundamental solutions are singular at the source points. The coefficients are determined by collocation. We want to solve the boundary value problem of acoustics (2.27). To this end, the residuals

$$\begin{aligned} R_D(x) &= p(x) - g_D(x) && \text{for } x \in \Gamma_D, \\ R_N(x) &= \frac{\nabla p(x) \cdot \mathbf{n}(x)}{\mathrm{i}\omega\rho} - g_N(x) && \text{for } x \in \Gamma_N, \end{aligned} \tag{4.47}$$

are forced to vanish at M collocation points on the boundary. Unlike other Trefftz methods, the MFS can be readily used for scattering and radiation problems in unbounded domains, since fundamental solutions satisfy the Sommerfeld radiation condition. We refer to [71] for numerous references. We mention three applications of the MFS in the field of poroelasticity. Nennig *et al.* [127] applied the MFS to scattering problems from poroelastic bodies in two dimensions. Wen and Liu [180] derived the fundamental solution for a poroelastic plate in Laplace domain and applied the MFS for solving boundary value problems. Augustin [15] presented density results and a MFS for quasi-static poroelasticity.

Another Trefftz method is the Wave Based Method (WBM) introduced by Desmet [62] in 1998. It is based on propagating and evanescent plane waves for the approximation and a variational formulation. In this setting, it is applicable to convex domains. Thus, for non-convex domains a sub-structuring into smaller convex domains is performed. The WBM

was originally developed for interior acoustic problems and has been constantly developed. A review of the capabilities of the WBM is given in [59].

In the present work, we use fundamental solutions placed on a surface embracing the fluid domain to approximate the pressure field in the acoustic fluid, as it is done in the MFS. The unknown coefficients are determined by a variational formulation like in the WBM. In section 4.3, we will couple this method with the developed FEM for the poroelastic shell using similar formulations as in [93, 171]. The MFS approximates the solution in the fluid domain by a linear combination of fundamental solutions $\mathcal{G}$ weighted with coefficients c_i

$$p^a(\mathbf{x}) = \sum_{i=1}^{N_p} c_i \, \mathcal{G}(\mathbf{x}, \mathbf{y}_i). \tag{4.48}$$

The fundamental solution of the Helmholtz operator in the full 3D space is given by

$$\mathcal{G}^{3D}(\mathbf{x}, \mathbf{y}) = \frac{\mathrm{e}^{-\mathrm{i}kr}}{4\pi r}, \quad r = ||\mathbf{y} - \mathbf{x}||. \tag{4.49}$$

The point $\mathbf{x}$ is called field point, whereas $\mathbf{y}$ is called source point. We restrict our further considerations to half-space problems. This means that we assume that the upper half-space $\Omega_+ = \{(x, y, z) \in \mathbb{R}^3 | z > 0\}$ is divided by the shell structure Ω^s into two fluid domains Ω^{int} and Ω^{ext}, such that $\Omega_+ = \Omega^{int} \cup \Omega^{ext} \cup \Omega^s$. We assume a sound hard surface $\partial\Omega_+$ at $z = 0$. Thus, the normal fluid velocity vanishes,

$$\mathbf{v}^a(\mathbf{x}) \cdot \mathbf{e}_3 = 0, \quad \text{for } \mathbf{x} \in \partial\Omega_+. \tag{4.50}$$

The setting is illustrated with schematic two-dimensional representation in Figure 4.7. By

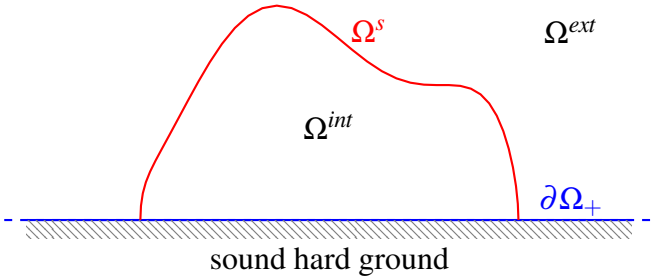

Figure 4.7: The half-space setting: Sound hard ground surface $\partial\Omega_+$, interior fluid domain Ω^{int}, exterior fluid domain Ω^{ext}, shell structure Ω^s

making use of the half-space fundamental solution, the condition at sound hard surface $\partial\Omega_+$ is fulfilled exactly. The half-space fundamental solution is given by

$$\mathcal{G}(\mathbf{x}, \mathbf{y}) = \frac{\mathrm{e}^{-\mathrm{i}kr}}{4\pi r} + \frac{\mathrm{e}^{-\mathrm{i}k\tilde{r}}}{4\pi \tilde{r}}, \quad \tilde{r} = ||\tilde{\mathbf{y}} - \mathbf{x}||, \quad \tilde{\mathbf{y}} = (y_1, y_2, -y_3). \tag{4.51}$$

In order to treat non-homogeneous problems, *i.e.* where sources are located inside the acoustic fluid domain, we extend (4.48) to

$$p^a = \sum_{i=1}^{N_s} c_i \, \mathcal{G}(\mathbf{x}, \mathbf{y}_i) + F_p, \tag{4.52}$$

where F_p are particular solutions of the in-homogeneous problem. In the present work, we consider point sources only. Thus, F_p is a linear combination of fundamental solutions

$$F_p = \sum_{s=1}^{N_p} d_s \, \mathcal{G}(\mathbf{x}, \mathbf{y}_s), \tag{4.53}$$

where d_l is the strength of an acoustic source at $\mathbf{y}_l$. In view of (2.25), the discrete fluid displacement is given by

$$\mathbf{u}^a(\mathbf{x}) = \frac{1}{\rho^a \omega^2} \sum_{i=1}^{N_p} c_i \mathcal{H}(\mathbf{x}, \mathbf{y}_i). \tag{4.54}$$

where

$$\mathcal{H}(\mathbf{x}, \mathbf{y}) = \nabla_{\mathbf{x}} \mathcal{G}(\mathbf{x}, \mathbf{y}). \tag{4.55}$$

Thus,

$$\mathcal{H}(\mathbf{x}, \mathbf{y}) \cdot \mathbf{e}_j = (1 + \mathrm{i}kr) \frac{y_j - x_j}{4\pi r^3} \, \mathrm{e}^{-\mathrm{i}kr} + (1 + \mathrm{i}k\tilde{r}) \frac{\tilde{y}_j - x_j}{4\pi \tilde{r}^3} \, \mathrm{e}^{-\mathrm{i}k\tilde{r}}. \tag{4.56}$$

In the uncoupled MFS considered in this section, either the interior acoustic problem in Ω^{int}, or the exterior acoustic problem Ω^{ext} can be tackled. In both cases, we assume that the boundary Γ of the respective domain can be decomposed into $\Gamma = \Gamma_D \cup \Gamma_N \cup \Gamma_R \cup \partial\Omega_+$. Due to the ansatz (4.52), the Helmholtz equation in Ω_+ and the hard wall condition at $\partial\Omega_+$ are fulfilled exactly. Nevertheless, the other boundary conditions cannot be fulfilled exactly, yielding the residua (4.47). Therefore, the unknown coefficients c_i in (4.52) are determined in a weighted residual sense. To this end, the boundary residua are weighted with the complex conjugate of the test functions η and their normal derivative,

$$\int_{\Gamma_D} \frac{\nabla \bar{\eta}(x) \cdot \mathbf{n}(x)}{\mathrm{i}\omega\rho} R_D(x) \, \mathrm{d}s_{\mathbf{x}} + \int_{\Gamma_N} \bar{\eta}(x) R_N(x) \, \mathrm{d}s_{\mathbf{x}} + = 0. \tag{4.57}$$

Applying a Galerkin approach, the test functions $\bar{\eta}$ are chosen to be fundamental solutions with the same source points as in (4.48). This leads to the linear system of equations

$$K^{\mathrm{MFS}} u^{\mathrm{MFS}} = f^{\mathrm{MFS}}, \tag{4.58}$$

where

$$
\begin{aligned}
K^{\mathrm{MFS}}[i,j] &= \int_{\Gamma_D} \mathcal{H}(\mathbf{x},\mathbf{y}_i)\cdot\mathbf{n}(\mathbf{x})\,\mathcal{G}(\mathbf{x},\mathbf{y}_j)\,\mathrm{d}s_{\mathbf{x}} + \int_{\Gamma_N} \mathcal{G}(\mathbf{x},\mathbf{y}_i)\,\mathcal{H}(\mathbf{x},\mathbf{y}_j)\cdot\mathbf{n}(\mathbf{x})\,\mathrm{d}s_{\mathbf{x}} \\
u^{\mathrm{MFS}}[i] &= c_i, \\
f^{\mathrm{MFS}}[i] &= \int_{\Gamma_D} \mathcal{H}(\mathbf{x},\mathbf{y}_i)\cdot\mathbf{n}(\mathbf{x}) \left(g_D - \sum_{l=1}^{N_p} d_l \mathcal{G}(\mathbf{x},\mathbf{y}_l) \right) \mathrm{d}s_{\mathbf{x}} \\
&\quad + \int_{\Gamma_N} \mathcal{G}(\mathbf{x},\mathbf{y}_i) \left(g_N - \sum_{l=1}^{N_p} d_l \mathcal{H}(\mathbf{x},\mathbf{y}_l)\cdot\mathbf{n}(\mathbf{x}) \right) \mathrm{d}s_{\mathbf{x}}.
\end{aligned}
\tag{4.59}
$$

In the classical MFS three insufficiently resolved issues arise. These are the placement of the source points [8, 42] and of the collocation points [82], as well as the ill-conditioning of the sytem matrix [41]. For the two-dimensional problem, a mathematical analysis is given in [17]. Due to the use of a variational MFS developed in the present work, no collocation points are necessary. In return, integration over the boundary is necessary. This is done by a numerical quadrature, introducing an error. This integration error has to be controlled in order to achieve reasonable results. In the present work, we simply place the source points using a constant offset in normal direction. Therefore, points have to be placed on the boundary. To this end, we use Poisson disk sampling in the case of a parametric description, whereas for an implicitly given surface we take the vertices of a triangulation.

4.3 Coupling of FEM and MFS

The goal of this section is to develop a coupling approach for the FEM and the MFS. The coupling of different numerical methods is a well known approach for acoustic-structure interaction problems. The FEM is perfectly suited for models with complex geometries while boundary related methods enable to account for the radiation of waves in domains of infinite extent. The coupling of FEM-BEM is well-known in literature. We mention [152] and [76] among others for the analysis in time domain. A FEM-BEM coupling schema for frequency domain sensitivity analysis was presented in [79]. The coupling of the FEM and the WBM has been proposed for different configurations in order to benefit from both worlds. We mention the cases of structural (FEM) - acoustic fluid (WBM) coupling [171], acoustic fluid (WBM) - poroelastic domain (FEM) coupling [93] and the coupling of two different poroelastic domains [105]. For two-dimensional soil-structure interaction problems a coupled FEM-MFS schema has been developed in [81]. Thus, two elastic sub-domains are coupled. This was extended to a 2.5-dimensional model for the prediction of vibrations due to underground railway traffic in [9]. Furthermore, we

mention [127], where an acoustic fluid domain is coupled with a poroelastic domain. Both are discretized using the MFS.

Acoustic-elastic FEM-MFS coupling. In this paragraph, we consider the case of an elastic solid which is in contact with an acoustic fluid at the interface Γ^{ae}. The individual uncoupled problems have been discretized by means of the FEM in Section 4.1 and the MFS in Section 4.2. Now, we consider the coupling of both methods. To this end, the variational formulation of the governing equations for an elastic solid is rewritten to

$$-\rho\ \omega^2 M_u(\mathbf{u}^e,\bar{\mathbf{u}}) + K_u(\mathbf{u}^e,\bar{\mathbf{u}}) - \int_{\Gamma^{ae}} \mathbf{t}^e \cdot \bar{\mathbf{u}}\ \mathrm{d}s_{\mathbf{x}} = f_V(\bar{\mathbf{u}}) + f_N(\bar{\mathbf{u}}). \tag{4.60}$$

Here, we have assumed the case $\Gamma = \Gamma_N \cup \Gamma_D \cup \Gamma^{ae}$. The case of an additional interface between an elastic solid and a poroelastic solid was commented in Section 3.3. The two coupling conditions for the interface Γ^{ae} stated in (2.82) and (2.83) are rewritten to

$$\mathbf{t}^e = -p^a\,\mathbf{n}, \quad \text{on } \Gamma^{ae}, \tag{4.61}$$

and

$$\frac{1}{\rho^a \omega^2}\nabla p \cdot \mathbf{n} - \mathbf{u}^e \cdot \mathbf{n} = 0, \quad \text{on } \Gamma^{ae}. \tag{4.62}$$

The incorporation of the first coupling condition in (4.60) yields

$$-\rho\ \omega^2 M_u(\mathbf{u}^e,\bar{\mathbf{u}}) + K_u(\mathbf{u}^e,\bar{\mathbf{u}}) + \int_{\Gamma^{ae}} p^a\,\mathbf{n}\cdot\bar{\mathbf{u}}\ \mathrm{d}s_{\mathbf{x}} = f_V(\bar{\mathbf{u}}) + f_N(\bar{\mathbf{u}}). \tag{4.63}$$

Following the variational MFS approach in Section 4.2, the second coupling condition is weighted with the complex conjugate of the test function η and integrated over the coupling interface

$$\int_{\Gamma^{ae}} \bar{\eta}(x)\left(\frac{1}{\rho^a\omega^2}\nabla p\cdot\mathbf{n} - \mathbf{u}^e\cdot\mathbf{n}\right)\ \mathrm{d}s_{\mathbf{x}}. \tag{4.64}$$

The discretization of (4.62) and (4.64) leads into a system of equations in the form of

$$\begin{bmatrix} -\omega^2 M_u + K_u & G_1 \\ -(\bar{G}_1)^\top & H \end{bmatrix} \begin{bmatrix} u_i \\ c_k \end{bmatrix} = \begin{bmatrix} f_V + f_N - f_{ae} \\ -f_p \end{bmatrix}. \tag{4.65}$$

The matrices M_u and K_u are the mass and the stiffness matrix and $f_V + f_N$ is the load vector, which arise from the FEM discretization. In order to state the entries of the other matrices, we use the global index $i = i(i_1, i_2, i_3, l)$, which refers to the respective finite

element function $N_{i_1}(\mathbf{x})\overset{(i_3)}{V}(\tilde{\tau}^l(\mathbf{x}))\overset{(i_3,l)}{u}_{i_2}\mathbf{e}_{i_2}$. Thus,

$$\begin{aligned}
G_1[i,k] &= \int_{\Gamma^{ae}} N_{i_1}(\mathbf{x})\overset{(i_3)}{V}(\tilde{\tau}^l(\mathbf{x}))\,\mathcal{G}(\mathbf{x},\mathbf{y}_k)\,\mathbf{e}_{i_2}\cdot\mathbf{n}^e(\mathbf{x})\,\mathrm{d}s_x,\\
H[k,l] &= \frac{1}{\rho^a\omega^2}\int_{\Gamma^{ae}} \mathcal{H}(\mathbf{x},\mathbf{y}_l)\cdot\mathbf{n}(\mathbf{x})\,\bar{\mathcal{G}}(\mathbf{x},\mathbf{y}_k)\,\mathrm{d}s_x,\\
f_{ae}[i] &= \sum_{s=1}^{N_s} d_s \int_{\Gamma^{ae}} N_{i_1}(\mathbf{x})\,\mathcal{G}(\mathbf{x},\mathbf{y}_s)\,\mathbf{e}_{i_2}\cdot\mathbf{n}^e(\mathbf{x})\,\mathrm{d}s_{\mathbf{x}},\\
f_p[k] &= \sum_{s=1}^{N_s} \frac{d_s}{\rho^a\omega^2}\int_{\Gamma^{ae}} \mathcal{H}(\mathbf{x},\mathbf{y}_s)\cdot\mathbf{n}(\mathbf{x})\,\bar{\mathcal{G}}(\mathbf{x},\mathbf{y}_k)\,\mathrm{d}s_{\mathbf{x}}.
\end{aligned} \tag{4.66}$$

We remark that the integrals are transformed to the reference element for their numerical evaluation by means of a quadrature rule.

Acoustic-poroelastic FEM-MFS coupling. We proceed with the coupling in the case of an acoustic fluid where the pressure field is approximated by an MFS ansatz and a poroelastic solid, which is discretized by the FEM. To this end, we rewrite the variational formulation of the governing equations for a poroelastic solid stated in (2.77) to

$$\begin{aligned}
-K_u(\mathbf{u},\bar{\mathbf{u}}) + \tilde{M}_u(\mathbf{u},\bar{\mathbf{u}}) + D(p,\bar{\mathbf{u}}) - L(p,\bar{\mathbf{u}}) + f_u(\bar{\mathbf{u}}) - \int_{\Gamma^{ap}} \mathbf{t}^{\mathrm{tot}}\cdot\bar{\mathbf{u}}\,\mathrm{d}s_{\mathbf{x}} = 0,\\
K_p(p,\bar{p}) + M_p(p,\bar{p}) + D(\bar{p},\mathbf{u}) - L(\bar{p},\mathbf{u}) + f_p(\bar{p}) + \int_{\Gamma^{ap}} \frac{\mathbf{q}\cdot\mathbf{n}^p}{i\omega}\bar{p}\;\mathrm{d}s_{\mathbf{x}} = 0,
\end{aligned} \tag{4.67}$$

with $\tilde{M}_u(\mathbf{u},\bar{\mathbf{u}}) = \omega^2\left(\rho+\beta\rho^f\right)M_u(\mathbf{u},\bar{\mathbf{u}})$. Here, we have assumed that $\Gamma = \Gamma_N\cup\Gamma_D\cup\Gamma^{ap}$. The coupling conditions on Γ^{ap} stated in (2.85) to (2.87) are rewritten to

$$\mathbf{t}^{\mathrm{tot}} = -p^a\,\mathbf{n}^p, \tag{4.68}$$

$$\frac{1}{\mathrm{i}\omega}\mathbf{q}\cdot\mathbf{n} = \frac{\nabla p^a\cdot\mathbf{n}}{\rho^a\omega^2} - \mathbf{u}^s\cdot\mathbf{n}, \tag{4.69}$$

$$p^a - p = 0\,. \tag{4.70}$$

We incorporate the coupling conditions (4.68) and (4.69) in the first equation of (4.67). This yields for the integral over Γ^{ap},

$$-\int_{\Gamma^{ap}} \mathbf{t}^{\mathrm{tot}}\cdot\bar{\mathbf{u}}\,\mathrm{d}s_{\mathbf{x}} = \int_{\Gamma^{ap}} p\,\mathbf{n}\cdot\bar{\mathbf{u}}\,\mathrm{d}s_{\mathbf{x}}. \tag{4.71}$$

Furthermore, coupling conditions (4.69) are incorporated in the second equation of (4.67). For the integral over Γ^{ap}, we obtain

$$\int_{\Gamma^{ap}} \frac{\mathbf{q}\cdot\mathbf{n}^p}{i\omega}\bar{p}\ \mathrm{d}s_{\mathbf{x}} = \int_{\Gamma^{ap}} \left(\frac{\nabla p^a\cdot\mathbf{n}}{\rho^a\omega^2} - \mathbf{u}^s\cdot\mathbf{n}\right)\bar{p}\ \mathrm{d}s_{\mathbf{x}}. \tag{4.72}$$

Following the variational MFS approach in Section 4.2, the coupling condition (4.70) is weighted with the gradient of the complex conjugate of the test function η and integrated over the coupling interface

$$\int_{\Gamma^{ae}} \nabla\bar{\eta}(x)\cdot\mathbf{n}\,(p^a - p)\ \mathrm{d}s_{\mathbf{x}} = 0. \tag{4.73}$$

In order state the entries of the newly introduced matrices, we use the global index $j = j(j_1, j_2, l)$, which refers to the respective finite element function $N_{i_1}(\mathbf{x})\overset{(j_2)}{V}(\tilde{\tau}^l(\mathbf{x}))\overset{(j_2,l)}{p}_{i_2}$.

$$\begin{bmatrix} K_u - \tilde{M}_u & L - D - M_\Gamma & 0 \\ (D)^\top - (L)^\top - (\bar{M}_\Gamma)^\top & K_p + M_p & G_2 \\ 0 & (-\bar{G}_2)^\top & H \end{bmatrix} \begin{bmatrix} u_i \\ p_j \\ c_k \end{bmatrix} = \begin{bmatrix} f_N^u - f_{ap}^u \\ -f_{N_p} - f_{ap}^p \\ -f_{p_2} \end{bmatrix} \tag{4.74}$$

where the newly introduced matrices and vectors are

$$\begin{aligned}
G_2[j,k] &= \int_{\Gamma^{ap}} N_{j_1}(\mathbf{x})\overset{(j_2)}{V}(\tilde{\tau}^l(\mathbf{x}))\ \mathcal{H}(\mathbf{x},\mathbf{y}_k)\cdot\mathbf{n}(\mathbf{x})\ \mathrm{d}s_x, \\
M_\Gamma[i,j] &= \int_{\Gamma^{ap}} N_{j_1}(\mathbf{x})\overset{(j_2)}{V}(\tilde{\tau}^l(\mathbf{x}))N_{i_1}(\mathbf{x})\overset{(i_3)}{V}(\tilde{\tau}^l(\mathbf{x}))\,\mathbf{e}_{i_2}\cdot\mathbf{n}(\mathbf{x})\ \mathrm{d}s_x, \\
f_{ap}^u[i] &= \sum_{s=1}^{N_s} d_s \int_{\Gamma^{ap}} N_{i_1}(\mathbf{x})\ \overset{(i_3)}{V}(\tilde{\tau}^l(\mathbf{x}))\ \mathcal{G}(\mathbf{x},\mathbf{y}_s)\,\mathbf{e}_{i_2}\cdot\mathbf{n}^e(\mathbf{x})\ \mathrm{d}s_{\mathbf{x}}, \\
f_{ap}^p[j] &= \sum_{s=1}^{N_s} d_s \int_{\Gamma^{ap}} N_{j_1}(\mathbf{x})\ \overset{(j_2)}{V}(\tilde{\tau}^l(\mathbf{x}))\ \mathcal{H}(\mathbf{x},\mathbf{y}_s)\cdot\mathbf{n}^e(\mathbf{x})\ \mathrm{d}s_{\mathbf{x}}, \\
f_{p_2}[k] &= \sum_{s=1}^{N_s} \frac{d_s}{\rho^a\omega^2} \int_{\Gamma^{ap}} \mathcal{G}(\mathbf{x},\mathbf{y}_s)\ \bar{\mathcal{H}}(\mathbf{x},\mathbf{y}_k)\cdot\mathbf{n}(\mathbf{x})\ \mathrm{d}s_{\mathbf{x}}.
\end{aligned} \tag{4.75}$$

5 VERIFICATION

The aim of this chapter is to verify the implementation of the methods developed in Chapter 4. In order to ensure the reliability of a numerical simulation software, verification and validation ($V\&V$) are unavoidable tasks [128, 130]. Figure 5.1 illustrates the relation between these activities. An observed real world phenomenon can be modeled by mathe-

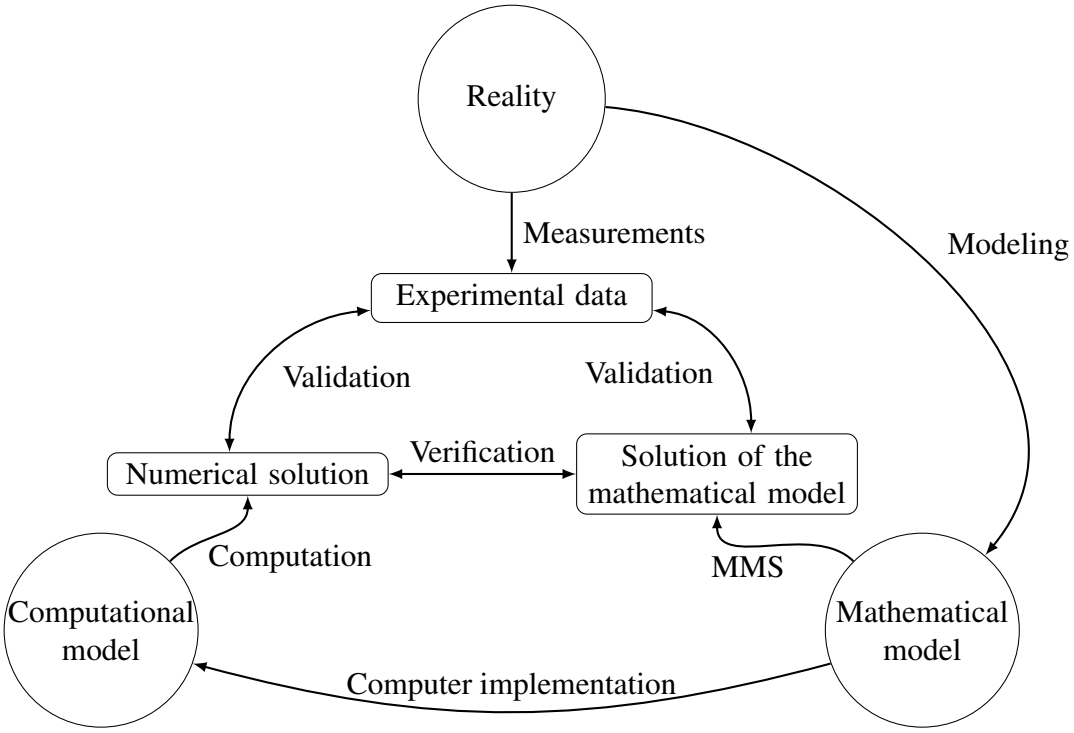

Figure 5.1: The role of $V\&V$ in numerical simulation, based on [157]

matical means, leading to an explicit mathematical model. Since the availability of explicit solutions to mathematical models describing real world problems is limited, the use of numerical solutions is inevitable. The computer implementation of the mathematical model leads to the computational model. Each of these steps introduces errors, which have to be assessed by $V\&V$. The process of validation determines how accurately the mathematical model represents the real (physical) problem. The aim of verification is to show that the numerical method is able to produce a solution which approximates the exact solution of the mathematical model. Thus, one is interested in the numerical error, which is defined as the difference between the numerical solution and the exact solution. The comparison of numerical results with measurement data is only feasible if the results are not significantly

influenced by the numerical error. Therefore, the process of verification has to precede the validation process. Verification activities can be split into code verification and solution verification. Code verification represents the process of demonstrating that the governing equations, as implemented in the code, are solved consistently. Solution verification is the assessment (estimation) of the numerical error in situations where no exact solution is known [129]. According to [151], the most rigorous tests for code verification are the order-of-accuracy tests. For any discretization method, we expect that the discretization error decreases as the discretization is refined. Within an order-of-accuracy test, the observed rate of decrease in the discretization error is compared with the theoretical rate. In order to evaluate the discretization error, exact solutions are needed. These exact solutions can be constructed by the Method of Manufactured Solutions (MMS) [128, 147, 151, 159]. This method has been applied to a Reynolds-Averaged Navier Stokes solver in [67], to nonlinear membrane elements in [74] within fluid structure interaction in [73, 75], to a conjugate heat transfer solver in [172], and to a Cahn–Hilliard equation solver in [95], among many others.

In the present work, we are concerned with shell problems. Thus, the problem domain may be curved. However, explicit solutions are only known for special geometries (mostly flat, cylindrical, spherical problems) and special loading conditions. Using these solutions for code verification might not be rigorous. Some terms might be zero for these special problems and will not be tested. The MMS aims to construct general problems such that all parts of the code are tested. In order to explain the central idea of the MMS, we consider the following model problem: Let $\mathfrak{L}$ be a differential operator. For given functions f and g, find the function u, such that

$$\mathfrak{L}\, u = f \quad \text{in } \Omega, \qquad u = g \quad \text{on } \partial\Omega. \tag{5.1}$$

In order to obtain a solution for a general problem, we fix a chosen manufactured solution u^M instead of the functions f and g. These functions are determined form the governing equations, *i.e.* $f = \mathfrak{L}\, u^M$ and g is the restriction of u on $\partial\Omega$. This procedure hinges on the fact that the application of $\mathfrak{L}$ is manageable systematically. Nevertheless, the resulting source term f can easily become complicated [116]. Therefore, the use of computer algebra software is standard. In the present work, we use [181] for the computation of the source terms. To summarize, we follow the following outline in the code verification examples [150]:

1. Choose the form of the problem domain
2. Choose the form of the manufactured solution
3. Derive the modified governing equations
4. Solve the discrete form of the modified governing equations on multiple meshes
5. Evaluate the numerical error (5.4) and the *eoc* (5.3)

6. Apply the order-of-accuracy test

In view of shell problems it is important to verify the code at general geometries. Therefore, we added the first point in comparison to [150]. In the case of the MFS, we are not aware of an algebraic convergence rate. Thus, an order-of-accuracy test cannot be performed. Nevertheless, the convergence can be observed.

5.1 Verification of the poroelastic shell FEM

In this section, we apply code verification to the poroelastic shell FEM developed in Section 4.1 based on order-of-accuracy tests and on the MMS. The necessary prerequisite to apply an order-of-accuracy test to a numerical schema is the knowledge of a formal order of convergence and exact solutions. Thus, one has to know an estimate of the type

$$||u^{exact} - u^{numerical}|| \leq C\, h^q\, ||u^{exact}||, \tag{5.2}$$

where C is a constant and h is a characteristic discretization parameter. Here, we refer to a characteristic element size. Then q is called the formal order of convergence with respect to the norm $||\cdot||$. For two meshes with characteristic element sizes h_1 and h_2, the experimental order of convergence (*eoc*) is defined as

$$eoc = \frac{\log(e_1) - \log(e_2)}{\log(h_1) - \log(h_2)}, \tag{5.3}$$

where

$$e_i = ||u^{exact} - u^{numerical}_{h_i}|| \tag{5.4}$$

is the numerical error corresponding to the discretization h_i. The code is verified, if the *eoc* matches the formal order of convergence within the asymptotic range. For the FEM with arbitrary ansatz order p applied here, we expect $q = p+1$ for the error in the L_2 norm for smooth solutions.

In the case of the elastic solid problem (2.38), the procedure above is straightforwardly applicable. The implemented finite element code needs the components b^i of the source term $\mathbf{b} = b^i \mathbf{e}_i$ with respect to the global Cartesian frame. In view of (3.40), they are given by

$$\begin{aligned} b^i &= -\left(\sigma^{jl}_{,j} + \sigma^{kl}\Gamma_{kj}{}^{j} + \sigma^{jk}\Gamma_{kj}{}^{l}\right) J^i_l, \\ \sigma^{kl} &= \mathbb{C}^{klij}\epsilon_{ij}. \end{aligned} \tag{5.5}$$

The components ϵ_{ij} and $\mathbb{C}^{klij}$ are given in (3.41) and (3.42) respectively. In the case of the poroelastic solid problem (2.71), we include artificial source terms in the formulation, in

order to apply the MMS. We modify the respective equations (2.71) to

$$\begin{aligned} \mathbf{b}^u &= \nabla \cdot \boldsymbol{\sigma}^{\mathrm{tot}} + \omega^2 \mathbf{u} \left(\rho + \rho_f \beta\right) - \beta \nabla p, \\ b^p &= -\frac{\beta}{\omega^2 \rho_f} \Delta p + (\beta + \alpha) \nabla \cdot \mathbf{u} + \frac{\phi^2}{R} p. \end{aligned} \tag{5.6}$$

We remark that these source terms have no physical meaning. They are incorporated in the variational formulation and in the FEM easily, leading to additional entries in the load vectors. All necessary differential operators are stated in local coordinates in (3.27), (3.32), (3.33), (3.39) and (3.40).

Verification examples. We have checked the order of convergence for a number of examples, considering different material parameters, frequencies, geometries, displacement fields, and pressure fields. In all examples, the optimal asymptotic order of convergence could be observed.

In this section, we show the results of four verification examples in total. In the first three examples, we use a parametric description of the reference surface, whereas in the fourth example, an implicit description is used. In the first example, we prescribe the trivial displacement solution and a non-trivial pressure solution. In the second example, we make it the other way round. In both examples, we use the reference surface given by

$$\begin{aligned} x &= \theta^1, \\ y &= \theta^2, \\ z &= \theta^1 \theta^2 \end{aligned} \tag{5.7}$$

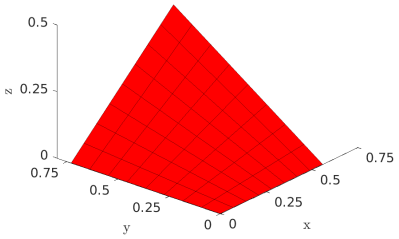

and $\theta^1 \in [0, 0.56]$ and $\theta^2 \in [0, 0.73]$. In the third example, we consider a part of a sphere singularly parametrized by

$$\begin{aligned} x &= \cos(\theta^2) \sin(\theta^1), \\ y &= \sin(\theta^2) \sin(\theta^1), \\ z &= \cos(\theta^1), \end{aligned} \tag{5.8}$$

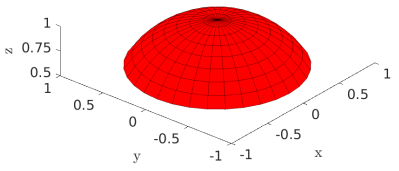

and $\theta^1 \in [0, 1]$ and $\theta^2 \in [0, 2\pi]$. We remark that this parametrization fulfills the condition in (4.34). In all three examples we choose for the thickness coordinate $\theta^3 \in [-0.05, 0]$. We use the material parameters of polyurethane given in Table A.3 and an angular frequency $\omega = 20\,\mathrm{s}^{-1}$. For the construction of the manufactured solution, we take the structure of the shell model into account. Therefore, the solution is defined by specifying the parameters

	Example 1	Example 2	Example 3
$\overset{(1)}{u_i^M}$	$[0 \quad 0 \quad 0]$	$[\cos(20\theta^1) \quad 0 \quad 0]$	$[xy \quad 0 \quad 0]$
$\overset{(2)}{u_i^M}$	$[0 \quad 0 \quad 0]$	$[\cos(20\theta^1) \quad 0 \quad 0]$	$[x \quad 0 \quad 0]$
$\overset{(n)}{u^M}$	0	$\exp(\theta^2)$	z
$\overset{(1)}{p^M}$	$\exp(\theta^1)\sin(20\theta^2)$	0	z
$\overset{(2)}{p^M}$	$\exp(\theta^2)\sin(\theta^1)$	0	0
$\overset{(n)}{p^M}$	$\cos(\theta^1)\sin(\theta^2)$	0	0

Table 5.1: Parameters for the manufactured solutions

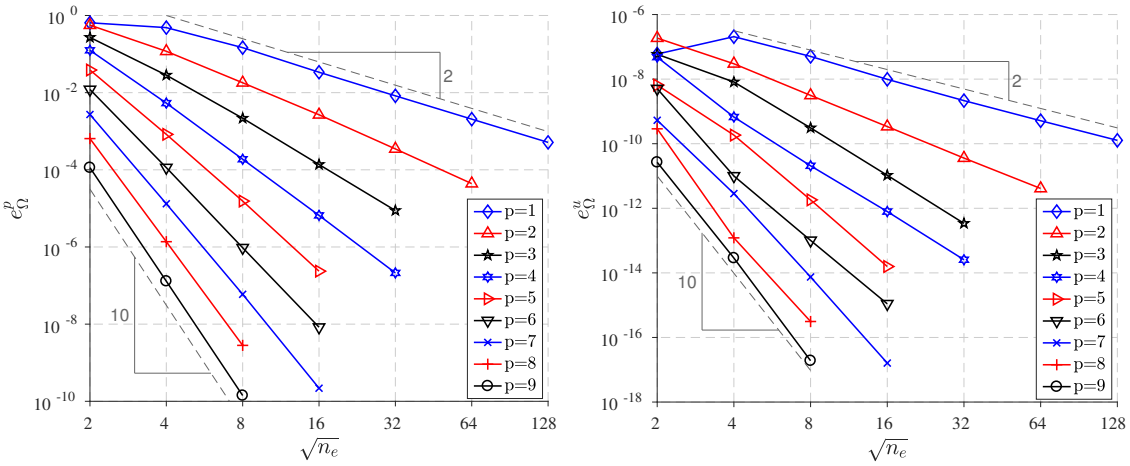

Figure 5.2: Example 1: pressure error e^p_Ω (left), displacement error e^u_Ω (right)

in (3.61) and (3.65). For the presented examples, these parameters are given in Table 5.1. The errors at multiple meshes with n_e elements each are illustrated in the Figures 5.2 - 5.4. In all graphs, the respective absolute error defined by

$$\begin{aligned} e^u_\Omega &= \sqrt{\int_\Omega (\mathbf{u}-\mathbf{u}^M)\cdot(\mathbf{u}-\mathbf{u}^M)\,\mathrm{d}\mathbf{x}}, \\ e^p_\Omega &= \sqrt{\int_\Omega (p-p^M)^2\,\mathrm{d}\mathbf{x}} \end{aligned} \tag{5.9}$$

is plotted. Therein, $\mathbf{u}$ and p denote the numerical solution, whereas $\mathbf{u}^M$ and p^M denote

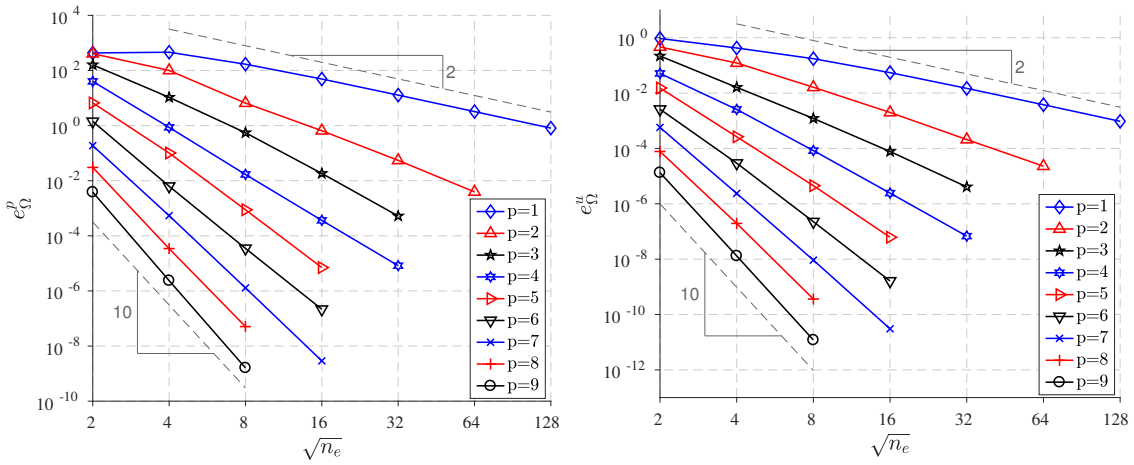

Figure 5.3: Example 2: pressure error e^p_Ω (left), displacement error e^u_Ω (right)

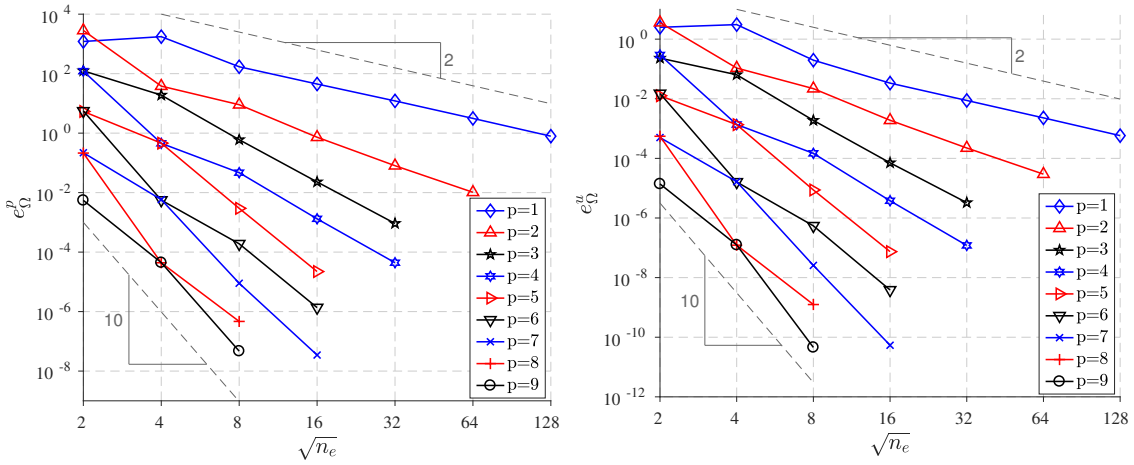

Figure 5.4: Example 3: pressure error e^p_Ω (left), displacement error e^u_Ω (right)

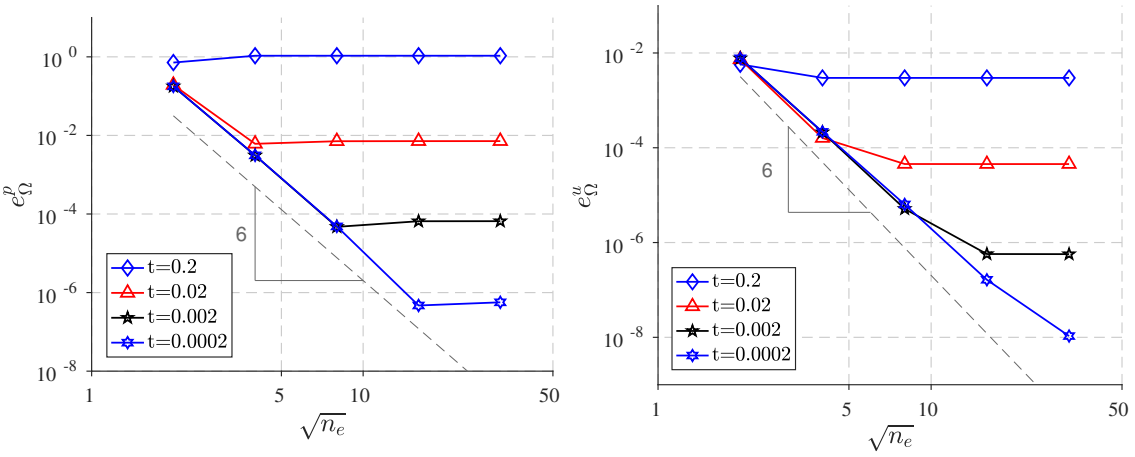

Figure 5.5: Example 4: pressure error e^p_Ω (left), displacement error e^u_Ω (right)

the manufactured solutions. We observe the optimal convergence rate in all examples. Furthermore, we see from Figure 5.3 that a small discretization error in the displacement field leads to large error in the pressure field. This is due to the conditioning of the physical problem and depends on the material parameters. Therefore, we conclude that a accurate discretization of the displacement field is necessary in order to obtain an accurate pressure approximation.

Next, we discuss the results of the fourth verification example for the poroelastic shell FEM in the case of an implicitly given reference surface. The considered spherical reference surface is given by $\phi = x^2 + y^2 + z^2 - 1$ and $B = [0,2]^3$. The shell volume has the extension t in the thickness direction and is symmetric around the reference surface. We prescribe the solution as

$$\mathbf{u}^M = \begin{bmatrix} xyz \\ xyz \\ xyz \end{bmatrix}, \tag{5.10}$$

and

$$p^M = xyz. \tag{5.11}$$

It is important to note that this solution cannot be exactly represented by the shell model. Therefore, a modeling error and a discretization error occurs. We use quintic shape functions for the discretization of a series of problems with decreasing thickness t. The results are depicted in Figure 5.5. We observe that the modeling error dominates in the case of thick shells. Therefore, a mesh refinement cannot reduce the overall error in this case. However, with decreasing thickness, the modeling error decreases and the discretization error dominates for the coarse meshes. In this regime, we observe the expected order of convergence of the FEM.

5.2 Verification of the MFS implementation

This section deals with the verification of the MFS for uncoupled acoustic fluid problems. To this end, we present the results of two examples. In both cases, the considered fluid is air with the material parameters given in Table A.1.

In the first example, an interior problem is considered. The domain Ω^{int} is bounded by the plane $\partial\Omega_+$ and a parametrically given surface Γ,

$$\begin{aligned} x &= \cos(\theta^1)\sin(\theta^2), \\ y &= 2\sin(\theta^1)\sin(\theta^2), \\ z &= \frac{1}{2}\cos(\theta^2), \end{aligned} \tag{5.12}$$

where $\theta^1 \in [0, 2\pi]$ and $\theta^2 \in [0, \frac{\pi}{2}]$, see Figure 5.6. The constructed solution is obtained by

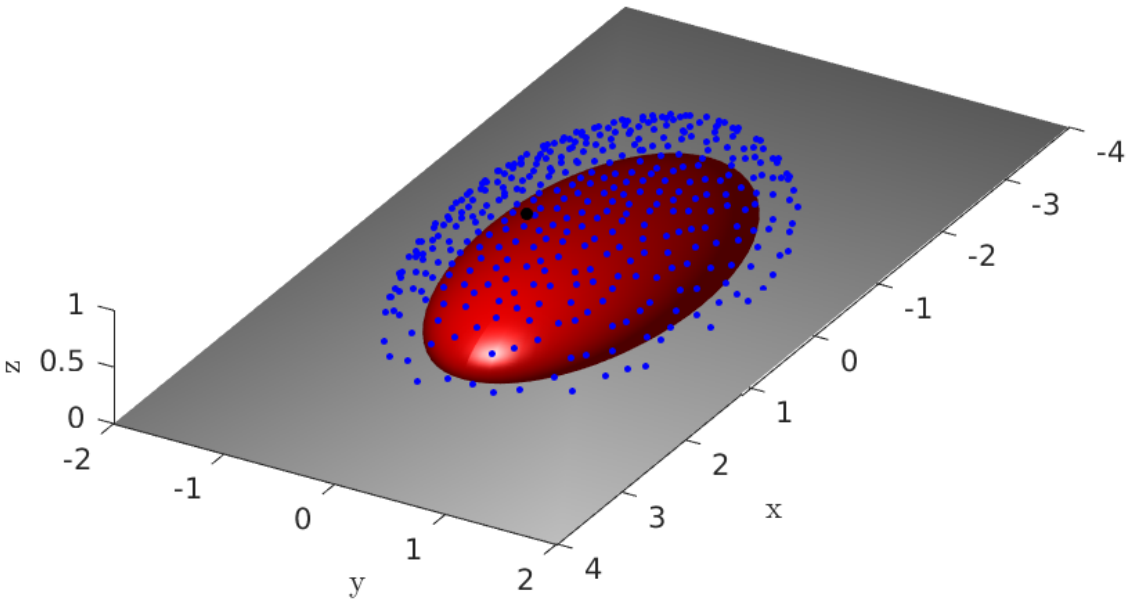

Figure 5.6: Configuration of the parametric MFS verification example: Sound hard plane at $z = 0$ (gray), sound hard surface Γ (red), MMS source point (black), MFS source points (blue)

means of the fundamental solution. Therefore, we specify the point $\mathbf{y}_0 = [1\,\text{m},\ 0\,\text{m},\ 1\,\text{m}]$, which lies outside the problem domain. This defines the sought solution according to

$$p^M(\mathbf{x}) = \mathcal{G}(\mathbf{x}, \mathbf{y}_0) \qquad \text{for } \mathbf{x} \in \Omega^{\text{int}}. \tag{5.13}$$

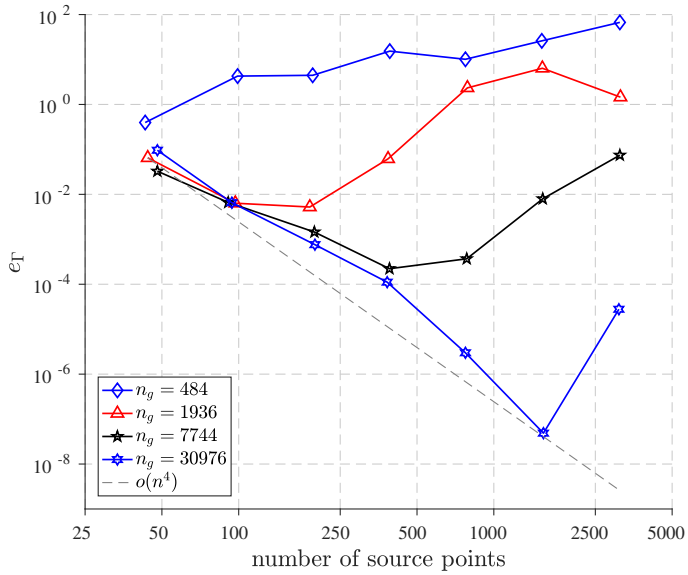

Figure 5.7: Error convergence for the parametric MFS verification example

The boundary data is derived from this solution as

$$g_N^M(\mathbf{x}) = \mathcal{H}(\mathbf{x}, \mathbf{y}_0) \cdot \mathbf{n}(\mathbf{x}) \qquad \text{for } \mathbf{x} \in \Gamma. \tag{5.14}$$

This boundary data is the input for the numerical method. The source points for the approximation are obtained by placing points on Γ and moving each 0.3 m in the direction normal to Γ. The problem setting and a source point configuration are depicted in Figure 5.6. We investigate the acoustic problem at a frequency $f = 200\,\text{Hz}$. In order to study the convergence behavior we introduce the relative error

$$e_\Gamma = \sqrt{\frac{\int_\Gamma (p^\text{M} - p)^2 \, \mathrm{d}s_\mathbf{x}}{\int_\Gamma (p^\text{M})^2 \, \mathrm{d}s_\mathbf{x}}}. \tag{5.15}$$

We evaluate this error for a number of solutions obtained with different number of source points. Furthermore, we study the influence of the numerical integration. The computed errors are plotted in Figure 5.7 for different number of quadrature points n_g used. It is evident that the integration has to be sufficiently accurate in order to obtain an accurate result. Nevertheless, very accurate solutions are possible with only a few source points for the solution approximation.

In the second verification example, we consider an exterior problem. The unbounded

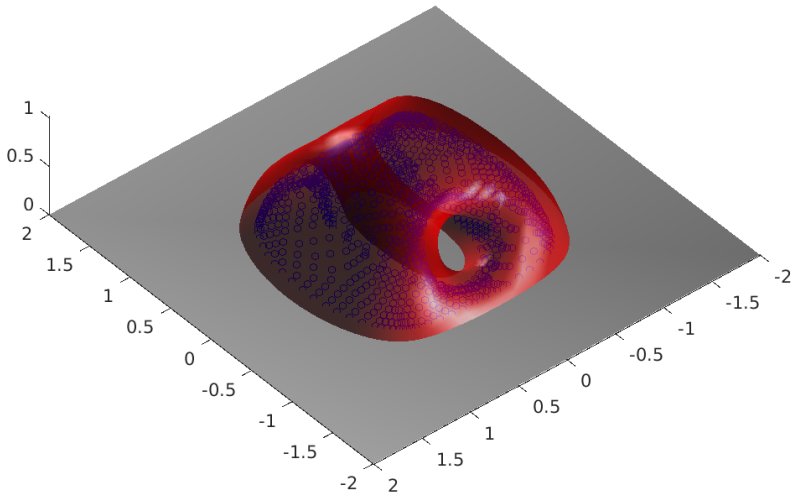

Figure 5.8: Configuration of the implicit MFS verification example: Sound hard plane at $z = 0$ (gray), sound hard surface Γ (red), MMS source point (black), MFS source points (blue)

problem domain is given as $\{(x,y,z)|\phi(x,y,z) > 0\} \cap \Omega_+$, where

$$\begin{aligned}\phi(x,y,z) = &\left(\left(x^2+y^2-1\right)^2+\left(\frac{1}{2}+z\right)^2\right)\times \\ &\times\left(x^2+\left(\frac{25}{16}y^2-1+\left(\frac{1}{5}+z\right)^2\right)^2\right)-\frac{4}{5}.\end{aligned} \tag{5.16}$$

The geometry of the problem and a source point configuration is depicted in Figure 5.8. We use $y_0 = [0.7\,\mathrm{m},\ 0.7\,\mathrm{m},\ 0.25\,\mathrm{m}]$ for the construction of the solution and the boundary data by means of (5.13) and (5.14). Again, we solve the acoustic problem at $f = 200\,\mathrm{Hz}$. The convergence behavior of the error (5.15) is plotted in Figure 5.9. We observe that the MFS is able to reproduce the solution accurately in the case of this geometrically complex problem as well. As in the previous example, we see that a sufficient number of quadrature points is necessary in order to obtain stable results.

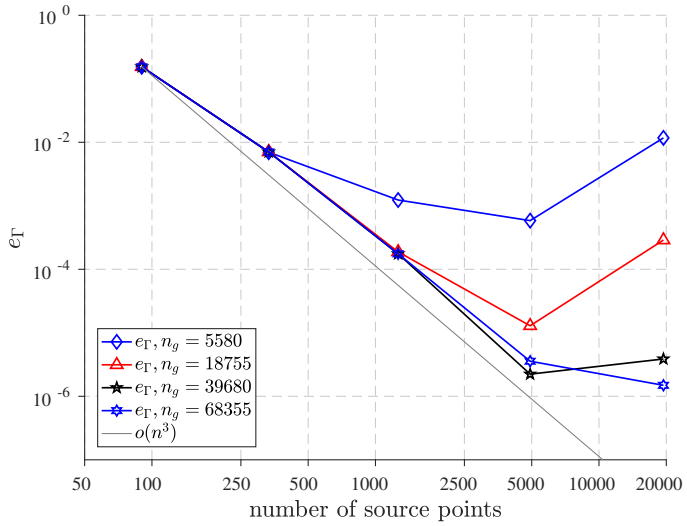

Figure 5.9: Error convergence for the implicit MFS verification example

5.3 Verification of the coupled method

In this section, we are concerned with the verification of the coupled MFS-FEM developed in Section 4.3. To this end, we consider radial symmetric problems, which allow for a closed form solution. Thus, we consider a spherical shell structure separating the upper half space into an interior and an exterior domain. The exact solutions of the three-dimensional problems are derived in Appendix B. However, the radial symmetric solutions are not the exact solutions to the shell problem. Due to the use of the shell model, a modeling error is introduced.

The reference surface for the shell structure is a hemisphere with unit radius. First, we consider the case of an elastic aluminum (see for the material parameters) structure with a thickness of $t = 0.025\,\mathrm{m}$. The used material parameters are given in Table A.2. In this example, an implicit geometry description of the hemisphere is used. The displacement of the shell is discretized with quartic finite element shape functions. The interior and exterior fluid pressure is discretized by means of the MFS. The error according to (5.15) is evaluated for the exterior acoustic fluid and plotted in Figure 5.10. The error is evaluated for varying finite element meshes and for varying number of MFS source points. The finite element meshes are identified by their number of elements n_e. Depending on the used discretization, the error is dominated either by the FEM or the MFS. This verifies the coupled method for the case of the acoustic fluid - elastic solid coupling.

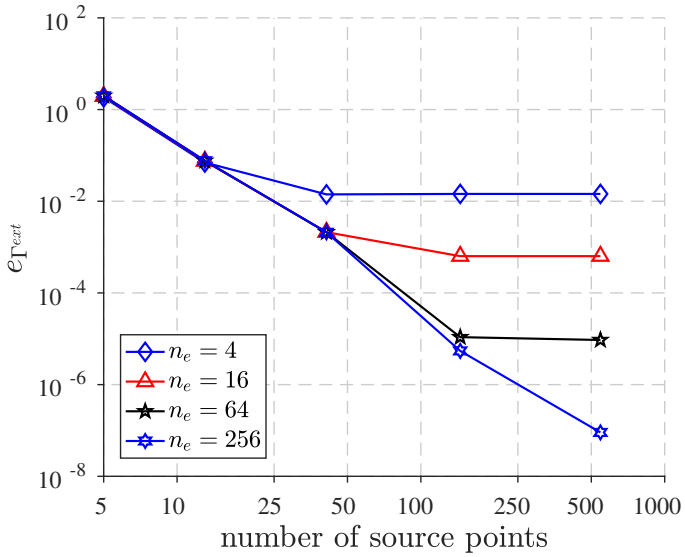

Figure 5.10: Error e_Γ for the exterior fluid in case of the coupled MFS-FEM: elastic structure and implicitly given reference surface

Next, we consider a poroelastic polyurethane shell structure separating the interior domain from the exterior domain. The material parameters are given in Table A.3. The spherical

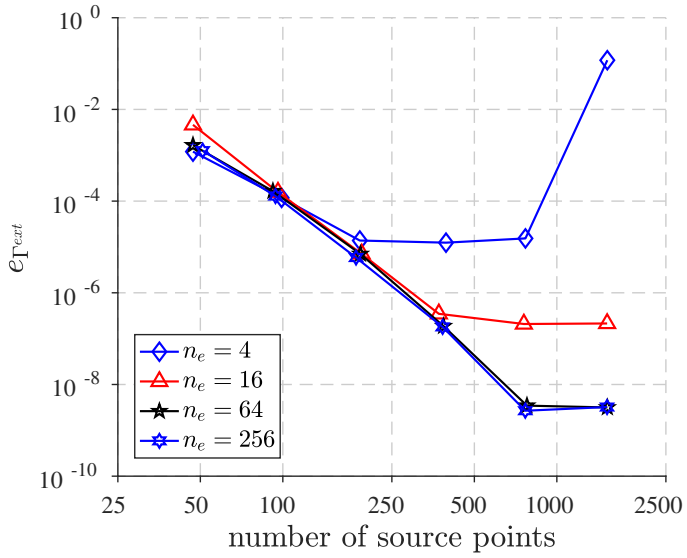

Figure 5.11: Error e_Γ for the exterior fluid in case of the coupled MFS-FEM: poroelastic structure and parametrically given reference surface

shell is described parametrically and has a thickness of $t = 0.002\,\text{m}$. Quartic finite element shape functions are used for the discretization of the displacement and pressure field of the shell structure. The error according to (5.15) is evaluated for the exterior acoustic fluid and plotted in Figure 5.11. The numerical integration for all matrix entries is done on the finite elements. In the case of $n_e = 4$, we can see the instability, which arises due to the insufficient numerical integration. However, we do not observe such instability in the case of the other meshes. In the present example, we see that due to the modeling error the minimal achievable error is around 10^{-9}. Up to this error, we observe the convergence of the coupled method. Hence, this examples verifies the coupled method for the case of acoustic fluid - poroelastic solid coupling.

6 NUMERICAL RESULTS

In the previous chapter, the implemented numerical methods were verified. In this chapter, the capabilities of the developed methods are shown on the basis of more examples. To this end, we consider three categories of problems. In the first category, the uncoupled FEM is used to solve the Scordelis-Lo roof problem and to investigate the deformation of a gyroid surface. The second category deals with acoustic problems, which are solved with the uncoupled MFS. Here, an interior as well as an unbounded exterior problem are considered. The domain of the interior problem is bounded by a complex surface, which is defined implicitly. In the exterior problem, the scattering at an assembly of spheres is studied. In the third category, coupled problems are given. We investigate the sound transmission from the inside of two cavities bounded by a poroelastic shell structure to the outside. In one example the reference surface of the shell is given parametrically, whereas in the other it is given implicitly.

6.1 Finite Element Method

6.1.1 Scordelis-Lo roof

We consider the Scordelis-Lo roof problem, described in [114]. It is a popular benchmark test to assess the performance of finite elements for thin-walled structures. The static deformation of an elastic shell is investigated. The cylindrical roof (radius $r = 25\,\mathrm{m}$) is supported by rigid diaphragms at the ends ($x = 0\,\mathrm{m}$ and $x = 50\,\mathrm{m}$), *i.e.* $u_y = u_z = 0\,\mathrm{m}$. All other surfaces are free. The geometry and the material parameters are depicted in Figure 6.1. The structure is subjected to gravity loading with $\mathbf{b} = -\mathbf{e}_z\, 360\,\mathrm{N/m^3}$.

For the parametrization of the reference surface, we use

$$\begin{aligned} x &= 50\, f(\theta^2), \\ y &= 25 \sin\left(\frac{40\pi\, f(\theta^1)}{180}\right), \\ z &= 25 \cos\left(\frac{40\pi\, f(\theta^1)}{180}\right), \end{aligned} \tag{6.1}$$

where the mapping

$$\kappa(\tau) = \tau((3-2\tau)\tau + b(1-3\tau+2\tau^2)) \quad \text{with } b = \frac{1}{100}, \tag{6.2}$$

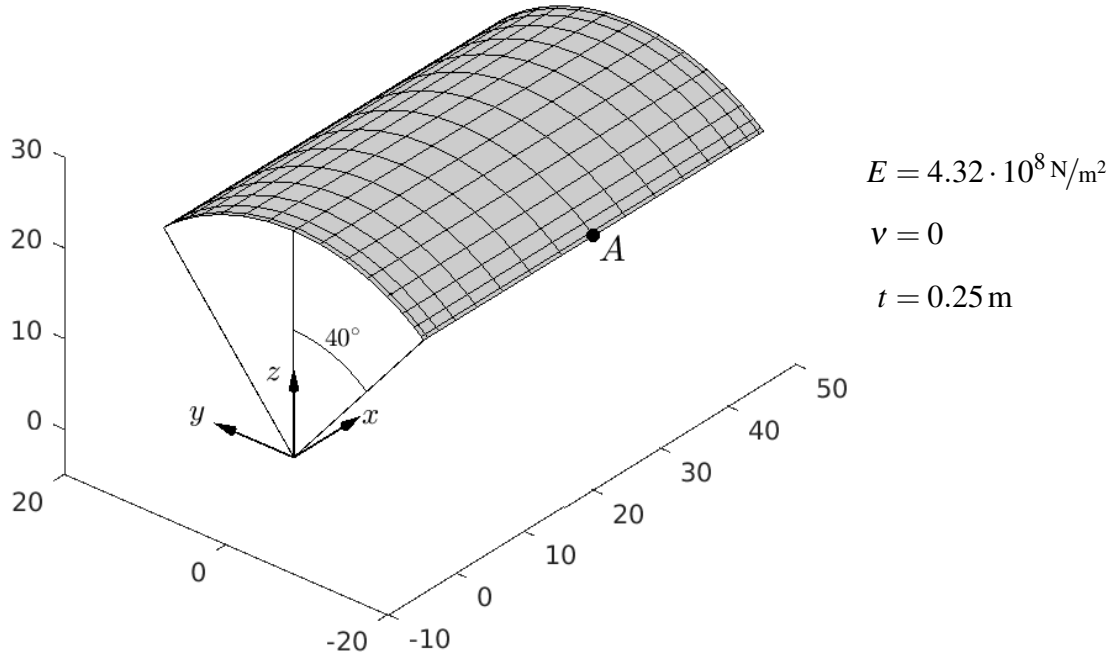

Figure 6.1: Problem description of the Scordelis-Lo-Roof

is deployed. We use κ in order to capture the boundary layer. The parameter space is given by $\theta^1 \in [0,1]$ and $\theta^2 \in [0,1]$. In Figure 6.1 a 16×16 element mesh mapped to the real space is illustrated.

We study the vertical displacement of point A, which is located in the middle of one free edge and on the mid-surface. We remark that the vertical displacement varies considerably trough-the-thickness. The results for different ansatz orders and meshes are given in Table 6.1. It is evident that the low order methods are effected by locking. The results obtained

Number of elements	4	16	64	256
Linear	-0.0026073	-0.0016144	-0.0044508	-0.0126987
Quadratic	-0.0019732	-0.0305159	-0.1354229	-0.2741197
Cubic	-0.0301026	-0.2470338	-0.2968267	-0.3012622
Quartic	-0.1675085	-0.2967069	-0.3012862	-0.3014015
Quintic	-0.2888778	-0.3012049	-0.3013835	-0.3014021
Sextic	-0.2979929	-0.3013161	-0.3014014	-0.3014026
Septic	-0.3014056	-0.3013603	-0.3014014	-0.3014026
Octic	-0.3012498	-0.3013926	-0.3014021	-0.3014026

Table 6.1: Vertical displacement at point A

with linear ansatz functions are far from the converged solution $u_z = -0.3014\,\mathrm{m}$. Raising the ansatz order reduces the locking phenomena. Without resorting to other techniques to reduce the locking, we advise to use at least quartic ansatz functions. In [114] a reference value $u_z = -0.3024\,\mathrm{m}$ for the vertical displacement at point A is reported. For a shell model based on equivalent seven-parameter kinematics, $u_z = -0.3008\,\mathrm{m}$ is computed in [68]. Therefore, our results are in accordance with the values found in literature.

6.1.2 Gyroid

In this example, we consider the deformation of a shell structure, where the reference surface is a part of a gyroid, see Figure 6.2. An approximation of a gyroid is given by the

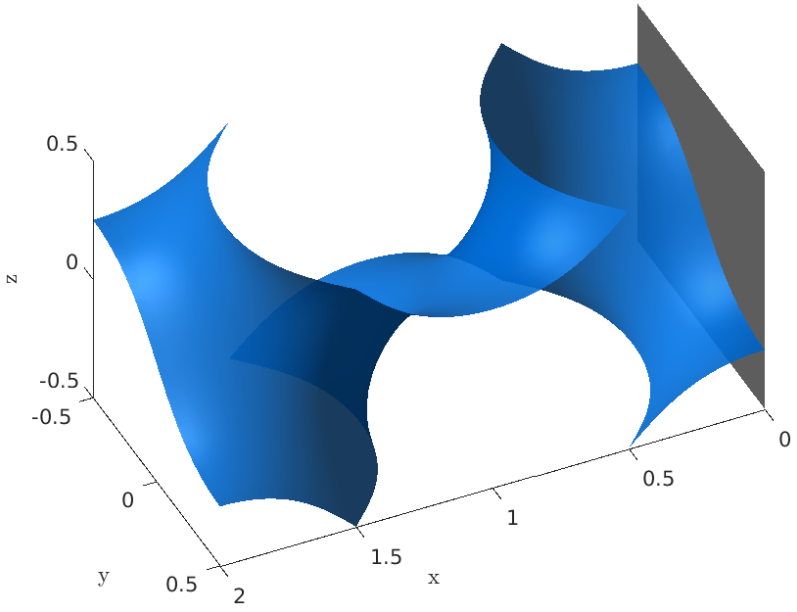

Figure 6.2: Geometry of the gyroid problem

level-set function

$$\phi(x,y,z) = \sin(x)\cos(y) + \sin(y)\cos(z) + \sin(z)\cos(x). \tag{6.3}$$

The considered shell lies in $B = [0\,\mathrm{m}, 2\,\mathrm{m}] \times [-0.5\,\mathrm{m}, 0.5\,\mathrm{m}] \times [-0.5\,\mathrm{m}, 0.5\,\mathrm{m}]$. The shell structure is fixed at the plane $x = 0\,\mathrm{m}$. We assume a thickness $t = 0.03\,\mathrm{m}$.

We investigate the static and dynamic responses. For the static analysis, we study the static deformation due to a volume load $\mathbf{b} = \mathbf{e}_z\, 10^7\,\mathrm{N/m^3}$. To this end, we use three different surface meshes, which are depicted in Figure 6.3. The coarsest mesh is obtained by the Marching Cubes Algorithm [112] and mesh smoothing. The other two meshes are

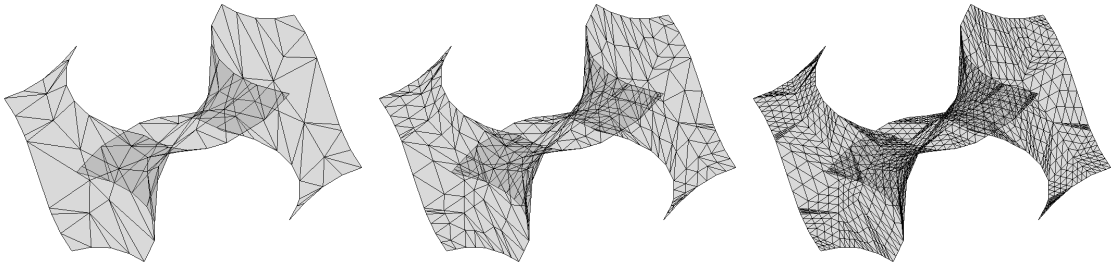

136 elements 544 elements 2176 elements

Figure 6.3: Three triangulations of the considered gyroid surface

obtained by uniform refinement of the coarsest mesh. We remark that in the analysis, each mesh is mapped to the exact surface by means of (4.39). In Table 6.2 and Figure 6.4, the convergence of the vertical displacement u_z at the point $[2\,\mathrm{m}, 0.5\,\mathrm{m}, -0.25\,\mathrm{m}]$ is studied. Obviously, the results obtained by linear ansatz functions underestimate the deformation tremendously for the considered meshes. The use of quadratic ansatz functions reduces the locking considerably. In view of the results obtained by the octic ansatz functions, we can accept a converged value of $u_z = 1.8812\,\mathrm{m}$. For the convergence plot in Figure 6.4, we have used the reference solution $u_{ref} = 1.8812370\,\mathrm{m}$. Again, the locking is clearly visible for the low order methods. However, for the methods $p \geq 4$ the expected exponential convergence is indicated.

Number of elements	136	544	2176
Linear	0.0118106	0.0332828	0.1055900
Quadratic	0.1694172	0.9005433	1.7152640
Cubic	1.2274694	1.8430397	1.8793713
Quartic	1.7745119	1.8788403	1.8808718
Quintic	1.8726206	1.8804255	1.8811317
Sextic	1.8784737	1.8809134	1.8812070
Septic	1.8802114	1.8811026	1.8812299
Octic	1.8807253	1.8811810	1.8812370

Table 6.2: Vertical displacement u_z at the point $[2\,\mathrm{m}, 0.5\,\mathrm{m}, -0.25\,\mathrm{m}]$

To characterize the dynamic behavior, we compute the eigenfrequencies of the structure. In Table 6.3, the convergence of the first ten eigenfrequencies of the considered gyroid are investigated. Here, octic shape functions were used. The results for all ten eigenfrequencies are very accurate already for the coarsest mesh. We remark that the eigenfrequencies are complex-valued due to the use of complex-valued material parameters modelling structural dissipation.

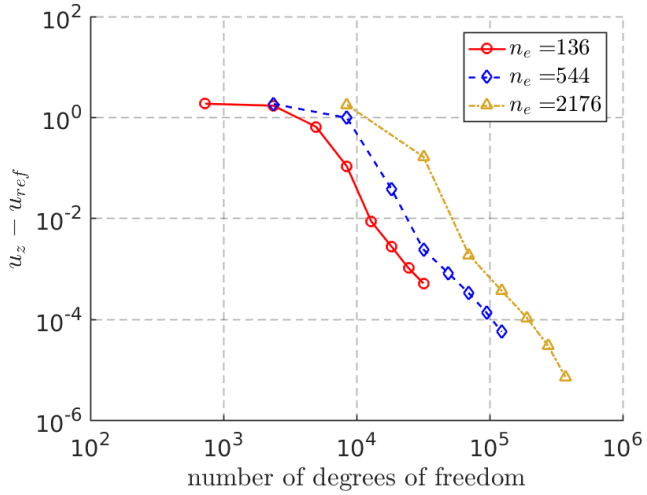

Figure 6.4: Error in the vertical displacement u_z at the point $[2\,\mathrm{m}, 0.5\,\mathrm{m}, -0.25\,\mathrm{m}]$

Number of elements	134	544	2176
1	5.8098+0.0290i	5.8094+0.0290i	5.8094+0.0290i
2	9.8908+0.0495i	9.8899+0.0494i	9.8898+0.0494i
3	23.7535+0.1188i	23.7514+0.1188i	23.7512+0.1188i
4	31.0186+0.1551i	31.0162+0.1551i	31.0160+0.1551i
5	56.3179+0.2816i	56.3132+0.2816i	56.3127+0.2816i
6	70.3201+0.3516i	70.3143+0.3516i	70.3137+0.3516i
7	86.3201+0.4316i	86.3127+0.4316i	86.3119+0.4315i
8	121.5068+0.6075i	121.4959+0.6075i	121.4948+0.6075i
9	133.4942+0.6675i	133.4781+0.6674i	133.4765+0.6674i
10	147.3079+0.7365i	147.2675+0.7363i	147.2631+0.7363i

Table 6.3: First ten eigenfrequencies of the gyroid, octic shape functions used

6.2 Method of Fundamental Solutions

6.2.1 Interior acoustics

We study the acoustic field inside a bounded domain, which is defined by the so-called orthocircle surface. This surface is given as the zero-level of the function

$$\begin{aligned}\phi(x,y,z) = ((x^2+y^2-1)^2+z^2)((y^2+z^2-1)^2+x^2)((z^2+x^2-1)^2+y^2) \\ -0.075^2(1+3(x^2+y^2+z^2)).\end{aligned} \tag{6.4}$$

The cavity of interest is given as $\{(x,y,z)|\phi(x,y,z)<0\}\cap\Omega_+$ and filled with air (material parameters shown in Table A.1). We assume that the whole boundary of the problem domain is sound hard. The problem setting is depicted in Figure 6.5. We place an acoustic

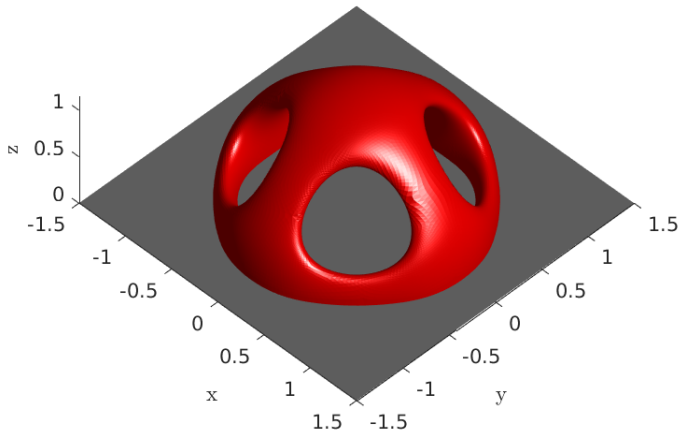

(a) View from above

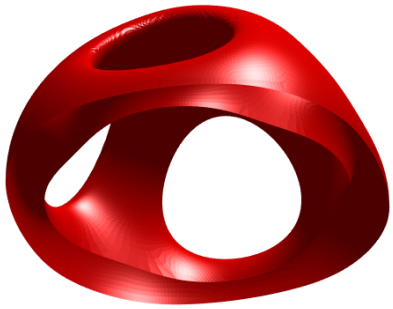

(b) View from below, bottom surface not shown

Figure 6.5: Geometry of the orthocircle problem

source with unit strength at the point $[-0.85\,\mathrm{m}, 0\,\mathrm{m}, 0.5\,\mathrm{m}]$. The excitation has a frequency $f = 1000\,\mathrm{Hz}$. Due to the fact that no dissipation occurs, the solution has to be real-valued. However, the approximation by means of the MFS yields a complex-valued solution. We use the imaginary part of the solution for the sake of solution verification. The imaginary part of the solution for different number of MFS sources n_s is depicted in Figure 6.6. For $n_s = 313$ and $n_s = 1202$, the imaginary part of the solution has the same order of magnitude as the real part of the solution. Thus, these results are not reliable. However, we observe the decreasing imaginary part of the solution, as more source points are used for the solution approximation. For $n_s = 9579$, the imaginary part of the solution is five order of magnitude lower than the real part of the solution. This indicates a practically accurate solution.

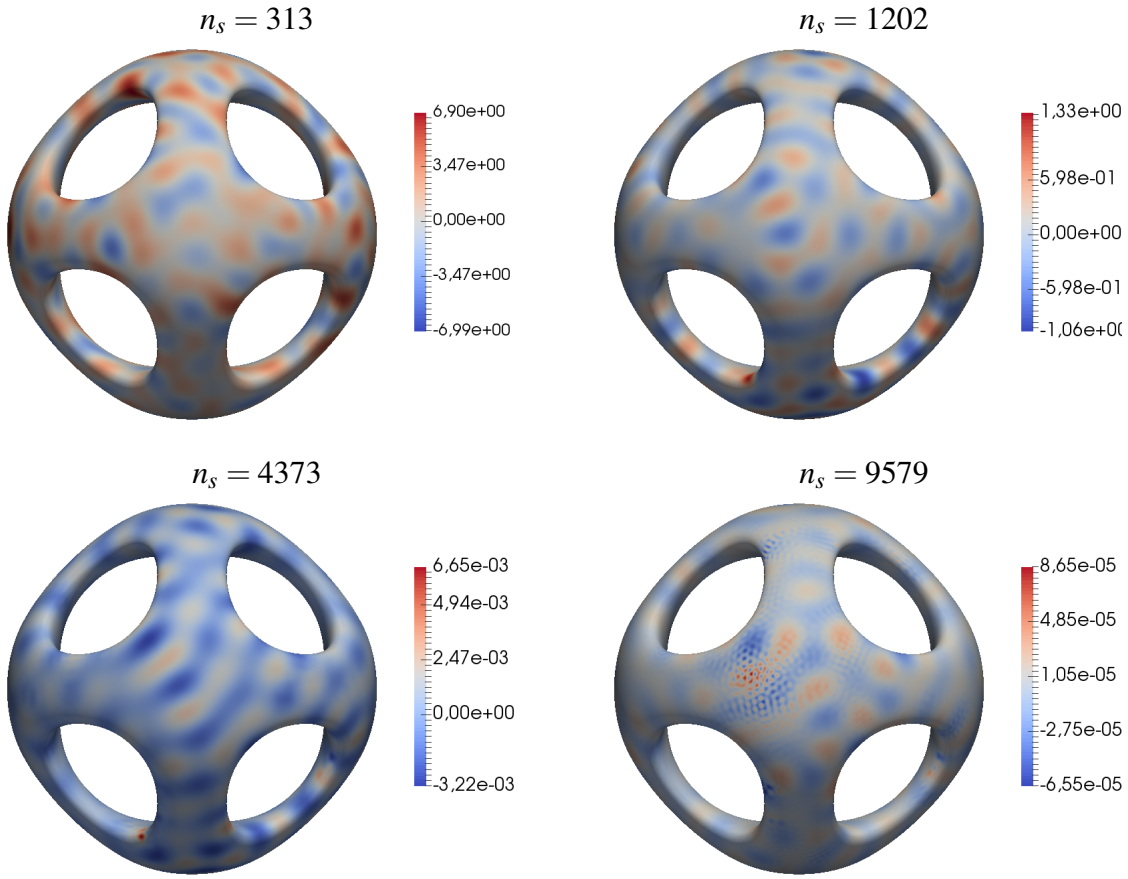

Figure 6.6: Imaginary part of the solution at the boundary for different number of source points n_s

The real part of the solution on the boundary is displayed in Figure 6.7 from different perspectives. Visually, no lack of symmetry in the solution is recognizable. The highest pressure on the boundary occurs near the excitation source point. For further reference, we state the results at three points in the interior in Table 6.4. Again, the convergence behavior of the results show the accuracy of the results obtained with $n_s = 9579$.

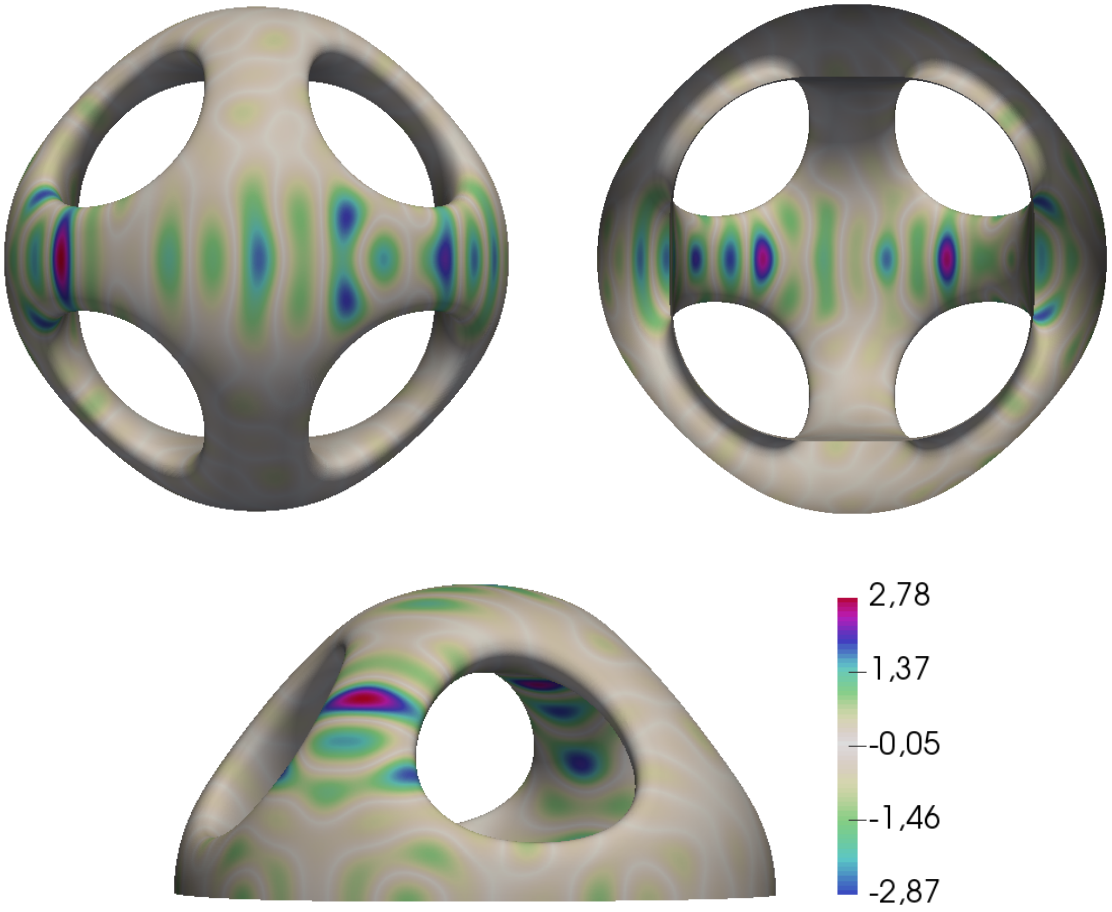

Figure 6.7: Real part of the pressure $[\mathrm{N/m^2}]$ at the boundary from different perspectives, $n_s = 9579$

Number of source points	313	1202	4373	9579
$[1\,\mathrm{m}, 0\,\mathrm{m}, 0.1\,\mathrm{m}]$	0.6350	0.3153	0.2523	0.2525
$[0\,\mathrm{m}, 0\,\mathrm{m}, 1\,\mathrm{m}]$	-0.3553	-0.0245	0.0191	0.0191
$[0\,\mathrm{m}, 1\,\mathrm{m}, 0.1\,\mathrm{m}]$	-0.1212	0.1567	0.2056	0.2056

Table 6.4: Real part of the pressure $[\mathrm{N/m^2}]$ at three points inside the orthocircle surface

6.2.2 Scattering at an assembly of spheres

In this example, the scattering at an assembly of sound hard spheres is studied. To this end, we assume a sound hard surface at $z = 0\,\mathrm{m}$. We place 18 spheres with unit radius regularly above this plane. The distance between the centers of the spheres is $3\,\mathrm{m}$. The centers of the lower nine spheres are on the plane at $z = 1.5\,\mathrm{m}$. We investigate the acoustic field due to a point source excitation with a frequency $f = 200\,\mathrm{Hz}$. The source is placed under the lower middle sphere at a $z = 0.25\,\mathrm{m}$. The situation is depicted in Figure 6.8.

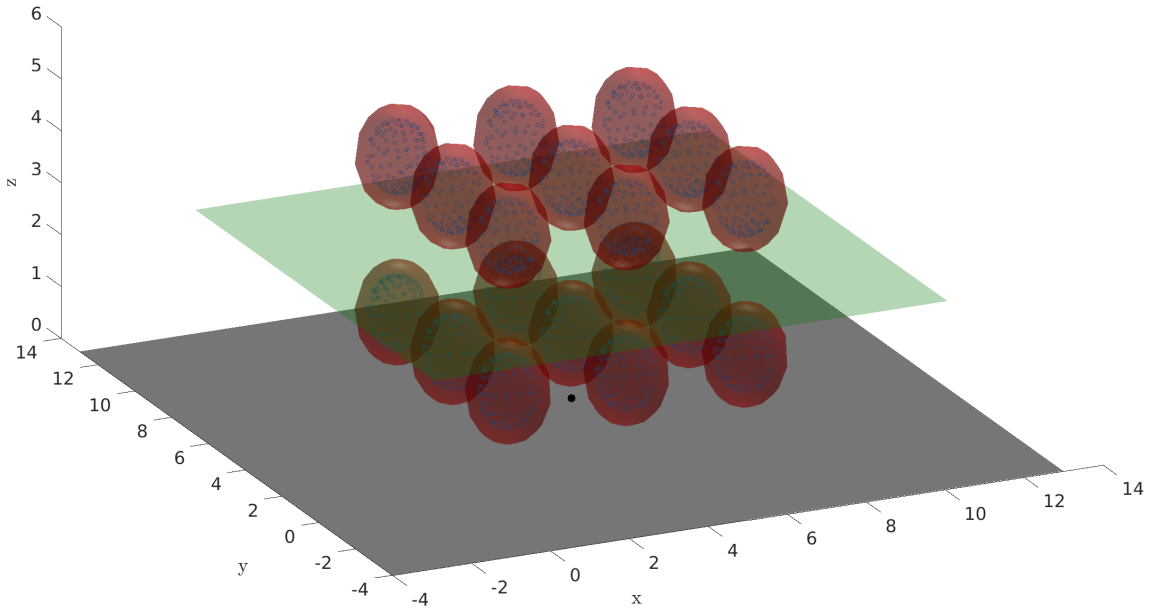

Figure 6.8: Assembly of spheres: Sound hard plane at $z = 0\,\mathrm{m}$ (gray), sound hard spheres (red), excitation source point (black), MFS source points (blue), evaluation plane (green)

We describe the spheres by the level-set function

$$\begin{aligned} f(\tau) &= \mathrm{mod}(\tau, 3) - \frac{3}{2}, \\ \phi(x,y,z) &= f(x)^2 + f(y)^2 + f(z)^2 - 1. \end{aligned} \tag{6.5}$$

For the problem at hand, we consider the zero level-set in $B = [0\,\mathrm{m}, 9\,\mathrm{m}] \times [0\,\mathrm{m}, 9\,\mathrm{m}] \times [0\,\mathrm{m}, 6\,\mathrm{m}]$. We remark that analogously to the description in [72] for the *norm* and comparison operators, the *modulo*-function has to evaluate on the real part of a hyper-dual number. The real part of the pressure distribution on the evaluation plane is plotted in Figure 6.9. Therein, we also considered the case in which no spheres are present. Due to the problem setup, the solution has to be symmetric. For the solutions obtained with 154 and

508 source points, the solutions are obviously not symmetric. However, for the solution with 1924 source points, virtually no lack of symmetry in the solution is visible.

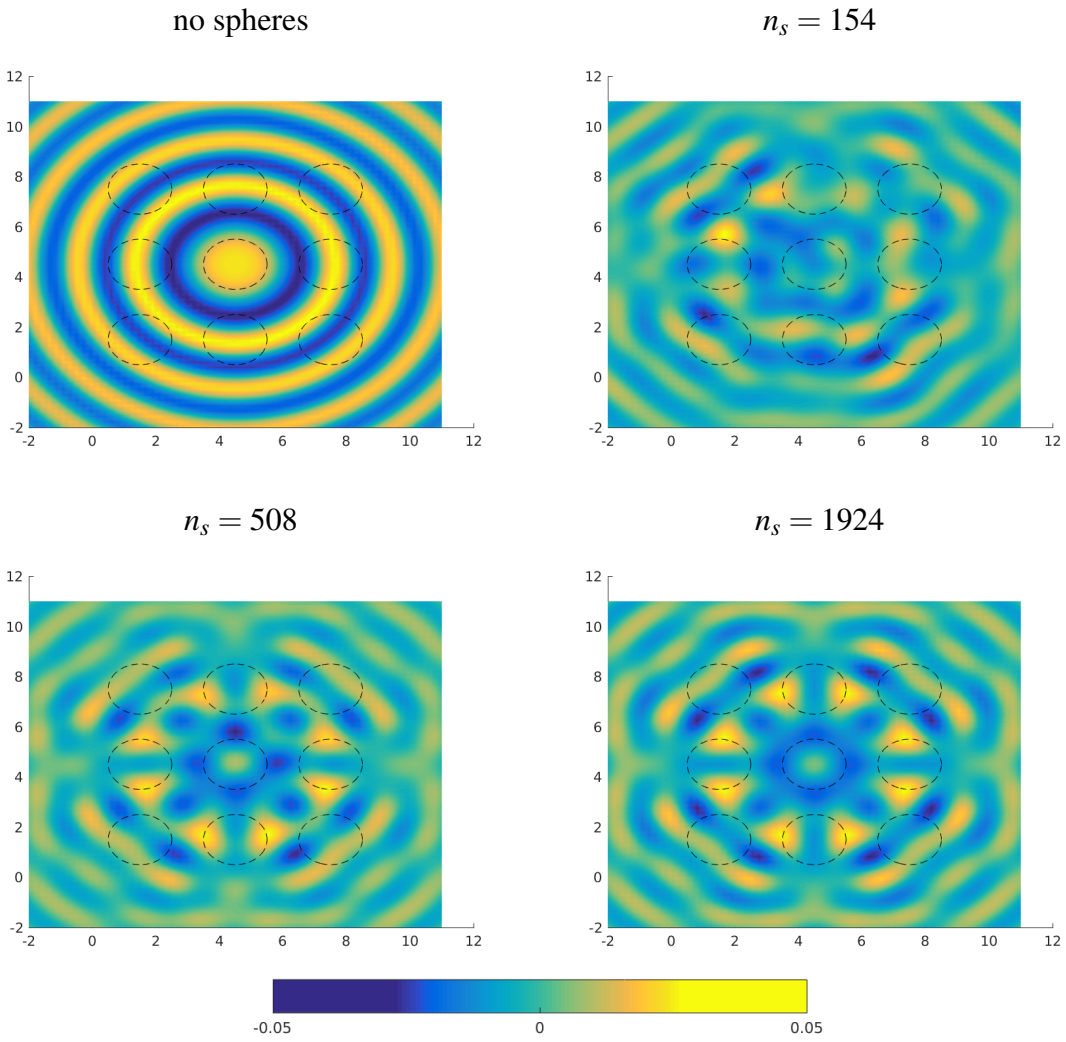

Figure 6.9: Real part of the pressure at the evaluation surface

6.3 Coupled Method

In this section, we apply the coupled MFS-FEM to two sound transmission problems through complex structures.

6.3.1 Deformed Sweep

In this example, we analyze a geometry which is given parametrically. We consider an ellipse which is moved along a circular path. Furthermore, the initial shape is deformed when moved. The initial ellipse lies in the $x-y$ plane with the center at $[0\,\mathrm{m}, 1\,\mathrm{m}, 0\,\mathrm{m}]$. The semi-major axis is $0.5\,\mathrm{m}$ in y direction, whereas the semi-major axis is $0.25\,\mathrm{m}$ in x direction. Finally, taking the deformation into account, the reference surface is parametrically given by

$$\begin{aligned} x &= \frac{\cos(2\pi\theta^2)}{4}\left(\cos\left(\pi^2 f(\theta^1)\right)-2\right), \\ y &= \frac{\cos(\pi f(\theta^1))}{4}(4+2\sin(2\pi\theta^2)-\sin(\pi f(\theta^1))\sin(2\pi\theta^2)), \\ z &= \frac{\sin(\pi f(\theta^1))}{4}(4+2\sin(2\pi\theta^2)-\sin(\pi f(\theta^1))\sin(2\pi\theta^2)). \end{aligned} \tag{6.6}$$

The parameter domain is $(\theta^1,\theta^2)\in[0,1]\times[0,1]$. We use the function κ defined in (6.2) with $b = 1/50$. In Figure 6.10, the geometry of the problem is visualized.

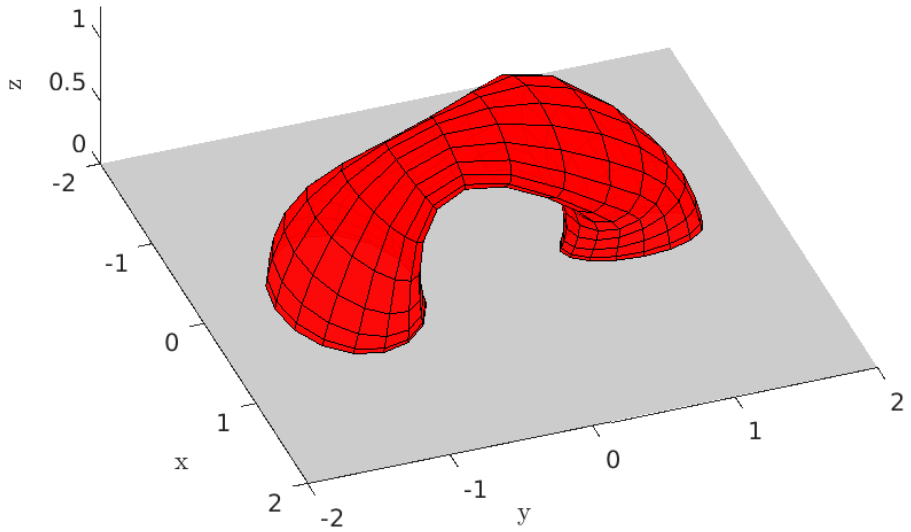

Figure 6.10: Geometry of the deformed sweep problem

The shell structure is composed of two layers. We assign the material parameters of aluminum (Table A.2) to the first layer, which has a thickness of 0.01 m. The second layer is a poroelastic polyurethane (Table A.3) layer with a thickness of 0.03 m. This poroelastic layer is in contact with the interior fluid.

For the sake of solution verification, we consider the uncoupled dynamic response of the shell structure as a result of a surface load $\mathbf{t} = -\mathbf{e}_z 10^3\,\mathrm{N/m^2}$ applied on the free surface of the aluminum layer. For the analysis at 250 frequencies in the range $[0\,\mathrm{Hz}, 500\,\mathrm{Hz}]$ we use sextic ansatz functions. The vertical displacements u_z at the point $(\theta^1, \theta^2) = (0.5, 0.25)$ are plotted over the frequency in Figure 6.11 for three meshes (each mesh has n_E elements). Due to these results, we will further use the 64-element mesh. In Figure 6.11, the displacement was plotted over the frequency range. For the better visualization, we have used the logarithmic measure

$$L_p(u) = 10 \log_{10}\left(\frac{u^2}{4 \cdot 10^{-10}}\right) \mathrm{dB}. \tag{6.7}$$

Next, the performance of the uncoupled MFS is studied. To this end, we calculate the interior pressure field due to a source with unit strength at the point $[0\,\mathrm{m}, -1\,\mathrm{m}, 0.5\,\mathrm{m}]$. The structure is assumed to be rigid in this case. The exact solution to this problem has to be real-valued. In Figure 6.12, the imaginary part of the solutions at the evaluation point $[0\,\mathrm{m}, 1\,\mathrm{m}, 0.5\,\mathrm{m}]$ obtained for a varying number of approximation source points are plotted. Based on this result, we proceed with 372 source points for the interior, as well as for the exterior fluid.

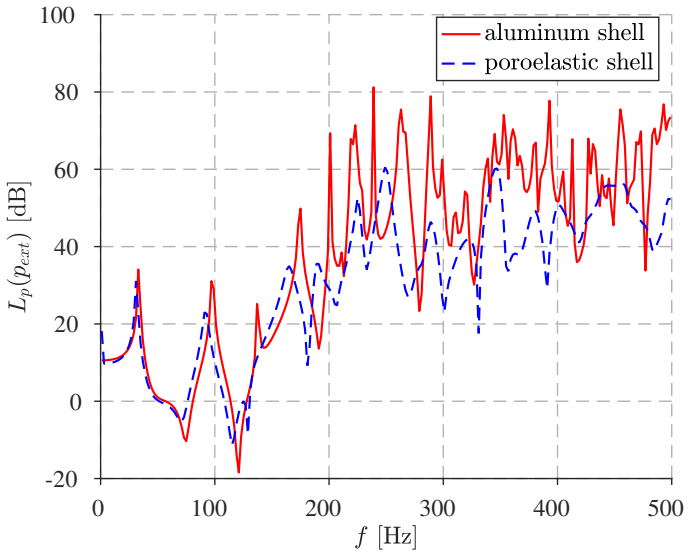

Figure 6.11: Deformed sweep problem: Vertical displacement u_z at point $(\theta^1, \theta^2) = (0.5, 0.25)$ of the uncoupled shell problem

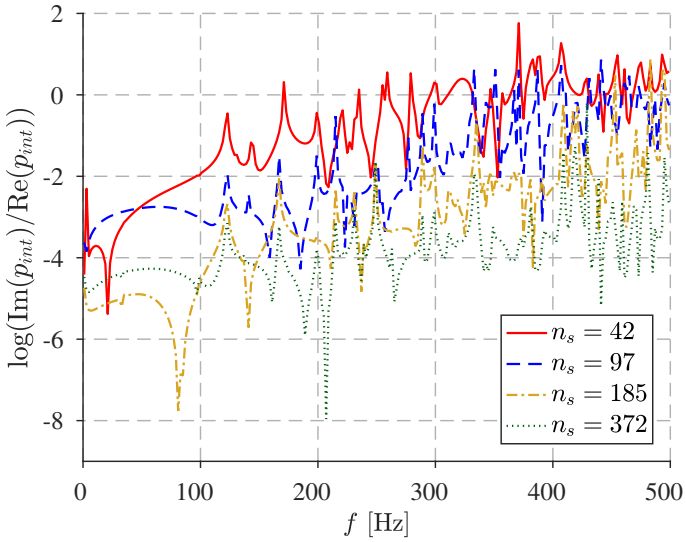

Figure 6.12: Deformed sweep problem: Imaginary part of the uncoupled MFS solution

With the discretization described above, we study the sound transmission from the interior to the exterior. Again, we consider a source at the point $[0\,\mathrm{m}, -1\,\mathrm{m}, 0.5\,\mathrm{m}]$ with unit strength for the excitation of the system. In Figure 6.13, the sound pressure level determined at the interior evaluation point $[0\,\mathrm{m}, 1\,\mathrm{m}, 0.5\,\mathrm{m}]$ is plotted. We compare the cases *uncoupled MFS* (rigid structure), *aluminum shell* (only the aluminum layer) and *poroelastic shell* (the aluminum layer with the polyurethane layer). The results for the cases *uncoupled MFS* and *aluminum shell* virtually agree. In the case of the *uncoupled MFS*, no dissipation occurs in the system and the solution is infinite at the eigenfrequencies. In the case of *aluminum shell* a small structural dissipation effect is present. This can be seen in Figure 6.13, where the eigenfrequencies are damped. However, we conclude that the compliance of the aluminum structure has only little influence on the interior sound pressure field. Nevertheless, the effects of the dissipation introduced by virtue of the poroelastic polyurethane layer are clearly visible. In particular, the calculated sound pressure levels are significantly reduced for frequencies above $f = 200\,\mathrm{Hz}$. The same conclusion is valid for the results at the exterior evaluation point $[0\,\mathrm{m}, 0\,\mathrm{m}, 1.5\,\mathrm{m}]$. The sound pressure level determined at the exterior evaluation point $[0\,\mathrm{m}, 0\,\mathrm{m}, 1.5\,\mathrm{m}]$ is plotted over the frequency in Figure 6.14. In the case of an rigid structure no transmission can occur. Therefore, this case is not considered in Figure 6.14. Again, the sound pressure level is significantly reduced in the case *poroelastic shell* compared to the case *aluminum shell*.

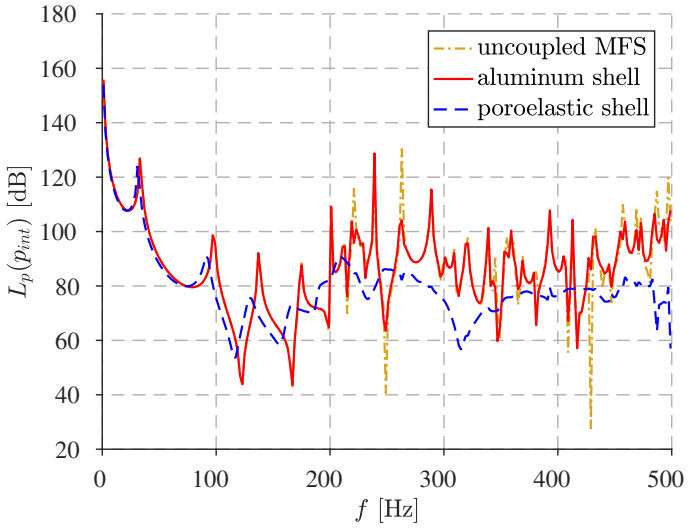

Figure 6.13: Deformed sweep problem: Comparison of the sound pressure level at the interior evaluation point for elastic and poroelastic shell

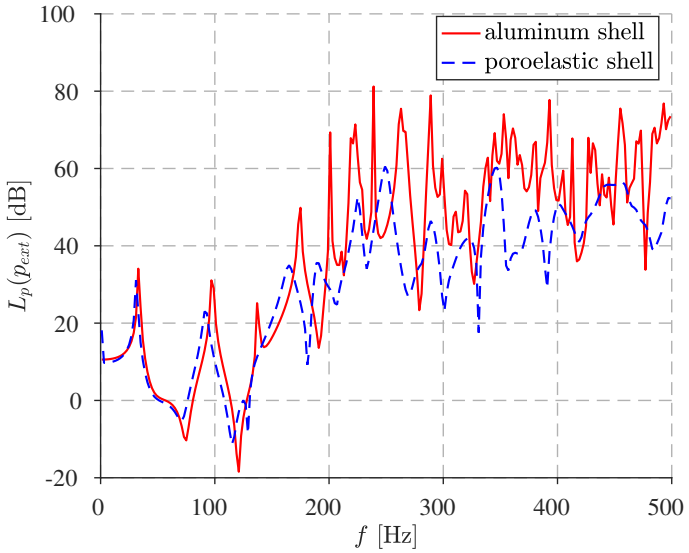

Figure 6.14: Deformed sweep problem: Comparison of the sound pressure level at the exterior evaluation point for elastic and poroelastic shell

6.3.2 Sound transmission through an implicitly given shell

In this section, we consider the sound transmission through a shell structure described by an implicitly given reference surface. The corresponding level-set function is

$$\phi(x,y,z) = (2x)^4 + (2y)^2 + (2z)^2 - 0.25. \tag{6.8}$$

The geometry of the problem is depicted in Figure 6.15. The shell structure is composed of

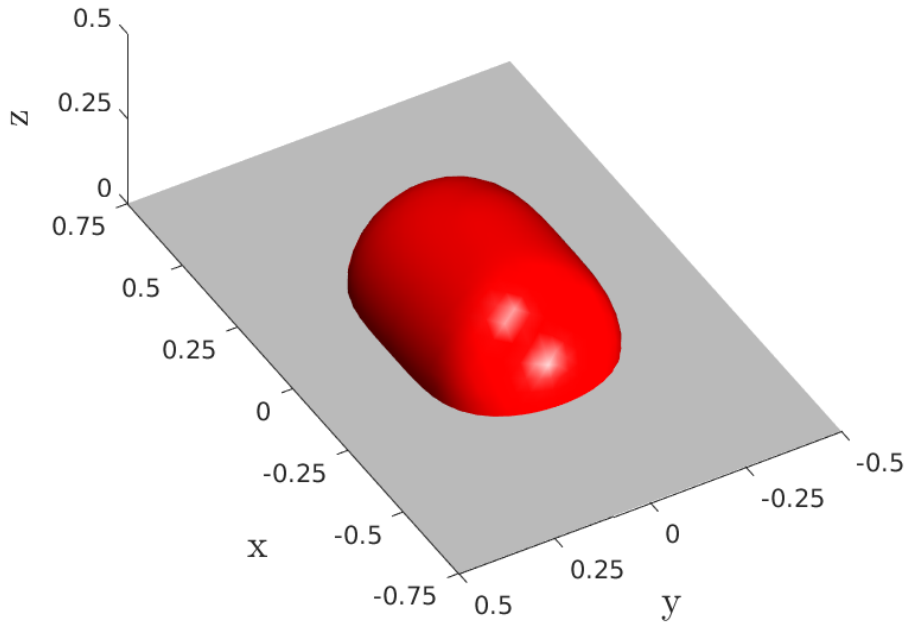

Figure 6.15: Geometry of the implicitly given shell

an aluminum (Table A.2) and a poroelastic polyurethane layer (Table A.3). The aluminum layer has a the thickness $t = 0.002\,\mathrm{m}$, whereas the polyurethane layer has a thickness $t = 0.01\,\mathrm{m}$. The poroelastic layer is in contact with the interior fluid.

We use octic shape functions constructed on a 64-element mesh for the discretization of the parameters in the shell model. For the discretization of the interior and exterior fluid pressure fields, we use 145 MFS source points each. The sound pressure level at the interior evaluation point $[0\,\mathrm{m}, 0\,\mathrm{m}, 0.1\,\mathrm{m}]$ due to a source at the point $[-0.25\,\mathrm{m}, -0.05\,\mathrm{m}, 0.1\,\mathrm{m}]$ with unit strength is plotted in Figure 6.16. Therein, the case of a rigid structure (uncoupled MFS), an aluminum shell and the full poroelastic structure is considered. We conclude that the compliance of the aluminum structure has only little influence on the interior sound pressure field. However, the effects of the dissipation introduced by virtue of the poroelastic layer are visible. The same conclusion is valid for the results at the exterior evaluation point $[0\,\mathrm{m}, 0\,\mathrm{m}, 0.3\,\mathrm{m}]$.

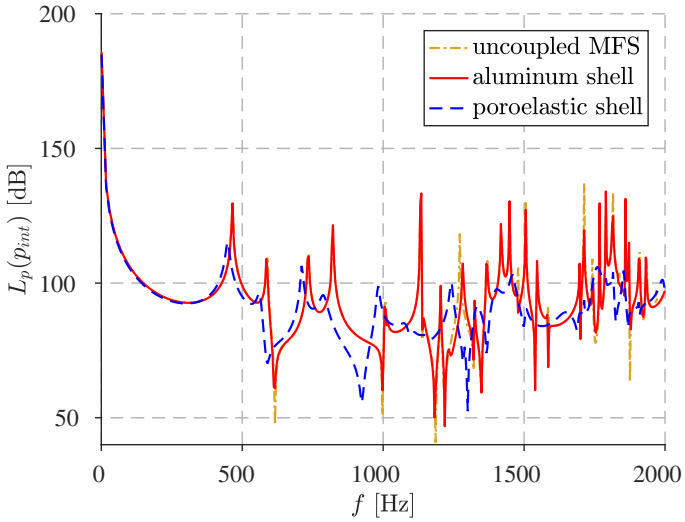

Figure 6.16: Comparison of the sound pressure level at the interior evaluation point for the aluminium and the poroelastic shell

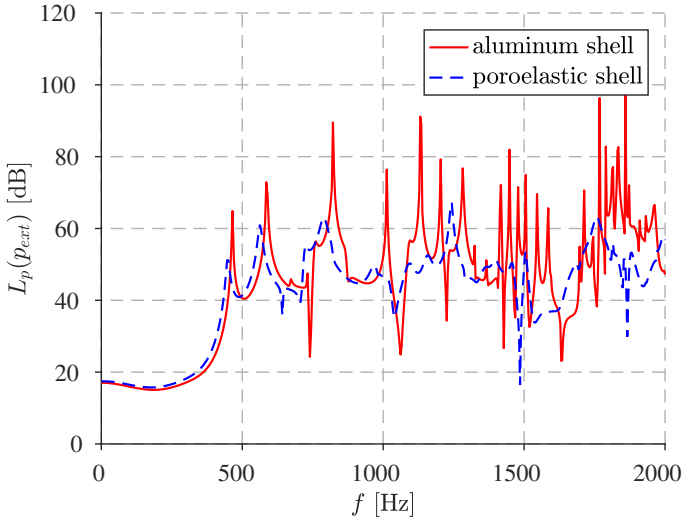

Figure 6.17: Comparison of the sound pressure level at the exterior evaluation point for the aluminium and the poroelastic shell

7 CONCLUSION

This work is concerned with the development of new simulation methods for vibro-acoustic analysis. In particular, we have treated the simulation of poroelastic shell structures and their interaction with the surrounding fluid.

The use of exact geometry descriptions for surfaces play a central role in this thesis. We developed a Finite Element Method (FEM) which is based on the exact geometry given by either a parametric or an implicit representation of the reference surface. In the case of a given parametrization, the evaluation of the quantities from differential geometry are done with respect to this parametrization and not with respect to a superfluous geometry discretization. In the case of an implicitly defined surface, the exact parametrization is constructed by means of the level-set function. Within the presented FEM, the derivatives of the parametrization up to the second order are required. We make use of a hyper-dual number concept. This technique allows to compute the derivatives up to the second order without loss in accuracy. In the present work, we treated the cases of surfaces given by a single parametrization or a single level-set function only. This limits the applicability of the developed methods when it comes to real life problems. Thus, an extension to complex, trimmed multi-patch parametrizations, as well as the ability to handle multiple level set functions is of interest in future research work.

The present work focuses on the vibro-acoustic analysis. Thus, the phenomena of interest are oscillations with small amplitude around an equilibrium state. Therefore, it is reasonable to linearize the nonlinear governing equations with respect to the equilibrium state. Hence, we model fluid domains with an acoustic fluid, elastic materials with the linearized theory of elasticity, and poroelastic materials with the Biot theory. Furthermore, we assumed harmonic time dependency of the field variables leading to an analysis in frequency domain. In future work, it might be of interest to conduct the analysis in time domain or to consider non-linear system response.

We consider inhomogeneous shell structures which may consist of elastic and poroelastic layers. Thus, not only the material parameters can vary from layer to layer, but also the underlying physical model. In order to face this complicated situation, a layer-wise shell model has been developed. The through-the-thickness variation of the displacement field is described by a seven-parameter model, which is assumed in each layer. Previous results in the literature suggest that this model has the least number of parameters and is asymptotically correct without resorting to a reduced energy functional. The pressure field occurring only in the poroelastic layers is described with a quadratic expansion through-the-thickness. The coupling conditions between elastic and poroelastic layers require the

continuity of the displacement field. This is accounted for in the developed model. However, this description yields only a constant transverse shear distribution in each layer. Thus, only a global discontinuous distribution is taken into account. In future work, it might be of interest to formulate a displacement field such that a continuous transverse shear distribution is obtained in situations where an accurate description is necessary. In contrast with this situation, the layup may contain very thin but stiff layers, where the effects of transverse shear may be neglected. Then the displacement field in these layers may be described by a shear-rigid model using less parameters.

The unknown parameters arising in the shell model are discretized by high order hierarchical finite element functions. Due to the chosen shell model, standard finite element ansatz functions are applicable. The chosen geometry treatment extends the standard FEM naturally. We also made a suggestion how to deal with singular parametrizations. This is based on simple observations of the bilinear form arising from the Laplacian. For the support of this suggestion, an in-depth mathematical analysis will be necessary.

The fluid surrounding the shell structure is discretized by means of the Method of Fundamental Solutions (MFS). Thus, the fluid pressure field is approximated by fundamental solutions of the underlying Helmholtz equation. The source points are placed in the complement of the respective fluid domain. The strength of the sources for the field approximation are determined by a variational formulation. This has the advantage over a collocation schema that the need of collocation points is circumvented. Due to the use of fundamental solutions, the Sommerfeld radiation condition is exactly fulfilled when considering unbounded domains. In the present work we placed the source points by simply shifting a constant distance normal to the boundary. In future work a more sophisticated placement may be considered in order to improve the efficiency of the MFS.

In order to solve problems where strong interaction between the shell structure and the surrounding fluid occurs, a coupled method is developed. Therefore, the coupling at acoustic fluid - elastic solid interfaces, as well as the coupling at acoustic fluid - poroelastic solid interfaces is considered.

The implemented numerical methods are verified against solutions obtained from the Method of Manufactured Solutions. In this method, a distinct solution is chosen and the corresponding source terms and boundary conditions are derived from the chosen solution. For the developed shell FEM, this approach has been implemented in the curvilinear coordinates induced by the shell geometry. For the verification of the MFS, the prescribed solution is constructed by a fundamental solution. Thus, the FEM and the MFS could be verified with high rigor. The coupled method has been verified against radial symmetric problems. The reference solutions were obtained by solving these problems analytically.

The capabilities of the developed methods have been shown in geometrically complex examples. The uncoupled FEM was used to solve the Scordelis-Lo roof problem and to study a shell structure where the reference surface is a part of the gyroid surface. The uncoupled

MFS was used to simulate the interior acoustics of a cavity bounded by the orthocircle surface. Furthermore, it was utilized to solve an exterior problem. The acoustic scattering at an assembly of spheres was investigated. Finally, the coupled method was applied to solve two sound transmission problems through poroelastic shells. In the present work, we considered only few selected materials. In particular, we used the material parameters of air (acoustic fluid), aluminum (elastic solid) and a polyurethane foam (poroelastic solid). In future work the developed methods can be used to investigate the performance of more materials applied in geometrically complex vibro-acoustic applications.

A MATERIAL PARAMETER

The material parameters used in the numerical examples are summarized in the following tables.

bulk modulus $K[\mathrm{kN/m^2}]$	$1.01 \cdot 10^5$
density $\rho[\mathrm{kg/m^3}]$	1.205

Table A.1: Material parameter of air

Young's modulus $E[\mathrm{N/m^2}]$	$70 \cdot 10^9$
Poisson's ratio ν[-]	0.3
density $\rho[\mathrm{kg/m^3}]$	2700
loss factor η[-]	0.01

Table A.2: Material parameter of aluminum

Young's modulus $E[\mathrm{N/m^2}]$	$70 \cdot 10^3$
Poisson's ratio ν[-]	0.39
density $\rho[\mathrm{kg/m^3}]$	22.1
loss factor η[-]	0.265
porosity ϕ[-]	0.98
static flow resistivity $\sigma[\mathrm{kg/m^3s}]$	3750
tortuosity α_∞[-]	1.17
viscous length $\Lambda[\mu m]$	110
thermal length $\Lambda'[\mu m]$	742

Table A.3: Material parameter of a polyurethane foam [87]

B RADIAL SYMMETRIC SOLUTIONS

We derive radial symmetric solutions of two coupled problems. In both cases a spherical shell structure separates a bounded interior fluid domain from an unbounded exterior fluid domain. In particular, we consider the cases *acoustic fluid - elastic layer - acoustic fluid* and *acoustic fluid - poroelastic layer - acoustic fluid*. We employ the spherical coordinates (r, φ, γ). Thus,

$$\begin{aligned} x &= r\cos(\varphi)\cos(\gamma) \\ y &= r\sin(\varphi)\cos(\gamma) \\ z &= r\sin(\gamma). \end{aligned} \tag{B.1}$$

Acoustic fluid. The Helmholtz equation in spherical coordinates assuming radial symmetry ($p(r, \varphi, \gamma) = p(r)$) reads

$$k^2 p + \frac{\partial^2 p}{\partial r^2} + \frac{2}{r}\frac{\partial p}{\partial r} = 0. \tag{B.2}$$

By setting $r = \frac{x}{k}$, we obtain

$$x^2\frac{d^2y}{dx^2} + 2x\frac{dy}{dx} + [x^2 - n(n+1)]y = 0 \tag{B.3}$$

with $n = 0$. The solutions for $n \in \mathbb{N}$ are the Spherical Bessel functions $j_n(x)$ and $y_n(x)$. For the case $n = 0$, they are

$$j_0(x) = \frac{\sin(x)}{x} \quad \text{and} \quad y_0(x) = \frac{-\cos(x)}{x}. \tag{B.4}$$

Thus, solutions of (B.2) are of the form

$$p(r) = a_1\, j_0(kr) + a_2\, y_0(kr), \tag{B.5}$$

where a_1, a_2 are constants, which have to be adapted to the respective problem. The radial displacement of the acoustic fluid is given by

$$u^a(r) = \frac{p_{,r}}{\omega^2 \rho^a}. \tag{B.6}$$

Elastodynamic. The equations of motion for a elastic solid in spherical coordinates assuming radial symmetry ($\mathbf{u}(r,\varphi,\gamma) = \mathbf{e}_r u(r)$) reduce to [1]

$$\frac{\partial \sigma_{rr}}{\partial r} + \frac{1}{r}(2\sigma_{rr} - \sigma_{\theta\theta} - \sigma_{\phi\phi}) = -\omega^2 \rho\, u_r. \tag{B.7}$$

The stress components are given by

$$\begin{aligned} \sigma_{rr} &= (\lambda + 2\mu)\frac{\partial u}{\partial r} + 2\lambda\frac{u}{r}, \\ \sigma_{\theta\theta} = \sigma_{\phi\phi} &= \lambda\frac{\partial u}{\partial r} + 2\lambda\frac{u}{r} + 2\mu\frac{u}{r}. \end{aligned} \tag{B.8}$$

Inserting (B.8) in (B.7) yields

$$\frac{\partial^2 u}{\partial r^2} + \frac{2}{r}\frac{\partial u}{\partial r} + \left(\frac{\omega^2}{c^2} - \frac{2}{r^2}\right) u = 0 \tag{B.9}$$

with $c = \sqrt{\frac{\lambda+2\mu}{\rho}}$. Multiplying with r^2 and $\Lambda^2 = \frac{\omega^2}{c^2}$ gives

$$r^2\frac{\partial^2 u}{\partial r^2} + 2r\frac{\partial u}{\partial r} + \left(\Lambda^2 r^2 - 2\right) u = 0. \tag{B.10}$$

By setting $r = \frac{x}{\Lambda}$, we obtain

$$x^2\frac{\partial^2 u}{\partial x^2} + 2x\frac{\partial u}{\partial x} + \left(x^2 - 2\right) u = 0, \tag{B.11}$$

which is in accordance with (B.3) for $n = 1$. Therefore, the solutions are

$$j_1(x) = \frac{\sin(x)}{x^2} - \frac{\cos(x)}{x} \quad , \quad y_1(x) = -\frac{\cos(x)}{x^2} - \frac{\sin(x)}{x}. \tag{B.12}$$

Thus, the radial symmetric displacement field is of the form

$$u^e(r) = b_1\, j_1(kr) + b_2\, y_1(kr), \tag{B.13}$$

with the two constants b_1 and b_2.

Poroelasticity. For the derivation of the poroelastic spherical radial symmetric solution, we follow [133]. The governing equations are

$$M\frac{\partial}{\partial r}\left(\frac{1}{r^2}\frac{\partial}{\partial r}\left(r^2 u\right)\right) - (\alpha + \beta)\frac{\partial p}{\partial r} + \omega^2(\rho + \beta\rho_f)\, u = 0 \tag{B.14}$$

and

$$-\frac{\beta}{\omega^2\rho_f}\Delta p+(\beta+\alpha)\,\nabla\cdot u+\frac{\phi^2}{R}p=0. \tag{B.15}$$

Defining the displacement potential $u=\frac{\partial\Phi}{\partial r}$ leads to

$$\frac{\partial}{\partial r}\left[M\left(\frac{1}{r^2}\frac{\partial}{\partial r}\left(r^2\frac{\partial\Phi}{\partial r}\right)\right)-(\alpha+\beta)\,p+\omega^2(\rho+\beta\rho_f)\,\Phi\right]=0 \tag{B.16}$$

Furthermore, we set $\Phi=\frac{\xi}{r}$ and $p=\frac{\chi}{r}$ to obtain

$$\begin{aligned}\xi_{,rr}-\frac{\alpha+\beta}{M}\chi+\frac{\omega^2(\rho+\beta\rho_f)}{M}\xi=0,\\ \frac{\beta}{\omega^2\rho_f}\chi_{,rr}+(\alpha+\beta)\,\xi_{,rr}+\frac{\phi^2}{R}\chi=0.\end{aligned} \tag{B.17}$$

The ansatz

$$\begin{aligned}\xi=\xi_i\,\mathrm{e}^{\omega\Lambda_i r},\\ \chi=\chi_i\,\mathrm{e}^{\omega\Lambda_i r}\end{aligned} \tag{B.18}$$

leads to the system of equations

$$\begin{bmatrix}\omega^2(\Lambda^2+\frac{\rho+\beta\rho_f}{M}) & \frac{(\alpha+\beta)}{M}\\ \omega^2\Lambda^2(\alpha+\beta) & \frac{\beta\Lambda^2}{\rho_f}+\frac{\phi^2}{R}\end{bmatrix}\begin{bmatrix}\xi_i\\ \chi_i\end{bmatrix}=\begin{bmatrix}0\\0\end{bmatrix}. \tag{B.19}$$

The four roots of the characteristic equation are found to be

$$\begin{aligned}\Lambda_1=-\Lambda_2=\frac{\sqrt{-A+\sqrt{A^2-4B}}}{\sqrt{2}},\\ \Lambda_3=-\Lambda_4=\frac{\sqrt{-A-\sqrt{A^2-4B}}}{\sqrt{2}},\end{aligned} \tag{B.20}$$

where

$$\begin{aligned}A=-\frac{\rho_f\phi^2}{\beta R}-\frac{\rho_f(\alpha+\beta)^2}{\beta M}+\frac{\rho+\beta\rho_f}{M},\\ B=-\frac{\rho_f\phi^2(\rho+\beta\rho_f)}{\beta MR}.\end{aligned} \tag{B.21}$$

Furthermore, $\chi_i = -\frac{\omega^2}{\alpha+\beta}(\lambda_i^2 M + \rho + \beta\rho_f)\xi_i$. Thus, the homogeneous solution has the form

$$\begin{aligned} u(r) &= \sum_{i=1}^{4} \xi_i \left(\omega\lambda_i - \frac{1}{r}\right) \frac{\mathrm{e}^{\omega\lambda_i r}}{r}, \\ p(r) &= \sum_{i=1}^{4} -\frac{\omega^2}{\alpha+\beta}(\lambda_i^2 M + \rho + \beta\rho_f)\xi_i \frac{\mathrm{e}^{\omega\lambda_i r}}{r}. \end{aligned} \tag{B.22}$$

Here, we have four constants ξ_i, which have to be determined. We remark that the total radial stress is given by

$$\sigma_{rr}^{\mathrm{tot}}(r) = (\lambda + 2\mu)\frac{\partial u(r)}{\partial r} + 2\lambda\frac{u(r)}{r} - \alpha p(r). \tag{B.23}$$

Coupled Solutions. The unknown coefficients introduced above can be determined, if the boundary and coupling conditions are taken into account. We state them for the two cases used in Chapter 5. These cases are the *acoustic fluid - elastic layer - acoustic fluid* and *acoustic fluid - poroelastic layer - acoustic fluid* problems. Thus, we have two acoustic fluid domains and two material interfaces in both domains. The pressure solutions of the interior domain and the exterior domain are denoted by p^{int} and p^{ext}, respectively. The material interfaces are located at the fixed radii r^{int} and r^{ext}. The excitation is given by an acoustic point source placed at the origin. Thus, we make the ansatz

$$p^{int} = \frac{\cos(kr)}{r} a^{int} + \frac{\mathrm{e}^{-\mathrm{i}kr}}{4\pi r}, \tag{B.24}$$

where we considered the non-singular part in (B.5). In order to fulfill the Sommerfeld radiation condition, we set $a_2 = -a_1 = a^{ext}$ in (B.5) and write

$$p^{ext} = \frac{\cos(kr) - \mathrm{i}\sin(kr)}{r}\, a^{ext}. \tag{B.25}$$

The interface conditions for the acoustic fluid - elastic solid interfaces are given by

$$\begin{aligned} p^{int}(r^{int}) &= \sigma_{rr}(r^{int}), \\ u^{int}(r^{int}) &= u^{e}(r^{int}), \\ p^{ext}(r^{ext}) &= \sigma_{rr}(r^{ext}), \\ u^{ext}(r^{ext}) &= u^{e}(r^{ext}). \end{aligned} \tag{B.26}$$

Therefore, the unknown constants a^{int}, a^{ext} and b_1, b_2 in (B.13) can be determined. The respective conditions for the acoustic fluid - poroelastic solid interfaces are

$$\begin{aligned} p^{int}(r^{int}) &= \sigma_{rr}^{\mathrm{tot}}(r^{int}), \\ p^{int}(r^{int}) &= p(r^{int}), \\ u^{int}(r^{int}) &= u^{p}(r^{int}), \\ p^{ext}(r^{ext}) &= \sigma_{rr}^{\mathrm{tot}}(r^{ext}), \\ p^{ext}(r^{ext}) &= p(r^{ext}), \\ u^{ext}(r^{ext}) &= u^{p}(r^{ext}). \end{aligned} \tag{B.27}$$

These conditions allow to uniquely determine the six coefficients a^{int}, a^{ext} and ξ_i in this case. We use the computer algebra system Mathematica [181] for this task.

REFERENCES

[1] Achenbach, J. *Wave propagation in elastic solids*, vol. 16. Elsevier, 2012.

[2] Acosta, G., and Monzón, G. Interpolation error estimates in $W^{1,p}$ for degenerate Q_1 isoparametric elements. *Numerische Mathematik 104*, 2 (2006), 129–150.

[3] Actis, R. L., Szabo, B. A., and Schwab, C. Hierarchic models for laminated plates and shells. *Computer Methods in Applied Mechanics and Engineering 172*, 1 (1999), 79–107.

[4] Ahmad, S., Irons, B. M., and Zienkiewicz, O. Analysis of thick and thin shell structures by curved finite elements. *International Journal for Numerical Methods in Engineering 2*, 3 (1970), 419–451.

[5] Allard, J., and Atalla, N. *Propagation of sound in porous media*, 2nd ed. John Wiley & Sons, 2009.

[6] Altenbach, H. *Kontinuumsmechanik: Einführung in die materialunabhängigen und materialabhängigen Gleichungen*. Springer, Berlin, 2012.

[7] Altenbach, J., Altenbach, H., and Eremeyev, V. A. On generalized Cosserat-type theories of plates and shells: A short review and bibliography. *Archive of Applied Mechanics 80*, 1 (2010), 73–92.

[8] Alves, C. J. On the choice of source points in the method of fundamental solutions. *Engineering analysis with boundary elements 33*, 12 (2009), 1348–1361.

[9] Amado-Mendes, P., Costa, P. A., Godinho, L. M., and Lopes, P. 2.5D MFS-FEM model for the prediction of vibrations due to underground railway traffic. *Engineering Structures 104* (2015), 141–154.

[10] Arciniega, R., and Reddy, J. Large deformation analysis of functionally graded shells. *International Journal of Solids and Structures 44*, 6 (2007), 2036–2052.

[11] Arciniega, R., and Reddy, J. Tensor-based finite element formulation for geometrically nonlinear analysis of shell structures. *Computer Methods in Applied Mechanics and Engineering 196*, 4 (2007), 1048–1073.

[12] Argyris, J., Fried, I., and Scharpf, D. The tuba family of plate elements for the matrix displacement method. *The Aeronautical Journal (1968) 72*, 692 (1968), 701–709.

[13] Arnold, D. N., Madureira, A. L., and Zhang, S. On the range of applicability of the Reissner-Mindlin and Kirchhoff-Love plate bending models. *Journal of Elasticity and the Physical Science of Solids 67*, 3 (2002), 171–185.

[14] Aubry, R., Karamete, B. K., Mestreau, E. L., and Dey, S. A three-dimensional parametric mesher with surface boundary-layer capability. *Journal of Computational Physics 270* (2014), 161–181.

[15] Augustin, M. A. *A method of fundamental solutions in poroelasticity to model the stress field in geothermal reservoirs*. PhD thesis, TU Kaiserslautern, Germany, 2015.

[16] Babuška, I., and Li, L. Hierarchic modeling of plates. *Computers & Structures 40*, 2 (1991), 419–430.

[17] Barnett, A., and Betcke, T. Stability and convergence of the method of fundamental solutions for Helmholtz problems on analytic domains. *Journal of Computational Physics 227*, 14 (2008), 7003–7026.

[18] Basar, Y., and Krätzig, W. B. *Mechanik der Flächentragwerke: Theorie, Berechnungsmethoden, Anwendungsbeispiele*. Vieweg, 1985.

[19] Benson, D., Bazilevs, Y., Hsu, M.-C., and Hughes, T. Isogeometric shell analysis: the Reissner-Mindlin shell. *Computer Methods in Applied Mechanics and Engineering 199*, 5 (2010), 276–289.

[20] Billade, N., and Vemaganti, K. Hierarchical models of thin elastic structures: Overview and recent advances in error estimation and adaptivity. *Computer Methods in Applied Mechanics and Engineering 196*, 37 (2007), 3508–3523.

[21] Biot, M. A. General theory of three-dimensional consolidation. *Journal of Applied Physics 12*, 2 (1941), 155–164.

[22] Biot, M. A. Theory of elasticity and consolidation for a porous anisotropic solid. *Journal of Applied Physics 26*, 2 (1955), 182–185.

[23] Biot, M. A. Theory of propagation of elastic waves in a fluid-saturated porous solid. I. Low-frequency range. *The Journal of the Acoustical Society of America 28* (1956), 168–178.

[24] Biot, M. A. Theory of propagation of elastic waves in a fluid-saturated porous solid. II. Higher frequency range. *The Journal of the Acoustical Society of America 28*, 2 (1956), 179–191.

[25] Bischoff, M. *Theorie und Numerik einer dreidimensionalen Schalenformulierung*. PhD thesis, Bericht Nr. 30, Institut für Baustatik, Universität Stuttgart, Germany, 1999.

[26] Bischoff, M., Bletzinger, K.-U., Wall, W., and Ramm, E. Models and finite elements for thin-walled structures. In *Encyclopedia of Computational Mechanics*, E. Stein, R. de Borst, and T. Hughes, Eds., vol. 2. Wiley Online Library, 2004, pp. 59–137.

[27] Bogner, F., Fox, R., and Schmit, L. The generation of inter-element-compatible stiffness and mass matrices by the use of interpolation formulas. In *Proceedings of the Conference on Matrix Methods in Structural Mechanics* (Wright-Patterson Air Force Base, Ohio, October 1965).

[28] Bowen, R. M. Theory of Mixtures. In *Continuum Physics*, A. C. Eringen, Ed. Academic Press, 1976, pp. 1–127.

[29] Bowen, R. M. Incompressible porous media models by use of the theory of mixtures. *International Journal of Engineering Science 18*, 9 (1980), 1129–1148.

[30] Bowen, R. M. Compressible porous media models by use of the theory of mixtures. *International Journal of Engineering Science 20*, 6 (1982), 697–735.

[31] Braess, D. *Finite elements: Theory, fast solvers, and applications in solid mechanics*. Cambridge University Press, 2007.

[32] Brenner, S., and Scott, R. *The mathematical theory of finite element methods*, vol. 15. Springer Science & Business Media, 2007.

[33] Buechter, N., and Ramm, E. Shell theory versus degeneration- a comparison in large rotation finite element analysis. *International Journal for Numerical Methods in Engineering 34*, 1 (1992), 39–59.

[34] Burger, M. Finite element approximation of elliptic partial differential equations on implicit surfaces. *Computing and Visualization in Science 12*, 3 (2009), 87–100.

[35] Burman, E., Claus, S., Hansbo, P., Larson, M. G., and Massing, A. CutFEM: Discretizing geometry and partial differential equations. *International Journal for Numerical Methods in Engineering 104*, 7 (2015), 472–501.

[36] Caliri, M. F., Ferreira, A. J., and Tita, V. A review on plate and shell theories for laminated and sandwich structures highlighting the finite element method. *Composite Structures 156* (2016), 63–77.

[37] Carrera, E. Theories and finite elements for multilayered, anisotropic, composite plates and shells. *Archives of Computational Methods in Engineering 9*, 2 (2002), 87–140.

[38] Carrera, E. Historical review of zig-zag theories for multilayered plates and shells. *Applied Mechanics Reviews 56*, 3 (2003), 287–308.

[39] Champoux, Y., and Allard, J.-F. Dynamic tortuosity and bulk modulus in air-saturated porous media. *Journal of Applied Physics 70*, 4 (1991), 1975–1979.

[40] Chapelle, D., and Bathe, K.-J. *The finite element analysis of shells*. Springer Science & Business Media, 2010.

[41] Chen, C., Cho, H. A., and Golberg, M. Some comments on the ill-conditioning of the method of fundamental solutions. *Engineering Analysis with Boundary Elements 30*, 5 (2006), 405–410.

[42] Chen, C., Karageorghis, A., and Li, Y. On choosing the location of the sources in the mfs. *Numerical Algorithms* (2015), 1–24. printed 3.5.2016.

[43] Cho, M., and Roh, H. Y. Development of geometrically exact new shell elements based on general curvilinear co-ordinates. *International Journal for Numerical Methods in Engineering 56*, 1 (2003), 81–115.

[44] Christensen, R. *Theory of viscoelasticity: An introduction*. Elsevier, 2012.

[45] Ciarlet, P. G. *The finite element method for elliptic problems*. North-Holland, Amsterdam, 1978.

[46] Ciarlet, P. G. *An Introduction to Differential Geometry with Applications to Elasticity*, vol. 78. Springer, 2006.

[47] Ciarlet, P. G., and Lods, V. Asymptotic analysis of linearly elastic shells. I. Justification of membrane shell equations. *Archive for Rational Mechanics and Analysis 136*, 2 (1996), 119–161.

[48] Ciarlet, P. G., and Lods, V. Asymptotic analysis of linearly elastic shells. III. Justification of Koiter's shell equations. *Archive for Rational Mechanics and Analysis 136*, 2 (1996), 191–200.

[49] Ciarlet, P. G., and Lods, V. Asymptotic analysis of linearly elastic shells:'Generalized membrane shells'. *Journal of Elasticity 43*, 2 (1996), 147–188.

[50] Ciarlet, P. G., Lods, V., and Miara, B. Asymptotic analysis of linearly elastic shells. II. Justification of flexural shell equations. *Archive for Rational Mechanics and Analysis 136*, 2 (1996), 163–190.

[51] Cirak, F., Ortiz, M., and Schroder, P. Subdivision surfaces: A new paradigm for thin-shell finite-element analysis. *International Journal for Numerical Methods in Engineering 47*, 12 (2000), 2039–2072.

[52] Cockburn, B., and Demlow, A. Hybridizable discontinuous Galerkin and mixed finite element methods for elliptic problems on surfaces. *Mathematics of Computation 85* (2016), 2609–2638.

[53] Cosserat, E., and Cosserat, F. Sur la théorie de l'élasticité. premier mémoire. *Annales de la Faculté des sciences de Toulouse : Mathématiques 10*, 3-4 (1896), I1–I116.

[54] Cosserat, E., and Cosserat, F. *Théorie des corps déformables*. Hermann net Fils, Paris, 1909.

[55] Courant, R. Variational methods for the solution of problems of equilibrium and vibrations. *Bulletin of the American Mathematical Society 49*, 1 (1943), 1–23.

[56] Dauge, M., Faou, E., and Yosibash, Z. Plates and shells: Asymptotic expansions and hierarchic models. *Encyclopedia of Computational Mechanics* (2004).

[57] De Araújo, B. R., Lopes, D. S., Jepp, P., Jorge, J. A., and Wyvill, B. A survey on implicit surface polygonization. *ACM Computing Surveys (CSUR) 47*, 4 (2015), 60.

[58] De Boer, R. *Theory of porous media: Highlights in historical development and current state*. Springer Science & Business Media, 2012.

[59] Deckers, E., Atak, O., Coox, L., D'Amico, R., Devriendt, H., Jonckheere, S., Koo, K., Pluymers, B., Vandepitte, D., and Desmet, W. The wave based method: An overview of 15 years of research. *Wave Motion 51*, 4 (2014), 550–565.

[60] Deckers, E., Jonckheere, S., Vandepitte, D., and Desmet, W. Modelling techniques for vibro-acoustic dynamics of poroelastic materials. *Archives of Computational Methods in Engineering 22*, 2 (2015), 183–236.

[61] Demlow, A. Higher-order finite element methods and pointwise error estimates for elliptic problems on surfaces. *SIAM Journal on Numerical Analysis 47*, 2 (2009), 805–827.

[62] Desmet, W. *A wave based prediction technique for coupled vibro-acoustic analysis*. PhD thesis, Katholieke Universiteit Leuven, Belgique, 1998.

[63] Detournay, E., and Cheng, A. H.-D. Fundamentals of poroelasticity. In *Comprehensive Rock Engineering: Principles, Practice and Projects, Analysis and Design Methods*, C. Fairhurst, Ed., vol. 2. 1993, pp. 113–171.

[64] Düster, A., Bröker, H., and Rank, E. The p-version of the finite element method for three-dimensional curved thin walled structures. *International Journal for Numerical Methods in Engineering 52*, 7 (2001), 673–703.

[65] Dziuk, G. Finite elements for the Beltrami operator on arbitrary surfaces. In *Partial Differential Equations and Calculus of Variations*, S. Hildebrandt and R. Leis, Eds., vol. 1357. Springer, 1988, pp. 142–155.

[66] Dziuk, G., and Elliott, C. M. Finite element methods for surface PDEs. *Acta Numerica 22* (2013), 289–396.

[67] Eça, L., Hoekstra, M., Hay, A., and Pelletier, D. Verification of RANS solvers with manufactured solutions. *Engineering with Computers 23*, 4 (2007), 253–270.

[68] Echter, R., Oesterle, B., and Bischoff, M. A hierarchic family of isogeometric shell finite elements. *Computer Methods in Applied Mechanics and Engineering 254* (2013), 170–180.

[69] Ehlers, W. Foundations of multiphasic and porous materials. In *Porous Media*. Springer, 2002, pp. 3–86.

[70] Eringen, A. C., and Suhubi, E. S. *Elastodynamics*, vol. II. Academic Press, 1975.

[71] Fairweather, G., Karageorghis, A., and Martin, P. A. The method of fundamental solutions for scattering and radiation problems. *Engineering Analysis with Boundary Elements 27*, 7 (2003), 759–769.

[72] Fike, J. A., and Alonso, J. J. The development of hyper-dual numbers for exact second-derivative calculations. In *49th AIAA Aerospace Sciences Meeting including the New Horizons Forum and Aerospace Exposition* (Orlando, Florida, 4-7 January 2011).

[73] Fisch, R. *Code Verification of Partitioned FSI Environments for Lightweight Structures*, vol. 23 of *Schriftenreihe des Lehrstuhls für Statik der Technischen Universität München*. Lehrstuhl für Statik, Technische Universität München, 2014.

[74] Fisch, R., Franke, J., Wüchner, R., and Bletzinger, K. Code verification examples of a fully geometrical nonlinear membrane element using the method of manufactured solutions. In *Proceedings Structural Membranes 2013* (Munich, Germany, October 9-11, 2013), K.-U.Bletzinger, B. Kröplin, and E. Oñate, Eds.

[75] Fisch, R., Franke, J., Wüchner, R., and Bletzinger, K. Code verification of a partitioned FSI environment for wind engineering applications using the method of manufactured solutions. In *5th European Conference on Computational Mechanics (ECCM V)* (Barcelona, Spain, July 20-15, 2014), E. Oñate, J. Oliver, and A. Huerta, Eds.

[76] François, S., Coulier, P., and Degrande, G. Finite element–boundary element coupling algorithms for transient elastodynamics. *Engineering Analysis with Boundary Elements 55* (2015), 104–121.

[77] Fries, T., Omerović, S., Schöllhammer, D., and Steidl, J. Higher-order meshing of implicit geometries part I: Integration and interpolation in cut elements. *Computer Methods in Applied Mechanics and Engineering 313* (2017), 759–784.

[78] Fries, T., and Schöllhammer, D. Higher-order meshing of implicit geometries part II: Approximations on manifolds. *submitted to Computer Methods in Applied Mechanics and Engineering* (2017).

[79] Fritze, D., Marburg, S., and Hardtke, H.-J. FEM–BEM-coupling and structural–acoustic sensitivity analysis for shell geometries. *Computers & Structures 83*, 2 (2005), 143–154.

[80] Gander, M. J., and Wanner, G. From Euler, Ritz, and Galerkin to modern computing. *SIAM Review 54*, 4 (2012), 627–666.

[81] Godinho, L., Amado-Mendes, P., Pereira, A., and Soares, D. A coupled MFS–FEM model for 2-D dynamic soil–structure interaction in the frequency domain. *Computers & Structures 129* (2013), 74–85.

[82] Godinho, L., Costa, E., Pereira, A., and Santiago, J. Some observations on the behavior of the method of fundamental solutions in 3D acoustic problems. *International Journal of Computational Methods 9*, 4 (2012), 1250049 1–25.

[83] Graff, K. F. *Wave motion in elastic solids*. Courier Corporation, 2012.

[84] Gurtin, M. E. *An introduction to continuum mechanics*. Academic Press, 1982.

[85] Hiptmair, R., Moiola, A., and Perugia, I. A survey of trefftz methods for the helmholtz equation. In *Building Bridges: Connections and Challenges in Modern Approaches to Numerical Partial Differential Equations*. Springer, 2016, pp. 237–278.

[86] Holzapfel, G. A. *Nonlinear solid mechanics*, vol. 24. Wiley Chichester, 2000.

[87] Hörlin, N.-E., Nordström, M., and Göransson, P. A 3-D hierarchical FE formulation of Biot's equations for elasto-acoustic modelling of porous media. *Journal of Sound and Vibration 245*, 4 (2001), 633–652.

[88] Hosseini, S., Remmers, J. J., Verhoosel, C. V., and Borst, R. An isogeometric solid-like shell element for nonlinear analysis. *International Journal for Numerical Methods in Engineering 95*, 3 (2013), 238–256.

[89] Hosseini, S., Remmers, J. J., Verhoosel, C. V., and De Borst, R. An isogeometric continuum shell element for non-linear analysis. *Computer Methods in Applied Mechanics and Engineering 271* (2014), 1–22.

[90] Hughes, T. J., Cottrell, J. A., and Bazilevs, Y. Isogeometric analysis: CAD, finite elements, NURBS, exact geometry and mesh refinement. *Computer Methods in Applied Mechanics and Engineering 194*, 39 (2005), 4135–4195.

[91] Jamet, P. Estimation of the interpolation error for quadrilateral finite elements which can degenerate into triangles. *SIAM Journal on Numerical Analysis 14*, 5 (1977), 925–930.

[92] Johnson, D. L., Koplik, J., and Dashen, R. Theory of dynamic permeability and tortuosity in fluid-saturated porous media. *Journal of Fluid Mechanics 176* (1987), 379–402.

[93] Jonckheere, S., Deckers, E., Van Genechten, B., Vandepitte, D., and Desmet, W. A direct hybrid Finite Element–Wave Based Method for the steady-state analysis of acoustic cavities with poro-elastic damping layers using the coupled Helmholtz–Biot equations. *Computer Methods in Applied Mechanics and Engineering 263* (2013), 144–157.

[94] Jung, M., and Langer, U. *Methode der finiten Elemente für Ingenieure: Eine Einführung in die numerischen Grundlagen und Computersimulation*. Springer-Verlag, 2012.

[95] Kästner, M., Metsch, P., and De Borst, R. Isogeometric analysis of the Cahn–Hilliard equation – a convergence study. *Journal of Computational Physics 305* (2016), 360–371.

[96] Kiendl, J., Bletzinger, K.-U., Linhard, J., and Wüchner, R. Isogeometric shell analysis with Kirchhoff–Love elements. *Computer Methods in Applied Mechanics and Engineering 198*, 49 (2009), 3902–3914.

[97] Kienzler, R. On consistent plate theories. *Archive of Applied Mechanics 72*, 4-5 (2002), 229–247.

[98] Kienzler, R., and Schneider, P. Consistent theories of isotropic and anisotropic plates. *Journal of Theoretical and Applied Mechanics 50* (2012), 755–768.

[99] Királyfalvi, G., and Szabó, B. A. Quasi-regional mapping for the p-version of the finite element method. *Finite Elements in Analysis and Design 27*, 1 (1997), 85–97.

[100] Kirchhoff, G. Über das Gleichgewicht und die Bewegung einer elastischen Scheibe. *Journal für die reine und angewandte Mathematik 40* (1850), 51–88.

[101] Kita, E., and Kamiya, N. Trefftz method: An overview. *Advances in Engineering Software 24*, 1 (1995), 3–12.

[102] Koiter, W. A consistent first approximation in the general theory of thin elastic shells. *Theory of Thin Elastic Shells* (1960), 12–33.

[103] Koiter, W. On the mathematical foundation of shell theory. In *Proc. Int. Congr. of Mathematics, Nice* (1970), vol. 3, pp. 123–130.

[104] Koschnick, F. *Geometrische Lockingeffekte bei Finiten Elementen und ein allgemeines Konzept zu ihrer Vermeidung*. PhD thesis, Institut für Baustatik, Technische Universität München, Germany, 2004.

[105] Lee, J. S., Deckers, E., Jonckheere, S., Desmet, W., and Kim, Y. Y. A direct hybrid finite element–wave based modelling technique for efficient analysis of poroelastic materials in steady-state acoustic problems. *Computer Methods in Applied Mechanics and Engineering 304* (2016), 55–80.

[106] Lehrenfeld, C. High order unfitted finite element methods on level set domains using isoparametric mappings. *Computer Methods in Applied Mechanics and Engineering 300* (2016), 716–733.

[107] Li, K., Zhang, W., and Huang, A. An asymptotic analysis method for the linearly shell theory. *Science in China Series A: Mathematics 49*, 8 (2006), 1009–1047.

[108] Lim, S. P., and Haron, H. Surface reconstruction techniques: a review. *Artificial Intelligence Review 42*, 1 (2014), 59–78.

[109] Lods, V., and Mardare, C. Asymptotic justification of the Kirchhoff–Love assumptions for a linearly elastic clamped shell. *Journal of Elasticity and the Physical Science of Solids 58*, 2 (2000), 105–154.

[110] Lods, V., and Mardare, C. A justification of linear Koiter and Naghdi's models for totally clamped shell. *Asymptotic Analysis 31*, 3, 4 (2002), 189–210.

[111] Long, Q., Burkhard Bornemann, P., and Cirak, F. Shear-flexible subdivision shells. *International Journal for Numerical Methods in Engineering 90*, 13 (2012), 1549–1577.

[112] Lorensen, W. E., and Cline, H. E. Marching cubes: A high resolution 3d surface construction algorithm. In *ACM Siggraph Computer Graphics* (1987), vol. 21, ACM, pp. 163–169.

[113] Love, A. E. H. The small free vibrations and deformation of a thin elastic shell. *Philosophical Transactions of the Royal Society of London. A 179* (1888), 491–546.

[114] Macneal, R. H., and Harder, R. L. A proposed standard set of problems to test finite element accuracy. *Finite Elements in Analysis and Design 1*, 1 (1985), 3–20.

[115] Majeed, M., and Cirak, F. Isogeometric analysis using manifold-based smooth basis functions. *Computer Methods in Applied Mechanics and Engineering 316* (2017), 547–567.

[116] Malaya, N., Estacio-Hiroms, K. C., Stogner, R. H., Schulz, K. W., Bauman, P. T., and Carey, G. F. Masa: a library for verification using manufactured and analytical solutions. *Engineering with Computers 29*, 4 (2013), 487–496.

[117] Marciniak-Czochra, A., and Mikelić, A. A rigorous derivation of the equations for the clamped Biot-Kirchhoff-Love poroelastic plate. *Archive for Rational Mechanics and Analysis 215*, 3 (2015), 1035–1062.

[118] Marco, O., Sevilla, R., Zhang, Y., Ródenas, J. J., and Tur, M. Exact 3D boundary representation in finite element analysis based on Cartesian grids independent of the geometry. *International Journal for Numerical Methods in Engineering* (2015).

[119] Marsden, J. E., and Hughes, T. J. *Mathematical foundations of elasticity*. Dover Publications, New York, 1983.

[120] Mikelic, A., and Tambaca, J. Derivation of a poroelastic flexural shell model. *Multiscale Modeling & Simulation 14*, 1 (2016), 364–397.

[121] Mindlin, R. Influence of rotatory inertia and shear on flexural motion of isotropic elastic plates. *Journal of Applied Mechanics 18* (1951), 31–38.

[122] Morgenstern, D. Herleitung der Plattentheorie aus der dreidimensionalen Elastizitätstheorie. *Archive for Rational Mechanics and Analysis 4*, 1 (1959), 145–152.

[123] Naghdi, P. The theory of plates and shells. *Handbuch der Physik IV* (1972), 425–640.

[124] Naghdi, P. M. Foundations of elastic shell theory. *Progress in Solid Mechanics 4* (1963), 1–90.

[125] Nagler, L., Rong, P., Schanz, M., and von Estorff, O. Sound transmission through a poroelastic layered panel. *Computational Mechanics 53*, 4 (2014), 549–560.

[126] Nagler, L., and Schanz, M. An extendable poroelastic plate formulation in dynamics. *Archive of Applied Mechanics 80* (2010), 1177–1195.

[127] Nennig, B., Perrey-Debain, E., and Chazot, J.-D. The method of fundamental solutions for acoustic wave scattering by a single and a periodic array of poroelastic scatterers. *Engineering Analysis with Boundary Elements 35*, 8 (2011), 1019–1028.

[128] Oberkampf, W. L., and Roy, C. J. *Verification and validation in scientific computing*. Cambridge University Press, 2010.

[129] Oberkampf, W. L., Trucano, T. G., and Hirsch, C. Verification, validation, and predictive capability in computational engineering and physics. *Applied Mechanics Reviews 57*, 5 (2004), 345–384.

[130] Oden, J. T., Belytschko, T., Fish, J., Hughes, T., Johnson, C., Keyes, D., Laub, A., Petzold, L., Srolovitz, D., and Yip, S. Revolutionizing engineering science through simulation. *National Science Foundation Blue Ribbon Panel Report 65* (2006).

[131] Oesterle, B., Ramm, E., and Bischoff, M. A shear deformable, rotation-free isogeometric shell formulation. *Computer Methods in Applied Mechanics and Engineering 307* (2016), 235–255.

[132] Oñate, E. *Structural analysis with the finite element method. Linear statics: Volume 2: Beams, plates and shells*. Springer Science & Business Media, 2013.

[133] Ozyazicioglu, M. Sudden pressurization of a spherical cavity in a poroelastic medium. *Mathematical Problems in Engineering 2013* (2013).

[134] Parvizian, J., Düster, A., and Rank, E. Finite cell method. *Computational Mechanics 41*, 1 (2007), 121–133.

[135] Paumier, J.-C., and Raoult, A. Asymptotic consistency of the polynomial approximation in the linearized plate theory. In *ESAIM: Proceedings* (1997), vol. 2, EDP Sciences, pp. 203–213.

[136] Payette, G., and Reddy, J. A seven-parameter spectral/hp finite element formulation for isotropic, laminated composite and functionally graded shell structures. *Computer Methods in Applied Mechanics and Engineering 278* (2014), 664–704.

[137] Peano, A. Hierarchies of conforming finite elements for plane elasticity and plate bending. *Computers & Mathematics with Applications 2*, 3-4 (1976), 211–224.

[138] Peano, A. Conforming approximations for Kirchhoff plates and shells. *International Journal for Numerical Methods in Engineering 14*, 9 (1979), 1273–1291.

[139] Pechstein, A., and Schöberl, J. Anisotropic mixed finite elements for elasticity. *International Journal for Numerical Methods in Engineering 90*, 2 (2012), 196–217.

[140] Rank, E., Düster, A., Nübel, V., Preusch, K., and Bruhns, O. High order finite elements for shells. *Computer Methods in Applied Mechanics and Engineering 194*, 21 (2005), 2494–2512.

[141] Rank, E., Kollmannsberger, S., Sorger, C., and Düster, A. Shell finite cell method: A high order fictitious domain approach for thin-walled structures. *Computer Methods in Applied Mechanics and Engineering 200*, 45 (2011), 3200–3209.

[142] Reddy, J. N. *Mechanics of laminated composite plates and shells: Theory and analysis*. CRC press, 2004.

[143] Reissner, E. On the theory of bending of elastic plates. *Journal of Mathematics and Physics 23*, 1 (1944), 184–191.

[144] Reissner, E. The effect of transverse shear deformation on the bending of elastic plates. *Journal of Applied Mechanics 12* (1945), 69?76.

[145] Reynolds, D. D. *Engineering principles of acoustics: Noise and vibration control*. Allyn & Bacon, 1981.

[146] Ritz, W. Über eine neue Methode zur Lösung gewisser Variationsprobleme der mathematischen Physik. *Journal für die reine und angewandte Mathematik 135* (1909), 1–61.

[147] Roache, P. J. *Verification and validation in computational science and engineering*. Hermosa, 1998.

[148] Rosenberg, S. *The Laplacian on a Riemannian manifold: An introduction to analysis on manifolds*. No. 31 in London Mathematical Society. Cambridge University Press, 1997.

[149] Rössle, A., Bischoff, M., Wendland, W., and Ramm, E. On the mathematical foundation of the (1, 1, 2)-plate model. *International Journal of Solids and Structures 36*, 14 (1999), 2143–2168.

[150] Roy, C. J. Review of code and solution verification procedures for computational simulation. *Journal of Computational Physics 205*, 1 (2005), 131–156.

[151] Roy, C. J., Nelson, C., Smith, T., and Ober, C. Verification of Euler/Navier–Stokes codes using the method of manufactured solutions. *International Journal for Numerical Methods in Fluids 44*, 6 (2004), 599–620.

[152] Rüberg, T. *Non-conforming FEM/BEM coupling in time domain*. Monographic Series TU Graz, Computation in Engineering and Science, 2008.

[153] Rüberg, T., Cirak, F., and Aznar, J. M. G. An unstructured immersed finite element method for nonlinear solid mechanics. *Advanced Modeling and Simulation in Engineering Sciences 3*, 1 (2016), 22.

[154] Sander, O., Neff, P., and Bîrsan, M. Numerical treatment of a geometrically nonlinear planar Cosserat shell model. *Computational Mechanics 57*, 5 (2016), 817–841.

[155] Schanz, M., and Diebels, S. A comparative study of Biot's theory and the linear theory of porous media for wave propagation problems. *Acta Mechanica 161*, 3-4 (2003), 213–235.

[156] Schillinger, D., and Ruess, M. The Finite Cell Method: A review in the context of higher-order structural analysis of CAD and image-based geometric models. *Archives of Computational Methods in Engineering 22*, 3 (2015), 391–455.

[157] Schlesinger, S., Crosbie, R. E., Gagné, R. E., Innis, G. S., Lalwani, C. S., Loch, J., Sylvester, R. J., Wright, R. D., Kheir, N., and Bartos, D. Terminology for model credibility. *Simulation 32*, 3 (1979), 103–104.

[158] Schneider, P., Kienzler, R., and Böhm, M. Modeling of consistent second-order plate theories for anisotropic materials. *ZAMM - Journal of Applied Mathematics and Mechanics 94*, 1-2 (2014), 21–42.

[159] Shih, T. A procedure to debug computer programs. *International Journal for Numerical Methods in Engineering 21*, 6 (1985), 1027–1037.

[160] Sladek, J., Sladek, V., Gfrerer, M., and Schanz, M. Mindlin theory for the bending of porous plates. *Acta Mechanica 226*, 6 (2015), 1909–1928.

[161] Sommerfeld, A. Die Greensche Funktion der Schwingungsgleichung. *Jahresbericht der Deutschen Mathematiker-Vereinigung 21* (1912), 309–352.

[162] Steinbach, O. *Numerical approximation methods for elliptic boundary value problems*. Springer, 2008.

[163] Strang, G., and Fix, G. J. *An analysis of the finite element method*, vol. 212. Prentice-Hall Englewood Cliffs, N.J., 1973.

[164] Szabó, B., and Babuška, I. *Introduction to finite element analysis: Formulation, verification and validation*, vol. 35. John Wiley & Sons, 2011.

[165] Taber, L. A. A theory for transverse deflection of poroelastic plates. *Journal of Applied Mechanics 59*, 3 (1992), 628–634.

[166] Takacs, T., and Jüttler, B. Existence of stiffness matrix integrals for singularly parameterized domains in isogeometric analysis. *Computer Methods in Applied Mechanics and Engineering 200*, 49 (2011), 3568–3582.

[167] Tews, R., and Rachowicz, W. Application of an automatic hp adaptive finite element method for thin-walled structures. *Computer Methods in Applied Mechanics and Engineering 198*, 21 (2009), 1967–1984.

[168] Theodorakopoulos, D., and Beskos, D. Flexural vibrations of fissured poroelastic plates. *Archive of Applied Mechanics 63*, 6 (1993), 413–423.

[169] Theodorakopoulos, D., and Beskos, D. Flexural vibrations of poroelastic plates. *Acta Mechanica 103*, 1-4 (1994), 191–203.

[170] Trefftz, E. Ein Gegenstuck zum ritzschen Verfahren. *Proc. 2nd Int. Cong. Appl. Mech., Zurich, 1926* (1926), 131–137.

[171] Van Genechten, B., Vandepitte, D., and Desmet, W. A direct hybrid finite element–wave based modelling technique for efficient coupled vibro-acoustic analysis. *Computer Methods in Applied Mechanics and Engineering 200*, 5 (2011), 742–764.

[172] Veeraragavan, A., Beri, J., and Gollan, R. Use of the method of manufactured solutions for the verification of conjugate heat transfer solvers. *Journal of Computational Physics 307* (2016), 308–320.

[173] Vekua, I. *Shell Theory: General Methods of Construction*. Monographs and Studies in Mathematics. Addison-Wesley Longman, 1985.

[174] Vogelius, M., and Babuška, I. On a dimensional reduction method. I. The optimal selection of basis functions. *Mathematics of Computation 37*, 155 (1981), 31–46.

[175] Vogelius, M., and Babuška, I. On a dimensional reduction method. II. Some approximation-theoretic results. *Mathematics of Computation 37*, 155 (1981), 47–68.

[176] Vogelius, M., and Babuška, I. On a dimensional reduction method. III. A posteriori error estimation and an adaptive approach. *Mathematics of Computation 37*, 156 (1981), 361–384.

[177] von Terzaghi, K. Die Berechnung der Durchlässigkeit des Tones aus dem Verlauf der hydromechanischen Spannungserscheinungen. *Sitzungsbericht der Akademie der Wissenschaften (Wien): Mathematisch-Naturwissenschaftlichen Klasse 132* (1923), 125–138.

[178] Wassermann, B., Kollmannsberger, S., Bog, T., and Rank, E. From geometric design to numerical analysis: A direct approach using the Finite Cell Method on Constructive Solid Geometry. *Computers & Mathematics with Applications* (2017).

[179] Weingarten, J. Ueber eine Klasse auf einander abwickelbarer Flächen. *Journal für die reine und angewandte Mathematik 59* (1861), 382–393.

[180] Wen, P., and Liu, Y. The fundamental solution of poroelastic plate saturated by fluid and its applications. *International Journal for Numerical and Analytical Methods in Geomechanics 34*, 7 (2010), 689–709.

[181] Wolfram Research, Inc. *Mathematica, Version 11.1*. Champaign, Illinios, 2017.

[182] Zaglmayr, S. *High order finite element methods for electromagnetic field computation*. PhD thesis, Institut für Numerische Mathematik, JKU Linz, Austria, 2006.

[183] Zhavoronok, S. A Vekua-type linear theory of thick elastic shells. *ZAMM-Journal of Applied Mathematics and Mechanics 94*, 1-2 (2014), 164–184.

[184] Zienkiewicz, O. C., and Taylor, R. L. *The finite element method for solid and structural mechanics*. Butterworth-Heinemann, 2005.

[185] Zienkiewicz, O. C., Taylor, R. L., and Zhu, J. Z. *The Finite Element Method: Its Basis and Fundamentals*. Butterworth-Heinemann, 2005.